

Surface-state Coulomb Repulsion Accelerates a Metal-insulator Transition in Topological Semimetal Nanofilms

S. Ito^a, M. Arita^b, J. Haruyama^a, B. Feng^c, W.-C. Chen^d, H. Namatame^b,
M. Taniguchi^b, C.-M. Cheng^e, G. Bian^f, S.-J. Tang^{d,e}, T.-C. Chiang^g, O. Sugino^a,
F. Komori^a, I. Matsuda^a

^a*Institute for Solid State Physics, The University of Tokyo, Kashiwa, Chiba 277-8581, Japan*

^b*Hiroshima Synchrotron Radiation Center, Hiroshima University, Higashi-Hiroshima, Hiroshima 739-0046, Japan*

^c*Institute of Physics, Chinese Academy of Sciences, Beijing 100190, China*

^d*Department of Physics and Astronomy, National Tsing Hua University, Hsinchu, Taiwan 30013, Republic of China*

^e*National Synchrotron Radiation Research Center (NSRRC), Hsinchu, Taiwan 30076, Republic of China*

^f*Department of Physics and Astronomy, University of Missouri, Columbia, MO 65211, USA*

^g*Department of Physics and Frederick Seitz Materials Research Laboratory, University of Illinois at Urbana-Champaign, Urbana, IL 61801, USA*

Keywords: quantum-size effect, metal-insulator transition, Coulomb repulsion

When confined to the microscopic scale, materials exhibit quantized electronic states. One of the most conspicuous example of the quantum-size effect (QSE) is a transition into an insulating state in a semimetallic nanofilm, which was predicted more than half a century ago on bismuth (Bi) [1]. The transition historically attracted great attention as a nanoscale pathway for achieving a substantial thermoelectric figure of merit and is now of interest for enhancing the surface-state-induced exotic phenomena stemming from the nontrivial electronic topology [2]. Although the transition was evidenced by transport experiments [3,4], a recent angle-resolved photoelectron spectroscopy (ARPES) measurement reported a metallic signature on atomically thin Bi films fabricated in the same way as in the transport experiments [5]. This strange contradiction indicates an interesting mechanism behind. However, essential information of quantization was lacked in all previous studies.

In the present research, we revealed an unexpected mechanism of the transition in Bi films by combining high-resolution ARPES measurements on high-quality films and the density-functional theory (DFT) calculations [6]. The experiments were performed in HiSOR BL-9A and NSRRC BL-21B1. Photon energies of 21 eV and 8.4 eV were used. The measurement temperature was set to 10 K and the total energy resolution was estimated as 7 meV. A Ge(111) wafer was used as a substrate and cleaned by cycles of Ar⁺ sputtering (1 kV) and annealing (600 °C). Bi was deposited on it at room temperature with a pressure kept at a very low level (1×10^{-8} Pa). The thickness was precisely calibrated using a quartz thickness monitor. Fig. 1 (a) shows peak-enhanced ARPES images measured on 9, 14, 18 bilayer (BL) Bi films (1 BL = 3.9 Å), where all quantized bulk bands and surface bands are clearly resolved. One can see that the top quantized levels are shifting below the Fermi level with decreasing thickness. This is the first direct observation of the QSE-induced transition into an insulating phase in Bi films. Markers in Fig. 1(c) show thickness dependence of each quantized level. The evolution turned out to largely divert from simple parabolic behaviors expected from a conventional model of QSE.

The high-resolution ARPES observation revealed another unusual signature: both of two surface bands connect to the top quantized bulk band. Because surface bands are doubly degenerate, this band connection means that the top quantized state must be quadruply degenerate as illustrated in Fig. 1(b). This unexpected behavior was reproduced by our DFT calculations, which showed transformation of the quantized bulk states into surface-localized states. The underlying mechanism can be understood based on the general framework of DFT: an effective one-body potential and a total charge density are determined by a self-consistent cycle reflecting Coulomb interaction. A decrease in the system size increases relative contributions of thickness-

independent surface states to the total charge density. This tendency makes Coulomb repulsion among electrons compress the total charge density toward the film center. In the one-body picture of the DFT framework, this compressed total charge induces a potential barrier around the film center, which creates a double-well potential, as illustrated in Fig. 1(d). Such a double-well potential supports degenerate ground states whose wave functions are localized in both wells with opposite parity. Furthermore, experimental thickness dependence of quantized levels was excellently reproduced by a numerical simulation using a single-well potential which gradually deforms into a double well (solid curves in Fig. 1(c)).

This novel picture of the transition naturally reconciles the contradiction observed in previous studies. Even when the top quantized levels cross the Fermi level, the top quantized states only contribute to surface-conducting channels, and the film interior is still insulating as observed in transport experiments. Thus, we established the complete picture of the half-century problem in Bi, which demonstrates a new class of size effects driven by increased Coulomb repulsion from surface states.

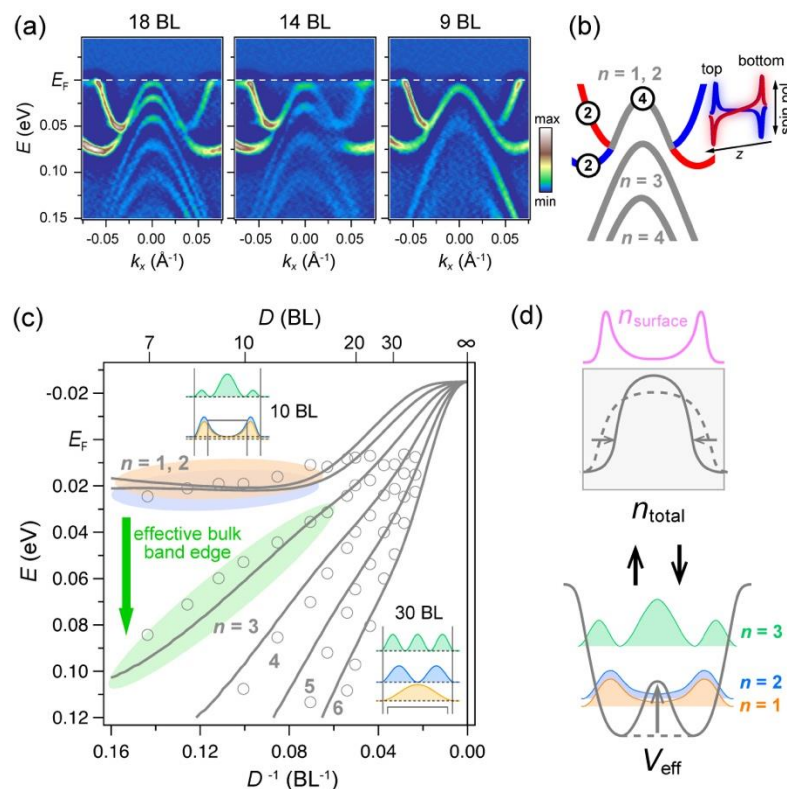


FIGURE 1. (a) Second-derivative ARPES images measured on atomically thin Bi films. (b) Schematics of unexpected band connection and level degeneracy. (c) Comparison of thickness dependence of quantized levels from ARPES measurements (markers) and a numerical simulation (solid lines). The inset depicts wave function characters obtained in the simulation. (d) Schematic of a self-consistent cycle for a total charge density and an effective confinement potential.

REFERENCES

1. V. B. Sandomirskii, Soviet Physics JETP **25**, 101-106 (1967)
2. S. Ito, B. Feng, M. Arita, A. Takayama, T. Someya, W.-C. Chen, C.-M. Cheng, C.-H. Lin, S. Yamamoto, T. Imori, H. Namatame, M. Taniguchi, S.-J. Tang, F. Komori, K. Kobayashi, and I. Matsuda, Phys. Rev. Lett. **117**, 236402 (2016).
2. S. Xiao, D. Wei, X. Jin, Phys. Rev. Lett. **109**, 166805 (2012).
3. P. Kröger, D. Abdelbarey, M. Siemens, D. Lükermann, S. Sologub, H. Pfnür, C. Tegenkamp, Phys. Rev. B **97**, 045403 (2018).
4. T. Hirahara, T. Shirai, T. Hajiri, M. Matsunami, K. Tanaka, S. Kimura, S. Hasegawa, K. Kobayashi, Phys. Rev. Lett. **115**, 106803 (2015).
5. S. Ito, M. Arita, J. Haruyama, B. Feng, W.-C. Chen, H. Namatame, M. Taniguchi, C.-M. Cheng, G. Bian, S.-J. Tang, T.-C. Chiang, O. Sugino, F. Komori, I. Matsuda, Science Advances **6**, eaaz5015 (2020).

ARPES studies of the layered ternary superconductors with low-carrier-density

Y. Akimoto^a, Kenta Kuroda^a, K. Kawaguchi^a, Y. Arai^a, M. Arita^b, D. Hirai^a,
Z. Hiroi^a, T. Yamada^b, Takeshi Kondo^a

^aISSP, University of Tokyo, Kashiwa, Chiba 277-8581, Japan

^bHiroshima Synchrotron Radiation Center, Hiroshima University, Higashi-Hiroshima, 739-0046, Japan

^cInstitute of Multidisciplinary Research for Advanced Material, Tohoku University, 2-1-1, Katahira, Aoba-ku, Sendai 980-8577, Japan

Keywords: Superconductors, Electronic structures

The discovery of new superconductors can give deeper or different insights to underlying properties that preferably induces superconducting pairing. The high- T_c superconductivity in Fe pnictides is a great example for it, providing a great platform to examine close relationships between magnetism and superconductivity. Among them, one of anti-PbFCl-type AFePn (A=alkali metals, Pn = P or As) compounds, LiFeAs with $T_c=18$ K has been extensively investigated [1].

Recently, a new member of ternary silicide NaAlSi with $T_c=7$ K has been successfully synthesized by high-pressure technique [2], which has the same crystal structure as the 111 Fe-based superconductors (space group $P4/nmm$, $Z=2$). This discovery is interesting; this material is a simple s - p electron system with very low-carrier density but shows such high T_c even at ambient pressure. Moreover, there is a family compound, NaAlGe, in which no superconductivity is observed at least above 1.8 K [2]. Since the electronic band structures of NaAlSi and NaAlGe should be very similar, the Si-related higher frequency phonon modes and/or the contribution of Si- $3p$ electronic states with smaller spin-orbit coupling should play a key role in establishing the BCS-type superconductivity in ternary silicide NaAlSi. Local-density approximation calculations have been made to investigate the electronic properties [3]. However, no experimental investigation has been carried out so far to reveal the electronic properties for NaAlSi and NaAlGe and their difference.

In this study, we have performed synchrotron-radiation based angle-resolved photoemission spectroscopy with low energy photons ranging in 6-32 eV at BL-9A of HiSOR, and systematically investigated the band structures in the both NaAlSi and NaAlGe. We show two important results. One is that the electronic structures of these two materials exhibit common features; two-dimensional character with weakly dispersion along k_z direction and flat-hole bands at Fermi energy (E_F) deriving from Si $2p$ (Ge $3p$) orbitals. Second is that there are slight differences, particularly the energy position of the flat bands probably due to distinct strength of their spin-orbit coupling.

We firstly observe weak but clear k_z dispersions of NaAlSi and NaAlGe by scanning the photon energy ($h\nu$), and determine a proper $h\nu$ to cut high-symmetry line in the bulk Brillouin zone. Figure 1 represents their band dispersion along Γ -X line. The main feature of the observed dispersions are the two-hole bands. One of them exhibits a sharp dispersion with the strong cross section. In sharp contrast, the other hole band with weak intensity features in flat in vicinity of E_F . By our band calculations, these two bands derive from Si $2p$ (Ge $3p$) orbitals and corresponds to the heavy and light hole dispersion with $J=2/3$ states. These features are commonly observed in

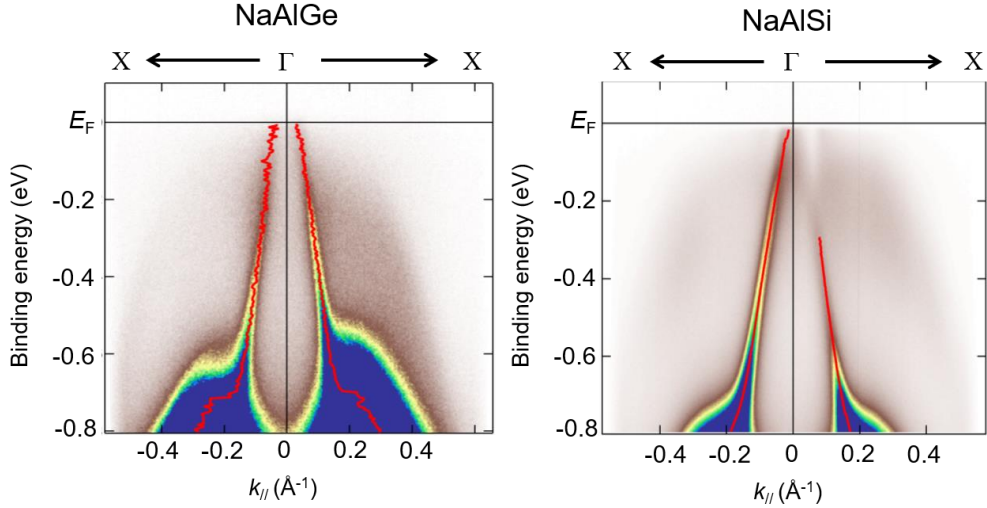


FIGURE 1. ARPES band maps for NaAlGe and NaAlSi cut along X- Γ -X high symmetry line.

the two materials.

We interestingly find that the energy positions of the hole bands are slightly different. This can be more clearly recognized by fitting analysis (see red lines in Fig.1). It is apparent that the top of the hole bands are located above E_F in NaAlGe but it slightly shifts down in energy in NaAlSi and is eventually located almost at E_F . This change is elucidated by weaker spin-orbit coupling in the Si-compound. As the top of the heavy and light hole-bands are degenerate at Γ point, the heavy hole-band should be almost at E_F in NaAlSi that is a superconductor with $T_c=7$ K. Therefore, we think that such flat band generally with high density of states are related to the mechanism of the superconductivity of NaAlSi.

REFERENCES

1. J. H. Tapp *et al.*, Phys. Rev. B **78**, 060505 (R) (2008).
2. S. Kuroiwa *et al.*, Physica C **466**, 11 (2007).
3. H. B. Rhee *et al.*, Phys. Rev. B **81**, 060505 (R) (2008).

Angle-resolved photoemission spectroscopy of valence transition compound YbInCu₄

K. Maeda^a, T. Matsumoto^a, Y. Tanaka^b, H. Sato^c, M. Arita^c,
K. Shimada^c, K. Matsumoto^d, K. Hiraoka^d

^aGraduate School of Science, Hiroshima University, Higashi-Hiroshima 739-8526, Japan

^bFaculty of Science, Hiroshima University, Higashi-Hiroshima 739-8526, Japan

^cHiroshima Synchrotron Radiation Center, Hiroshima University, Higashi-Hiroshima 739-0046, Japan

^dGraduate School of Science and Engineering, Ehime University, Matsuyama 790-8577, Japan

Keywords: angle resolved photoemission spectroscopy, valence transition, *c-f* hybridization

Yb compounds have interesting physical properties originated from 4*f* electrons. The Yb takes divalent state (Yb²⁺:4*f*¹⁴) and trivalent state (Yb³⁺:4*f*¹³). The Yb valence in the compounds fluctuates between the two states and has non-integer value averaged over the compounds. Among the Yb compounds, YbInCu₄ shows the first order valence transition at $T_v = 42$ K. The mean Yb valences have been estimated to be ~ 2.90 in the high temperature phase and ~ 2.74 in the low temperature phase from the Yb 3*d* hard x-ray photoemission spectra [1]. The magnetic susceptibility changes discontinuity from the Curie-Weiss behavior (high temperature phase) to Pauli paramagnetic behavior (low temperature phase) across T_v . The Kondo temperature also changes from $T_K \sim 25$ K to ~ 400 K below T_v , which indicates that a degree of hybridization between the conduction and Yb 4*f* electrons (*c* - *f* hybridization) increases in the low temperature phase. A number of studies of electronic structure of YbInCu₄ by means of angle-integrated photoemission spectroscopy have been reported [1, 2]. Previously we successfully observed the increase of the *c* - *f* hybridization strength below T_v by means of the angle-integrated low-energy excited photoemission spectroscopy at $h\nu = 7$ eV [3]. On the other hand, angle-resolved photoemission spectroscopy (ARPES) study of YbInCu₄ has been limited because the flat surface to obtain the clear ARPES spectra is difficult to be prepared by the usual fracturing method. Only one ARPES result for YbInCu₄ is reported although the measured band dispersions are unclear [4]. To clarify the change in their band structures near the Fermi level (E_F) associated with the valence transition by means of ARPES, is indispensable to reveal the mechanism of the valence transition.

In this study, we prepared YbInCu₄(111) surface for ARPES measurements as follows. First, the sample was polished in air until a mirror-like surface plane was obtained, and then the polished YbInCu₄(111) surface was cleaned by Ar⁺ ion sputtering in 3 hours and annealing at about 400 °C in 8 hours. The cleanliness and flatness of the obtained surface is characterized by means of the Auger electron spectroscopy and low-energy electron diffraction. Single crystals of YbInCu₄ were synthesized by flux-method. The ARPES experiments on YbInCu₄(111) were performed at undulator beamline BL-9A of Hiroshima Synchrotron Radiation Center (HSRC). The ARPES spectra were collected at $h\nu = 23.2$ eV along the Γ -M and Γ -K directions of the surface Brillouin zone.

Figures 1(a) and 1(b) show ARPES intensity plots for YbInCu₄(111) along with the Γ -M and Γ -K directions, respectively, taken with the *p*-polarized configuration at 6 K. A vertical axis represents binding energy (E_B) relative to E_F and a horizontal axis wave number (*k*) along the respective direction. We successfully observed the clear band dispersions as shown in Fig. 1. For the Γ -M direction (Fig. 1 (a)), we notice almost no dispersive band A around $E_B = 0.03$ eV, which is attributed to the Yb²⁺ 4*f*_{7/2} band. The dispersive M-shaped band B is due to the conduction electron band. We also notice electron pocket like band C around the Γ point. These characteristic three bands are also observed for the Γ -K direction (Fig. 1 (b)), although the feature of the B band is different between the two directions. This indicates that the B band at $|k| > 0.2 \text{ \AA}^{-1}$ largely dispersive along the M-K direction. The different feature of the B band is well reproduced by the band-structure calculation using the WIEN2k code [4]. However, the C band is not reproduced by the calculation.

Figure 2 shows the temperature dependence of the ARPES intensity plots for YbInCu₄(111) along with

the Γ -K direction. All the A-C bands shift to the deeper binding-energy with decreasing temperature. It is noted that the splitting between the A and B bands around $k = 0.2 \text{ \AA}^{-1}$ increases with decreasing temperature. The splitting is explained as a result of the c - f hybridization between the $\text{Yb}^{2+} 4f_{7/2}$ band (A) and conduction electron band (B). The C band, which is not reproduced by the band-structure calculation, is also interpreted as an anti-bonding band. The splitting energy between the A and B bands corresponds to the c - f hybridization gap. Thus, we succeeded in the direct observation the increase of the c - f hybridization below T_v , for the first time.

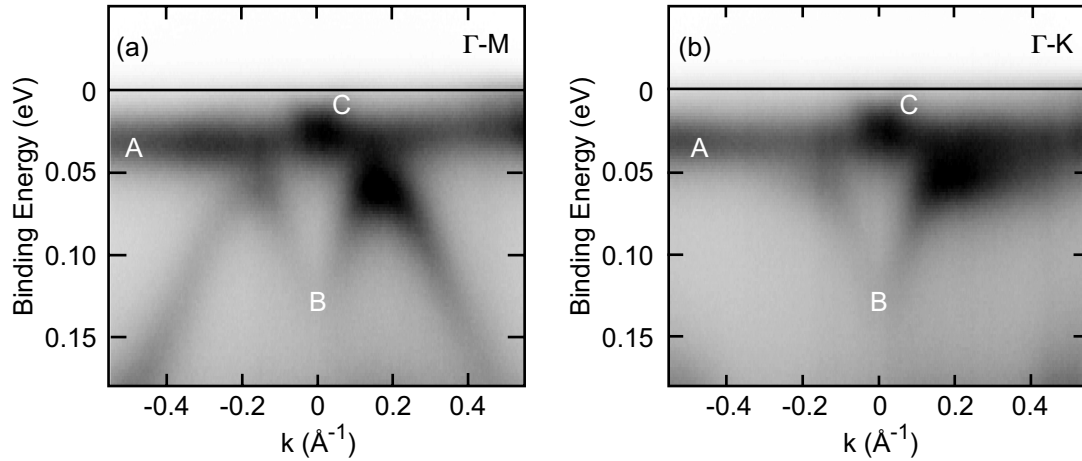


FIGURE 1. ARPES intensity plots of $\text{YbInCu}_4(111)$ along with (a) Γ -M and (b) Γ -K directions measured at 6 K.

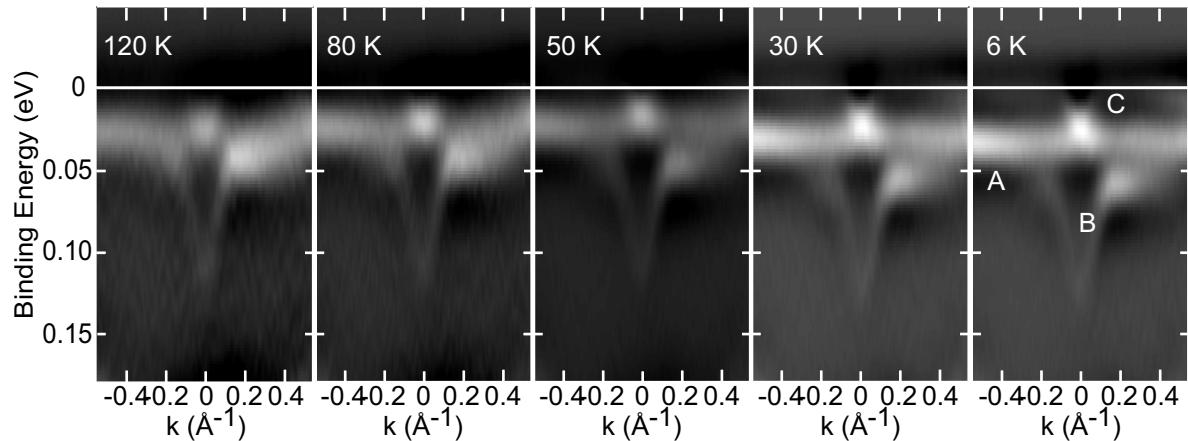


FIGURE 2. ARPES intensity plots of $\text{YbInCu}_4(111)$ along with Γ -K directions measured between 120 and 6 K.

REFERENCES

1. H. Sato, K. Shimada, M. Arita, K. Hiraoka, K. Kojima, Y. Takeda, K. Yoshikawa, M. Sawada, M. Nakatake, H. Namatame, M. Taniguchi, Y. Takata, E. Ikenaga, S. Shin, K. Kobayashi, K. Tamasaku, Y. Nishino, D. Miwa, M. Yabashi and T. Ishikawa, *Phys. Rev. Lett.* **93**, 246404 (2004).
2. For example, F. Reinert, R. Claessen, G. Nicolay, D. Ehm, S. Hüfner, W. P. Ellis, G.-H. Gweon, J. W. Allen, B. Kindler and W. Asmus, *Phys. Rev. B* **58**, 12808 (1998).
3. K. Yoshikawa, H. Sato, M. Arita, Y. Takeda, K. Hiraoka, K. Kojima, K. Tsuji, H. Namatame and M. Taniguchi, *Phys. Rev. B* **72**, 165106 (2005).
4. S. Ishihara, K. Ichiki, K. Abe, T. Matsumoto, K. Mimura, H. Sato, M. Arita, E. F. Schwier, H. Iwasawa, K. Shimada, H. Namatame, M. Taniguchi, T. Zhuang, K. Hiraoka and H. Anzai, *J. Electr. Spectrosc. Relat. Phenom.* **220**, 66 (2017).
5. P. Blaha, K. Schwarz, G. Madsen, D. Kvasicka and J. Luitz, WIEN2k, *An Augmented Plane Wave Plus Local Orbitals Program for Calculating Crystal Properties* (TU Vienna, Vienna, 2001).

Three-Dimensional Band Structure Characteristics of the Magnetic Topological Insulator MnBi_2Te_4

Yu-Jie Hao^a, Rui'e Lu^a, M. Arita^b, Chang Liu^a, Chaoyu Chen^a

^a Shenzhen Institute for Quantum Science and Engineering (SIQSE) and Department of Physics, Southern University of Science and Technology (SUSTech), Shenzhen 518055, China.

^b Hiroshima Synchrotron Radiation Center, Hiroshima University, Higashi-Hiroshima, Hiroshima 739-0046, Japan

Keywords: MnBi_2Te_4 , Antiferromagnetic topological insulator, Gapless surface state

The recently discovered antiferromagnetic (AFM) topological insulators MnBi_2Te_4 [1-3] has sparked extensive research interest, because it is predicted to be able to realize rich exotic physical phenomena, such as quantum anomalous Hall effect (QAHE) [4, 5] and axion electrodynamics [6]. Early theoretical calculations and angle resolved photoemission spectroscopy (ARPES) measurements have pointed out that the surface state of MnBi_2Te_4 is gapped. However, we have observed a gapless Dirac cone band structure at the (0001) surface of MnBi_2Te_4 by using high-resolution ARPES, which is not the same as previously reported. Such an unexpected band structure remains unchanged across the T_N , and is even robust against severe surface degradation. In order to further explore electronic band structure of MnBi_2Te_4 , we performed systematically electronic band structure measurements on MnBi_2Te_4 with different photon energies at BL09A. The crystals were cleaved at 15 K (below the Néel temperature 24.4 K) and measured at 10 K.

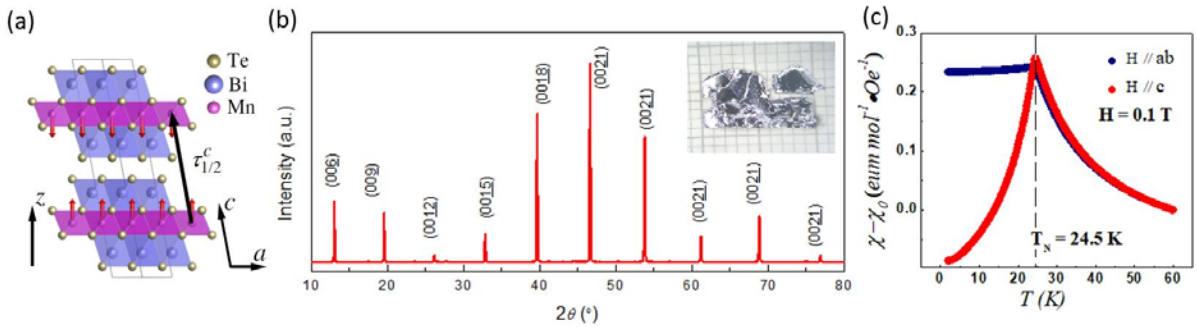


FIGURE 1. Crystal characterization and magnetic responses of MnBi_2Te_4 . (a) Crystal structure and A-type AFM magnetic configuration. (b) Single crystal x-ray diffraction data. Inset: Crystal against a millimeter grid. (c) Magnetization curves in two different configurations, $H||ab$ and $H||c$.

The MnBi_2Te_4 is a van der Waals compound, consisting of seven atomic layers that arrange as Te-Bi-Te-Mn-Te-Bi-Te [1-3] [Figure 1(a)]. We synthesized the samples by flux method. Figure 1(b) shows single crystal x-ray diffraction data and photograph of crystals. Figure 1(c) shows the magnetization versus temperature curves for two different configurations, $H||ab$ and $H||c$. An AFM-paramagnetic (PM) transition is found at $T_N = 24.4$ K.

We show the electronic band structure of MnBi_2Te_4 obtained by the ARPES at BL09A in Figure 2. We performed a detailed photon energy dependent ARPES map from 6 to 36 eV. Figure 2(a) shows kz dispersion map at Γ , from 9 eV to 25 eV photon energy with 1 eV step. The results clearly show the periodic evolution of conduction band minima (CBM) and valence band maxima (VBM), which reveals the bulk nature of these gapped bands. Figure 2(b) shows k - E maps along M - Γ - M taken at 10 eV, 12 eV ... 20 eV, respectively. According to 10 eV, 12 eV, 14 eV and 16 eV k - E maps, the Dirac point negligible change in the (k , E) position. Therefore, the gapless Dirac band structure is a surface state, which behaves as a quasi-2D. Our experimental data taken at $h\nu = 20$ eV is similar to the results reported in the previous paper which is

measured by helium lamp. Now we can conclude that the so called “gapped” surface state observed previously is actually the bulk band.

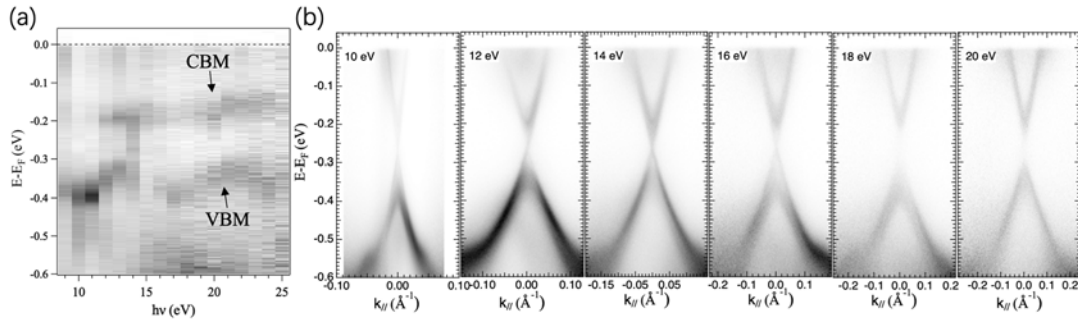


FIGURE 2. Surface and bulk electronic band structure of MnBi_2Te_4 . (a) k_z dispersion map at Γ , taken with 9–25 eV photon energy. Periodic dispersion pattern on the VBM is seen clearly. (b) k -E maps along M - Γ - M taken at 10 eV, 12 eV, 14 eV, 16 eV, 18 eV, 20 eV respectively. It is clear that the gapless state forming the Dirac cone has no k_z dispersion, while the gap of bulk band is consequently changing. VBM, valence band maxima; CBM, conduction band minima.

REFERENCES

1. M. M. Otrokov *et al.*, *Nature* **576**, 416 (2019)
2. Z. S. Aliev *et al.*, *J. Alloys Compd.* **789**, 443 (2019).
3. M. M. Otrokov *et al.*, *Phys. Rev. Lett.* **122**, 107202 (2019)
4. R. Yu *et al.*, *Science* **329**, 61 (2010)
5. C.-Z. Chang *et al.*, *Science* **340**, 167 (2013)
6. Xiao *et al.*, *Phys. Rev. Lett.* **120**, 056801 (2018).

High-resolution Photoemission Study of RuAs

D. Ootsuki ^a, T. Ishida ^a, Y. Yuzawa ^a, M. Arita ^b, D. Hirai ^c, H. Takagi ^{d,e},
T. Mizokawa ^f and T. Yoshida ^a

^a Grad. Sch. of Human & Environmental Studies, Kyoto University, Sakyo-ku, Kyoto 606-8501, Japan,

^b Hiroshima Synchrotron Radiation Center, Hiroshima University, Higashi-Hiroshima, 739-0046, Japan.

^c Institute for Solid State Physics, University of Tokyo, 5-1-5 Kashiwanoha, Kashiwa, 277-8581, Japan.

^d Department of Physics, University of Tokyo, 7-3-1 Hongo, Bunkyo-ku, Tokyo 113-0033, Japan.

^e Max Plank Institute for Solid State Research, Heisenbergstrasse 1, D-70569 Stuttgart, Germany.

^f Department of Applied Physics, Waseda University, Shinjuku-ku, Tokyo 169-8555, Japan.

Keywords: Ru pnictides, Photoemission spectroscopy, metal to nonmagnetic insulator transition

MnP-type pnictides $RuPn$ ($Pn = P, Sb$ and As) have a distorted NiAs-type structure, in which the $RuPn_6$ octahedra share their edges and faces to form a three-dimensional structure. RuP (RuAs) shows a metal to insulator (MI) transition at $T_{MI} = 270$ K (200 K) and the pseudogap (PG) transition at $T_{PG} = 330$ K (270 K) with the reduction of the magnetic susceptibility [1]. However, the single crystal RuP shows two distinct metal to metal transitions at $T = 320$ K and 270 K [2]. Thus, there is a discrepancy between the single crystal and the polycrystalline RuP. Recently, the single crystal RuAs was successfully synthesized by Kotegawa *et al.* [3]. The single crystal RuAs shows the MI transitions at $T_{MI1} = 255$ K and $T_{MI2} = 195$ K without the difference between the single crystal and polycrystalline RuAs.

In this study, we have performed the photoemission spectroscopy of the single crystal RuAs in order to clarify the electronic structure and the origin of the MI transition. The photoemission spectroscopy was carried out at BL-9A of Hiroshima synchrotron radiation center (HiSOR). The total energy resolution was ~ 16 meV for the incident photon energy $h\nu = 21$ eV. The Fermi level (E_F) was calibrated by using the Fermi edge of the gold reference samples.

Figure 1 shows the near- E_F photoemission spectra as a function of temperature. The spectral shape is similar to that of the polycrystalline RuP [4]. The spectral intensity near E_F strongly depends on temperature. To identify the spectral weight change near E_F , we divided the spectra by the Fermi-Dirac distribution function convoluted with the energy resolution as shown in Fig. 1 (b). The spectral weight near E_F is gradually suppressed with decreasing temperature. The spectral weight does not substantially change from $T = 280$ K to 200 K. This tendency agrees with the absence of the spectral difference between the pseudogap phase and the metallic phase in the previous photoemission study on polycrystalline RuP [4]. The spectral

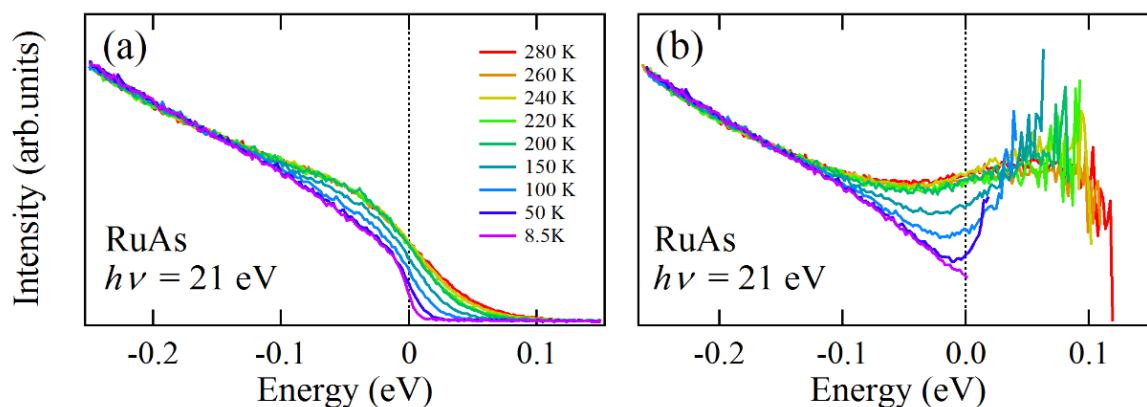


FIGURE 1. (a) Photoemission spectra of single crystal RuAs as a function of temperature. (b) Photoemission spectra divided by Fermi-Dirac distribution functions for each temperature convoluted with the energy resolution. The data were taken at $h\nu = 21$ eV.

weight decreases across $T = 200$ K, which is consistent with the previous photoemission studies on the single crystal RuAs [5] and the polycrystalline RuP [4]. In contrast to the electrical resistivity showing the highly insulating ground state below T_{MI} , the clear Fermi-edge is observed in the photoemission spectrum even at $T = 8.5$ K. This result suggests that the metallic surface state is realized in the low temperature insulating phase.

REFERENCES

1. D. Hirai, T. Takayama, D. Hashizume, and H. Takagi, Phys. Rev. B **85**, 140509 (R) (2012).
2. R. Y. Chen, Y. G. Shi, P. Zheng, L. Wang, T. Dong, and N. L. Wang, Phys. Rev. B **91**, 125101 (2015).
3. H. Kotegawa, K. Takeda, Y. Kuwata, J. Hayashi, H. Tou, H. Sugawara, T. Sakurai, H. Ohta, and H. Harima, Phys. Rev. Mater. **2**, 055001 (2018).
4. D. Ootsuki, K. Sawada, H. Goto, D. Hirai, D. Shibata, M. Kawamoto, A. Yasui, E. Ikenaga, M. Arita, H. Namatame, M. Taniguchi, T. Toriyama, T. Konishi, Y. Ohta, N. L. Saini, T. Yoshida, T. Mizokawa, and H. Takagi, Phys. Rev. B **101**, 165113 (2020).
5. Y. Nakajima, Z. Mita, H. Watanabe, Y. Ohtsubo, T. Ito, H. Kotegawa, H. Sugawara, H. Tou, and S. Kimura, Phys. Rev. B **100**, 125151 (2019).

ARPES study of non-uniform charge transfer and circular dichroism in Vanadium intercalated NbS₂

Mario Novak ^a, XiaoXiao Wang ^b, and Akio Kimura ^b

^a Faculty of Science, University of Zagreb, 10000 Zagreb, Croatia

^b Graduate School of Science, Hiroshima University, 739-8526 Higashihiroshima, Japan

Keywords: Intercalated NbS₂, dichroism of surface states

We have carried on extensive ARPES studies of magnetically ordered Vanadium intercalated single crystals NbS₂. Vanadium atoms are located in the van der Waals gap. The measured samples were p-type fully doped with stoichiometric formula VNb₃V₆. The measurements were done below, and above the magnetic ordering transition of 65 K. The high-quality mapping of the band structure of VNb₃S₆ is used for comparison with other transition metal intercalated dichalcogenides such as CrNb₃S₆ and CrNb₃Se₆ to understand the effect of intercalation and origin of magnetic ordering. Obtained information on the band structure will be in the future compared with DFT calculations to estimate the strength of the on-site interaction parameters to get a better understanding of how the band structure accommodates intercalated atoms and to test if the rigid-band model is an appropriate model. The dichroism at the Fermi level was detected at Γ point and K point of the 1st Brillouin zone.

Photoemission study of mechanical polished SmB_6 [110] surface

M. Arita¹, H. Sato¹, K. Shimada¹, H. Namatame¹, M. Taniguchi¹, H. Tanida², Y. Osanai³, K. Hayashi³, F. Iga⁴

¹Hiroshima Synchrotron Radiation Center, ²Graduate School of Advanced Sciences of Matter,

Hiroshima University, Kagamiyama, Higashi-Hiroshima 739-0046, Japan

³Graduate School of Science and Engineering, ⁴College of Science, Ibaraki University, Mito, Ibaraki, 310-8512, Japan

SmB_6 is well known as Kondo insulator, the energy gap of which opens below ~ 100 K. It was a first topological Kondo insulator [1]. The spin-polarized surface band structure near the Fermi level (E_F) around \bar{X} has been observed by spin-resolved ARPES(SR-ARPES) for SmB_6 (001) [2], so that the SmB_6 is confirmed topological Kondo insulator. On the other hand, as SmB_6 (001) surface takes some kind of structure e.g. 1×1 , 2×1 , and the surface of the Sm or B termination is polar, there are some different variations of the ARPES spectra.

SmB_6 [110] surface is non-polar because Sm^+ and B_6^- with opposite charges lie in-plane. Thus, E_F shift due to the band bending effect is expected to disappear in the surface band structure. The [110] surface was prepared by mechanical polishing orientated with Laue image. In the vacuum chamber, the cycle of the ion sputter and 1050 K annealing was continued until taking a clear rectangular 1×1 LEED image (Fig. 1).

Figures 2 shows the Fermi surface (FS) map taken by ARPES for $h\nu = 19$ eV at 15 K. These are the in-gap state, as the bulk electronic state of SmB_6 has c-f hybridization band gap around E_F at 15 K. The observed FS's are similar to ones observed in [001] surface except around $\bar{\Gamma}$. The two elliptical electron-FS's are centered at $(k_x, k_y) = (0, 0.76)$ and $(0.53, 0)$, which correspond to the \bar{X} and \bar{Y} points of the [110] surface Brillouin Zone (BZ). In neither 1st nor 2nd BZ, a circular-type FS centered around $\bar{\Gamma}$ does not found. The band folding due to the surface reconstruction as in [001] surface does not occur in [110] surface.

According to the result of the SR-ARPES measurements of SmB_6 [111] surface, the parity of the filled band at the high symmetry points is assumed to be $(\Gamma, X, M, R) = (\pm 1, \mp 1, \pm 1, \pm 1)$ [3]. Therefore, it cannot be concluded that both FS's of the in-gap state is derived by the topological surface state.

[1] T. Takimoto et al., J. Phys. Soc. Jpn. 80, 123710 (2011).

[2] N. Xu et al., Nat. Commun. 5, 4566 (2014).

[3] Y. Ohtsubo et al., Nature Communications 10, 2298 (2019)

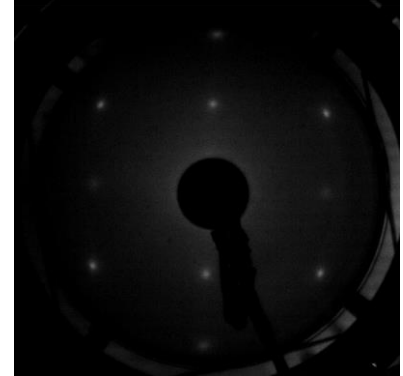


Fig.1 LEED image of SmB_6 [110] for $E = 110$ eV.

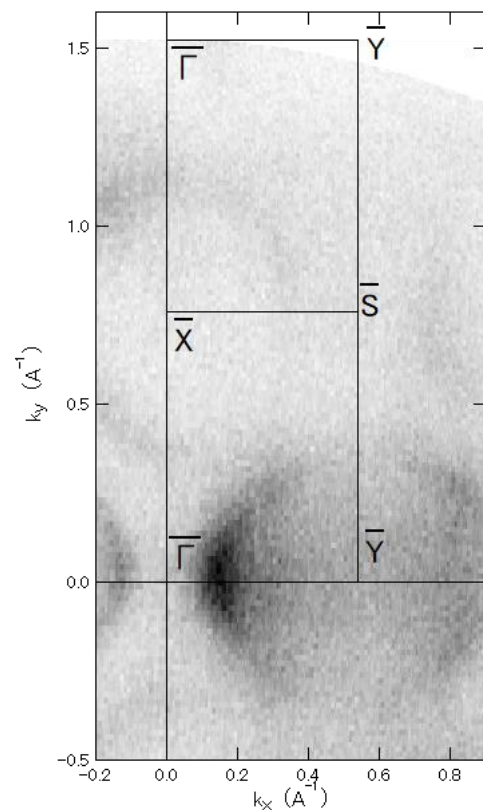


Fig.2 ARPES image of FeSi [110] with $h\nu = 19$ eV at 15 K.

Photon Energy Dependent ARPES Study on Magnetic Topological Insulators $\text{Mn}(\text{Bi}_{1-x}\text{Sb}_x)_2\text{Te}_4$

Yu-Jie Hao^a, Xiao-Ming Ma^a, Ke Zhang^b, Rui'e Lu^a, Meng Zeng^a, Xiang-Rui Liu^a, M. Arita^b, Eike F. Schwier^b, Shiv Kumar^b, Kenya Shimada^b, Chaoyu Chen^a, Chang Liu^a

^a Shenzhen Institute for Quantum Science and Engineering (SIQSE) and Department of Physics, Southern University of Science and Technology (SUSTech), Shenzhen 518055, China.

^b Hiroshima Synchrotron Radiation Center, Hiroshima University, Higashi-Hiroshima, Hiroshima 739-0046, Japan

Keywords: $\text{Mn}(\text{Bi}_x\text{Sb}_{1-x})_2\text{Te}_4$, antiferromagnetic topological insulator, gapped Dirac Cone

The quantum anomalous Hall effect (QAHE) is a quantized Hall effect without any external magnetic field, which has attracted tremendous attentions for its potential applications in electronic and spintronic devices [1-2]. Magnetic topological insulator (MTI) is considered to be one of the most promising topological matter to realized QAHE in relatively high temperature. The MnBi_2Te_4 was recently reported to be the first intrinsic stoichiometric Antiferromagnetic topological insulators (AFM-TI) [3-5]. However, the Dirac Cone surface state is below the Fermi level. As previously study found that the Fermi level of $\text{Mn}(\text{Bi}_{1-x}\text{Sb}_x)_2\text{Te}_4$ can be tuned from the conduction bands to the valence bands by adjusting the atomic ratio x of bismuth to antimony [6]. As the doping amount of antimony increases, its Néel temperature will decrease slightly, and the magnetoresistive behavior will also change. In order to further explore electronic band structure of $\text{Mn}(\text{Bi}_{1-x}\text{Sb}_x)_2\text{Te}_4$, we performed systematically electronic band structure measurements on $\text{Mn}(\text{Sb}_x\text{Bi}_{1-x})_2\text{Te}_4$ with different photon energies at BL09A.

Figure 1 shows our ARPES data taken on a typical $\text{Mn}(\text{Bi}_{1-x}\text{Sb}_x)_2\text{Te}_4$ sample with a nominal x value of 0.075 at $T = 10$ K (below $T_N \sim 25$ K). Figure 1(a) shows the detailed photon energy dependent ARPES map from 6.5 eV to 23 eV photon energy with step of 0.5 eV. The results clearly show the periodic evolution of conduction band minima (CBM) and valence band maxima (VBM), which reveals the bulk nature of these gapped bands. Figure 1(b) shows raw and second derivative ARPES k -E maps along M - Γ - M taken at 6.5 eV, 7.5 eV 14.5 eV, respectively. According to the second derivative ARPES k -E maps, we can find a gap band beside the bulk band and it negligible change in the (k, E) position, indicating a quasi-2D character. We can therefore unambiguously conclude that the surface state of $\text{Mn}(\text{Bi}_{1-x}\text{Sb}_x)_2\text{Te}_4$ is gapped.

We already put the article containing the data of this measurement on arxiv.org with tracking number arXiv:2004.09123.

REFERENCES

1. R. Yu *et al.*, Science **329**, 61 (2010)
2. C.-Z. Chang *et al.*, Science **340**, 167 (2013)
3. M. M. Otrokov *et al.*, Nature **576**, 416 (2019)
4. Z. S. Aliev *et al.*, J. Alloys Compd. **789**, 443 (2019).
5. M. M. Otrokov *et al.*, Phys. Rev. Lett. **122**, 107202 (2019)
6. B. Chen *et al.*, Nat. Commun. **10**, 056801 (2018).

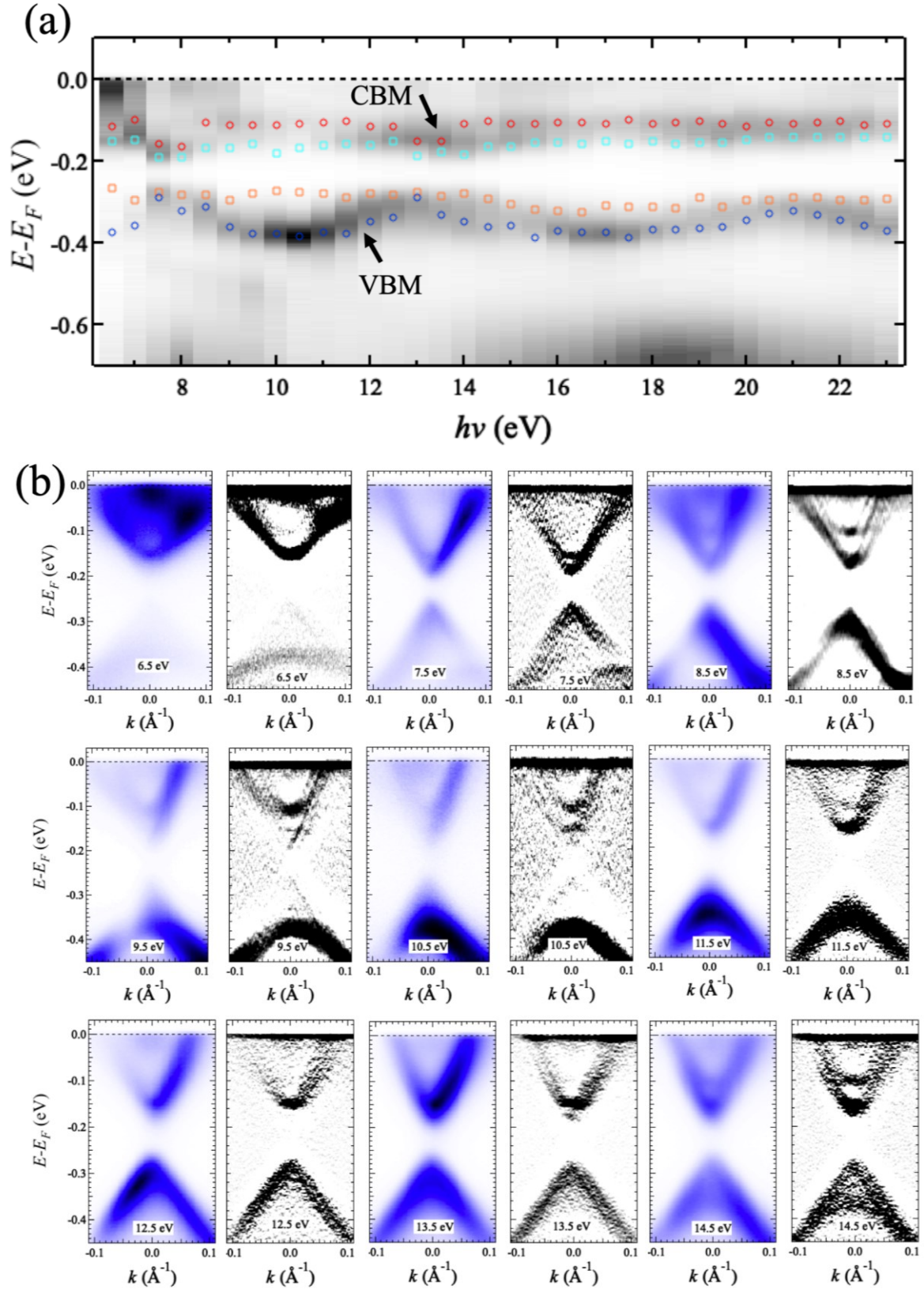


FIGURE 1. Surface and bulk electronic band structure of $\text{Mn}(\text{Bi}_x\text{Sb}_{1-x})_2\text{Te}_4$ ($x = 0.075$). (a) k_z dispersion map at Γ , taken with 6.5–23 eV photon energy. Periodic dispersion pattern on the VBM is seen clearly. (b) k - E maps along M - Γ - M taken at 6.5 eV, 7.5 eV, 8.5 eV, 9.5 eV, 10.5 eV, 11.5 eV, 12.5 eV, 13.5 eV, 14.5 eV respectively. It is clear that the gaped state forming the Dirac cone has no k_z dispersion, while the gap of bulk band is consequently changing. VBM, valence band maxima; CBM, conduction band minima.

Radial Spin Texture in Elemental Tellurium with Chiral Crystal Structure

M. Sakano^{a,b}, T. Takahashi^c, S. Akebi^a, M. Nakayama^a, K. Kuroda^a, K. Taguchi^d, T. Yoshikawa^d, K. Miyamoto^e, T. Okuda^e, N. Mitsuishi^a, K. Ishizaka^{a,f}, S. Shin^a, T. Sasagawa^c, and Takeshi Kondo^{a,g}

^a*Institute for Solid State Physics (ISSP), The University of Tokyo, Kashiwa, 277-8581, Japan*

^b*Quantum-Phase Electronics Center (QPEC) and Department of Applied Physics, The University of Tokyo, Bunkyo-ku, Tokyo, 113-8656, Japan*

^c*Materials and Structures Laboratory (MSL), Tokyo Institute of Technology, Yokohama, Kanagawa, 226-8503, Japan.*

^d*Graduate School of Science, Hiroshima University, Higashi-Hiroshima, Hiroshima, 739-8526, Japan*

^e*Hiroshima Synchrotron Radiation Center (HiSOR), Hiroshima University, Higashi-Hiroshima, Hiroshima, 739-0046, Japan*

^f*RIKEN Center for Emergent Matter Science (CEMS), Wako, Saitama, 351-0198, Japan*

^g*Trans-scale Quantum Science Institute, The University of Tokyo, Bunkyo-ku, Tokyo 113-0033, Japan*

Keywords: Tellurium, chiral, spin-resolved ARPES

The chiral crystal structure is defined by the lack of mirror symmetry, giving rise to two inequivalent crystals, so-called right- and left-handed crystals, which show opposite physical responses in the magnetoelectric effect. This structure is also intriguing in that the spin degeneracy should be lifted in momentum space (\mathbf{k} -space), even in nonmagnetic materials, by the combination of the spin-orbit interaction (SOI) and the breaking of inversion symmetry. Recently, Tsirkin *et al.* have revealed that the spin-orbit coupled bands of chiral crystals can play an important role in various gyrotropic effects [8].

In this study, we have investigated the spin and electronic structure in elemental tellurium by the spin- and angle-resolved photoemission spectroscopy (SARPES) measurement at BL-9B in HiSOR. The elemental tellurium is the simplest material with a chiral structure [16] consisting of atomic spiral chains along the z -axis.

Figures 1(b)-1(d) show the SARPES spectra for the left-handed crystal, measured at the \mathbf{k} -points around the H-point indicated as #1-#13 in Figs. 1(a) and 1(e) (emission angles from -9.0 deg. to 9.0 deg.); each panel corresponds to the x , y , and z component of the spin magnetic moment [m_x , m_y , and m_z , respectively] defined parallel to the orthogonal axes in Figs. 1(a) and 1(b). Significantly, the spectra for m_z [Fig 1(d)] show a clear difference between the spin-up (red) and spin-down (blue) intensities, and the relationship between the two is reversed across the H-point (#7, or the zero-emission angle). These contrasts to the other components (m_x and m_y), which show nearly equivalent intensities for the spin-up and spin-down. Since the measured \mathbf{k} -points of #1-#13 [blue circles in Fig. 1(a)] are aligned nearly parallel to the k_z direction, our SARPES results demonstrate the hedgehog-like radial spin texture formed around the H-point in the highest valence band, which is characteristic in a chiral crystal structure. The spin-polarized band dispersion experimentally determined is exhibited in Fig. 1(f), which maps the z component (P_z) of spin polarization corresponding to the ARPES image in Fig. 1(e). The red and blue circles in the panel plot the peak positions marked in Fig. 1(d) for the SARPES spectra of m_z . The data clearly illustrates the outward and inward radial spin textures in the highest and second-highest bands, respectively. The H'-point is another BZ corner inequivalent with the H-point, and thus the same outward radial spin textures are expected around it for the left-handed crystal, since these two points are mutually linked by the time-reversal and D_3 symmetry. Our experiments have indeed confirmed it, as demonstrated in Fig. 1(h): the upper and middle SARPES spectra obtained at #5' and #5' close to the H'- and H-point, respectively, are almost identical. To further demonstrate the specific feature in chiral crystals, we have also measured a crystal with the opposite chirality

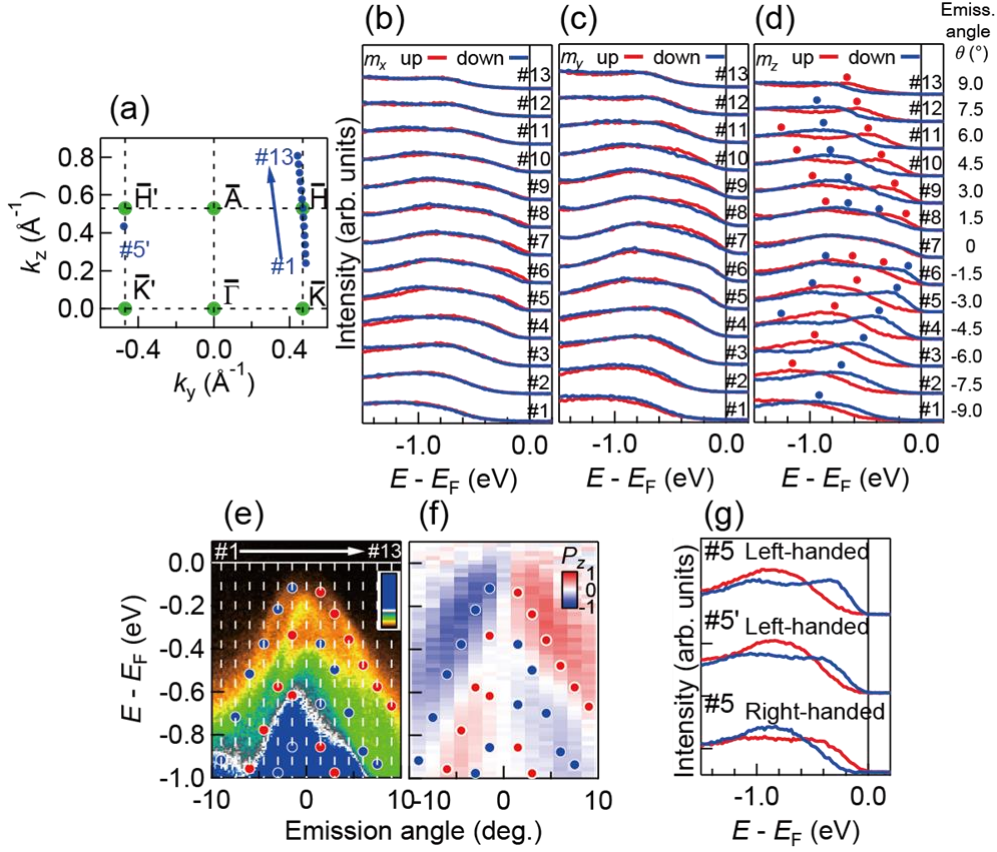


FIGURE 1. (a) The projected two-dimensional Brillouin zone with the k -points (#1-#13, and #5' marked by blue circles) measured by the spin-resolved ARPES. (b)-(d) Spin-resolved energy distribution curves (EDCs) for the left-handed crystal recorded at $h\nu = 18$ eV for the spin magnetic moments along the xyz crystal axes (m_x , m_y and m_z), respectively. Each EDC is labeled by #1-13 in (a). Hereafter, red (blue) color indicates the spin-up (down) component. The markers of red and blue circles indicate the positions of the intensity peaks. (e) ARPES image around the valence band maximum recorded at $h\nu = 18$ eV. White lines represent the measurement cuts for the EDCs in (d). The markers indicate the peak positions of the spin-resolved EDCs, which are also plotted in (d). (f) Spin-resolved ARPES image for the z component (P_z) of spin polarization for the left-handed crystal. The markers are the same as those in e, indicating the peak positions of the spin-resolved EDCs. (g) Calculated spin polarizations along k_z (P_z) for the valence bands. (h) Spin-resolved EDCs at #5 (around H-point) and #5' (around H'-point) for the left-handed crystal, and at #5 (around H-point) for the right-handed crystal, respectively. The k -points of #5 and #5' are shown in (a).

(a right-handed crystal). Very importantly, the z -oriented spin polarizations are observed to be completely inverted from that in the left-handed crystal [see the lower spectra in Fig. 1(h) measured at #5], indicating that the radial spin textures around the H- and H'-points are inward in the case of the right-handed crystal [8,42].

To summarize, the spin texture of a chiral nonmagnetic crystal was experimentally verified for the first time by the SARPES measurements of the elemental trigonal tellurium, which is the simplest material with a chiral structure. Observation of radial spin texture, which becomes inward or outward depending on the winding direction of spiral tellurium-chains, gave a one-to-one correspondence to the chirality of the crystal structure.

REFERENCES

1. S. S. Tsirkin, P. A. Puente, and I. Souza, Phys. Rev. B 97, 035158 (2018).
2. A. J. Bradley, Phil. Mag. 48, 477 (1924).
3. Y. Tanaka, S. P. Collins, S. W. Lovesey, M. Matsumami, T. Moriwaki, and S. Shin, J. Phys. Condens. Matter 22, 122201 (2010).

Spin Polarization Study on Single-Spin Dirac Cones in the Magnetic Kagome Metal Fe_3Sn_2

Xiao-Ming Ma, Yue Feng, Chen Wang, Yu-Jie Hao, Tian-Xiaong Han, Hui-Wen Shen, Yi-Ming Xu and Chang Liu

Shenzhen Institute for Quantum Science and Engineering (SIQSE) and Department of Physics, Southern University of Science and Technology (SUSTech), Shenzhen 518055, China.

Keywords: Magnetic Dirac Cone, Fe_3Sn_2 , Very Low Energy Diffraction.

The kagome lattice, which is named after a Japanese traditional woven bamboo pattern, is a two-dimensional network with mixed hexagons and triangles. Owing to its unique geometry, most of the currently reported compounds promising to be the time reversal symmetry broken topological materials are crystalized in the kagome type lattice [2, 3]. The most direct experimental methods to verify its topology nontrivial nature are the directly electronic band structure and spin polarization measurements on the characteristic electronic bands, which are insufficient for most of the candidates. In this letter, we performed directly spin polarization measurement of the gapped out double Dirac bands in the first experimentally discovered magnetic kagome metal Fe_3Sn_2 by the Very Low Energy Diffraction (VLEED) detector.

The Fe_3Sn_2 single crystals grown by flux method has a layered rhombohedra crystal structure with space group R-3m and hexagonal lattice constants $a = 5.3 \text{ \AA}$ and $c = 19.8 \text{ \AA}$. It consists of two kagome Fe_3Sn layers separated by one layer Sn with honeycomb pattern and detailed crystal structure is shown in Fig. 1 (a). The corresponding Brillouin zone also present hexagonal shape and the picture and the definitions of high symmetry positions are given in Fig 1 (b). We carried out the conventional and spin-resolved ARPES measurements of Fe_3Sn_2 at the BL9A of HiSOR. The constant energy contours was collected with 49 eV photon, and are presented in Fig. (c) and (d) with $E_b = 0 \text{ eV}$ and 0.180 eV , respectively. The Fermi surface presents clear hexagonal shape, which is consistent with the lattice symmetry of the (001) plane of Fe_3Sn_2 .

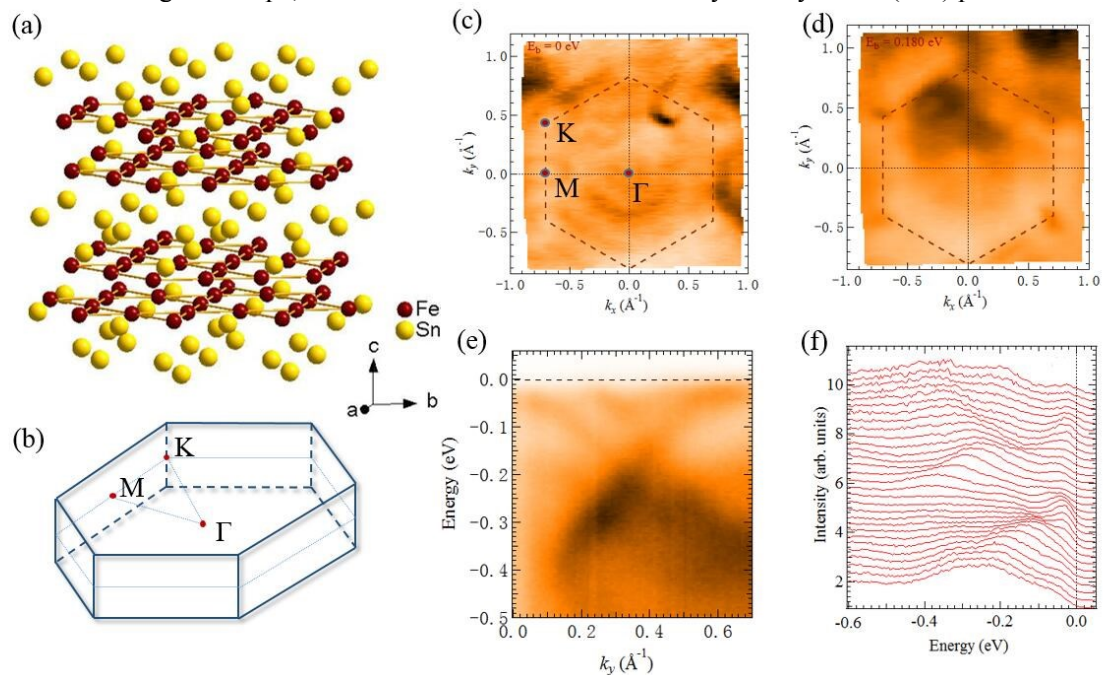


FIGURE 1. (a) is the crystal structure of the Fe_3Sn_2 compound in real space and (b) is the corresponding Brillouin zone with high marked symmetry points. (c) and (d) are the mapping results collected using 49 eV photon energy with $E_b = 0 \text{ eV}$ and 0.180 eV , respectively. (e) is the cut at high symmetry K point along k_y direction and (e) is the corresponding picture of the stack of energy distribution curves.

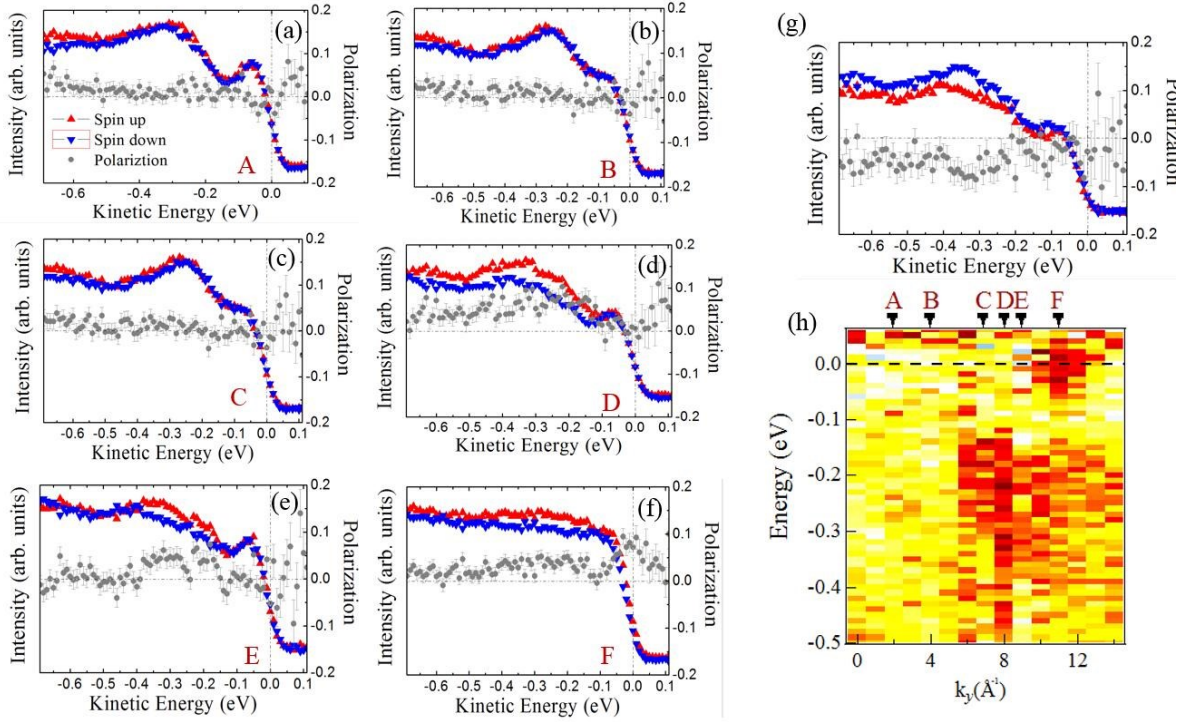


FIGURE 2. The spin-resolved photoemission results of the surface of the Fe_3Sn_2 . (a)-(f) are the spin-resolved spectra with the polarization vector along the y direction and (g) is the corresponding result along z direction of picture (e). Positive and negative spin polarizations are indicated by red and blue colors. Gray lines show spin polarization. The measurement points of (a) to (f) are indicated by red capital letters in the summarized mapping result in (h).

We chose a K position marked in Fig. 1 (c), showing the most distinct band to do the further spin-resolved ARPES measurements. The cut along the k_y direction [given in Fig. 1 (e)] crossing the marked K point presents linear dispersing Dirac like bands and the corresponding stack of energy distribution curves is also given in (f). We performed the spin polarization mapping by the VLEED with y direction magnetization by 1° step for the massive Dirac bands in Fig. 1 (e) and the respective results are plotted in Fig. 2 (a)-(f). The

The summary mapping result by plotting all the y component measurement together in order is give in Fig. 2 (h), in which the portions of the Fig. 2 (a) to (f) are indicated by red capital letters. The the summarized mapping picture in Fig. 2 (h) presents a distinct right half Dirac cone shape. We speculate that the blackout of the left part of the polarization bands maybe highly caused by that the intensity is suppressed by the transition matrix element. Our measurements suggest that the double gapped out Dirac crossings bands are showing the same spin polarization direction for y component with the maximum spin-polarization magnitude $\sim 10\%$, that is consist with the massive Dirac cone nature.

The article of this work is still in preparing.

REFERENCES

- 1 H.-M. Guo and M. Franz, Topological insulator on the kagome lattice, *Phys. Rev. B*, **80**, 113102 (2009).
- 2 H. Yang, Y. Sun, Y. Zhang, W. J. Shi, S. S. P. Parkin and B. Yan, Topological Weyl semimetals in the chiral antiferromagnetic materials Mn_3Ge and Mn_3Sn , *New J. Phys.* **19**, 015008 (2009).
- 3 I. I. Mazin, H. O. Jeschke, F. Lechermann, H. Lee, M. Fink, R. Thomale and R. Valenti, Theoretical prediction of a strongly correlated Dirac metal, *Nat. Commun.* **5**, 42361 (2014).
- 4 L. A. Fenner, A. A. Dee, and A. S. Wills, *J. Phys. Condens. Matter* **21**, 452202 (2009).

Spin-resolved ARPES study on charge density wave material TaTe₂

M. Sakano^a, N. Mitsuishi^a, Y. Takahashi^a, T. Akiba^a,
K. Miyamoto^b, T. Okuda^b, S. Ishiwata^c, K. Ishizaka^a

^a*Quantum-Phase Electronics Center (QPEC) and Department of Applied Physics,
The University of Tokyo, Hongo 113-8656, Japan.*

^b*Hiroshima Synchrotron Radiation Center (HSRC), Hiroshima University,
2-313 Kagamiyama, Higashi-Hiroshima 739-0046, Japan.*

^c*Division of Materials Physics, Graduate School of Engineering Science,
Osaka University, Toyonaka, Osaka 560-8531, Japan.*

Keywords: TaTe₂, topological surface states, charge density wave, spin-resolved ARPES

Since the discovery of topological insulators, a wide variety of topological phases have been intensively developed and established in realistic materials [1, 2]. The upcoming target is to explore the guiding principle toward the manipulation of these topological states. The key to characterize the topological aspect of materials is the band inversion, i.e. the crossing and anti-crossing of multiple bands with opposite parities. In bulk materials, the control of band inversion has been mostly done through the tuning of spin-orbit coupling (SOC) by element substitution [3, 4], with some exceptions related to the topological crystalline insulators [5]. Recently, we have discovered the emergence of topological changes through the charge density wave (CDW) formation in the transition metal dichalcogenides VTe₂ [6]. Considering the CDW's flexible nature to external stimuli, we can also expect to manipulate the CDW-coupled topological state by electric field and optical pulse, leading the novel concepts and applications of topological quantum materials.

To further seek the CDW-coupled topological materials, we here focus on the transition metal ditellurides TaTe₂. TaTe₂ has a distorted CdI₂ (*1T'*) structure (here we refer it as *1T''*) in the high-temperature phase [7]. This superstructure is characterized by the double zigzag chains of metal atoms (Figs. 1 (a) and (b)), which commonly appears in group-V transition metal ditellurides *M*Te₂ (*M* = V, Nb, Ta) [7, 8]. With cooling, TaTe₂ undergoes a phase transition at around 170 K to another CDW phase (LT phase), where a part of Ta atoms are further distorted and tantalum butterfly-like clusters are formed (Fig. 1 (c)) [9].

In this study, we investigate the spin texture of electronic structures in TaTe₂ using spin- and angle-resolved photoemission spectroscopy (ARPES) at BL-9B in HiSOR. Single crystalline TaTe₂ were grown by chemical vapor transport method using I₂ as a transport agent. Samples were cleaved at room temperature in-situ to obtain clean cleavage planes. For spin-resolved measurements, we used a *s*-polarized 21.2 eV light and set the energy and angle resolutions to ~90 meV and ±1.5 deg, respectively.

Figure 2 (a) shows the spin-integrated ARPES spectra collected in the high-temperature *1T''* phase (300 K) along the Brillouin zone boundary at around \bar{M}_1 (see Fig. 1 (d) for the measurement cut). Figure 2 (b) depicts the corresponding spin-resolved energy distribution curves (EDCs) near the \bar{M}_1 point. According to the previous study on the isostructural *1T''*-VTe₂ [6], there exists a Dirac-cone like topological surface state at \bar{M}_1 ranging from 0.5 to 1.5 eV, which is stemming from the band inversion involving V3*d* and Te5*p* bands. In the present study on TaTe₂, such a spin-polarized surface state is not clearly detected in that energy region. This indicates that the topological characters in the *1T''*-structure system sharply depend on the cation sites, which differ in their strength of SOC and energy difference relative to Te5*p* band. On the other hand, we find that the band near the Fermi level shows the spin-up/down contrasts with sign reversal at \bar{M}_1 . Figure 2 (c) compares the spin-resolved EDCs in the *1T''* (300 K) and LT phase (20 K). Both data shows similar spin-up/down contrasts, suggesting that the spin texture associated with this band structure is robust against the *1T''*-LT CDW phase transition. To clarify the origin of this spin texture, further theoretical/experimental studies and analysis are demanded.

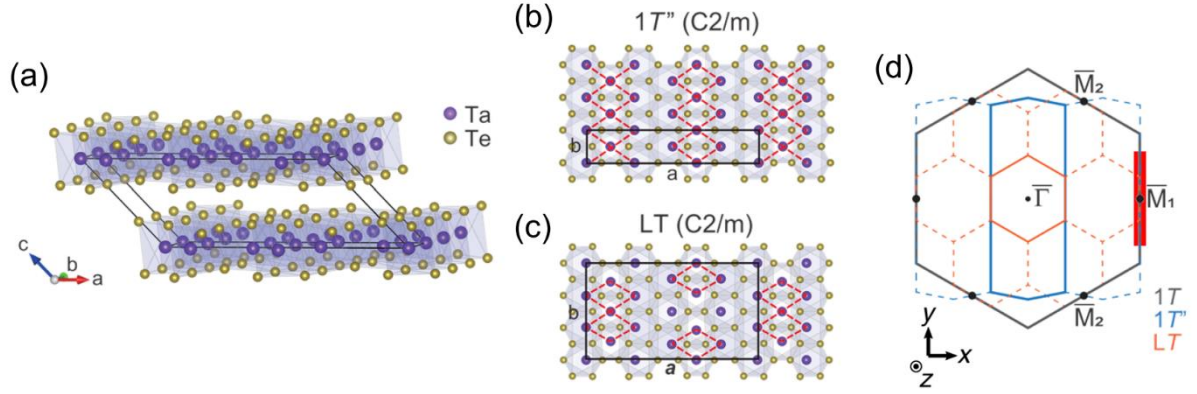


FIGURE 1. Crystal structure and Brillouin zone of TaTe₂. (a) Crystal structure in the high-temperature 1T'' phase. (b) Top view of TaTe₂ layer in the 1T'' phase. The red broken lines highlight the Ta's double zigzag chains. (c) Same as (b), but in the low-temperature LT phase. The red broken lines highlight the Ta's butterfly-like clusters. (d) (0 0 1) 2D Brillouin for virtual 1T (black), 1T'' (light blue), and LT (orange). The (spin-resolved) ARPES data in Fig. 2 were measured along the red line. The spin components were collected along the x direction.

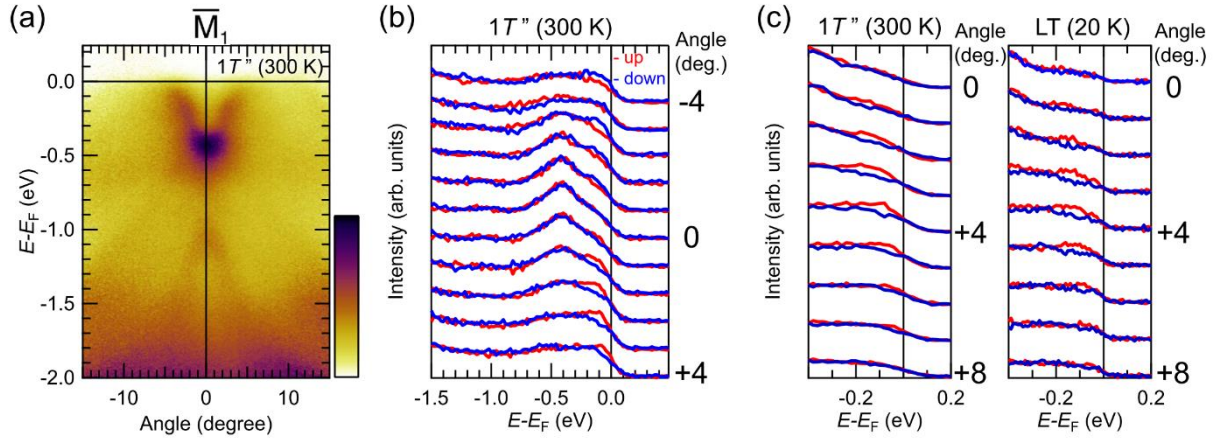


FIGURE 2. Spin-resolve ARPES results on TaTe₂. (a) Spin-integrated ARPES spectra in the 1T'' phase (300 K). (b) Spin-resolved energy distribution curves (EDCs) in 1T''. (c) Temperature-dependence of spin-resolved EDCs for 1T'' (300 K) and LT (20 K).

REFERENCES

1. L. Fu and C. L. Kane, *Phys. Rev. B* **76**, 045302 (2007).
2. M. Z. Hasan and C. L. Kane, *Rev. Mod. Phys.* **82**, 3045-3067 (2010).
3. S. Y. Xu *et al.*, *Science* **332**, 560-564 (2011).
4. T. Sato *et al.*, *Nat. Phys.* **7**, 840-844 (2011).
5. P. Dziawa *et al.*, *Nat. Mater.* **11**, 1023-1027 (2012).
6. N. Mitsuishi *et al.*, *Nat. Commun.* **11**, 2466 (2020).
7. B. E. Brown, *Acta Crystallorg.* **20**, 264-267 (1966).
8. K. D. Bronsema, G. W. Bus, and G. A. Wiegers, *J. Solid State Chem.* **53**, 415-421 (1984).
9. T. Sörgel *et al.*, *Mater. Res. Bull.* **41**, 987 (2006).

Spin-Resolved ARPES Measurement on Magnetic Topological Insulators MnBi_2Te_4

Yu-Jie Hao^a, K. Miyamoto^b, T. Okudad^b, Chang Liu^a

^a Shenzhen Institute for Quantum Science and Engineering (SIQSE) and Department of Physics, Southern University of Science and Technology (SUSTech), Shenzhen 518055, China.

^b Hiroshima Synchrotron Radiation Center, Hiroshima University, Higashi-Hiroshima, Hiroshima 739-0046, Japan

Keywords: MnBi_2Te_4 , Spin-resolved, antiferromagnetic topological insulator

The first discovered antiferromagnetic topological insulator MnBi_2Te_4 [1-3] is predicted to host quantum anomalous Hall effect (QAHE) [4, 5] and axion electrodynamics [6]. MnBi_2Te_4 is a van der Waals compound, consisting of seven atomic layers that arrange as Te-Bi-Te-Mn-Te-Bi-Te. Its magnetic moments in the bulk are theoretically predicted to be ferromagnetically (FM) ordered within a Mn plane pointing along the out-of-plane z direction but antiferromagnetically aligned between adjacent Mn layers, which later confirmed by neutron diffraction experiments. Now, many theoretical studies, transport measurements and angle resolved photoelectron spectroscopy (ARPES) measurements have performed on MnBi_2Te_4 . However, the surface state of MnBi_2Te_4 is still controversial. In order to understand the surface state, we performed the spin-resolved ARPES measurements on MnBi_2Te_4 at BL09B. The crystals were measured at 20 K (below the Néel temperature 24.4 K).

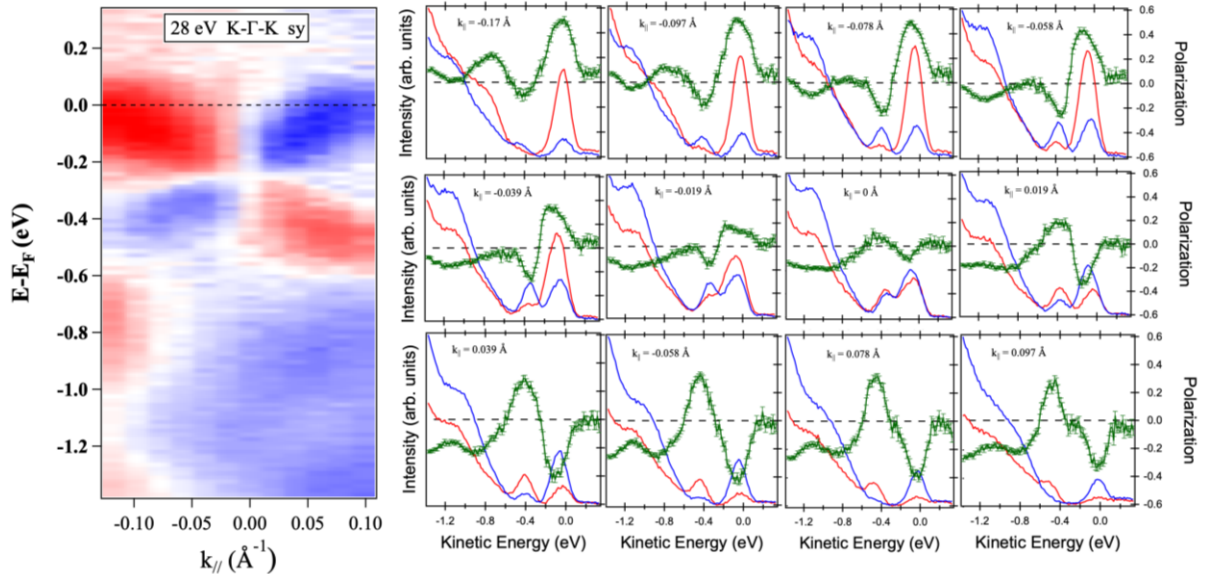


FIGURE 1. The in-plane spin-resolved ARPES results of MnBi_2Te_4 . (a) The in-plane spin-resolved ARPES dispersion maps measured at 28 eV. Positive and negative spin polarizations are indicated by red and blue colors. (b) Energy distribution curves of spin up (red line) and down (blue line) obtained from different momentum positions. Green lines show spin polarization as a function of kinetic energy.

Figure 1 shows the in-plane spin-resolved ARPES dispersion map and the corresponding in-plane polarization of MnBi_2Te_4 . The in-plane spin-resolved ARPES dispersion map measured at 28 eV along K- Γ -K, and a clear helical nature of Dirac state was observed near the Fermi level. In the direction of $k_{||} = 0 \text{ \AA}^{-1}$, the spin reverses. Figure 2 shows the out-of-plane spin-resolved ARPES dispersion map and the corresponding out-of-plane polarization of MnBi_2Te_4 . The strong spin polarization near the Fermi level, the spin polarizations with opposite signs are seen around 0 eV to -0.25 eV then change to positive signs around

-0.3 eV to -1.2 eV.

The present spin-resolved ARPES results indicated that the Dirac band structure match well with topological character.

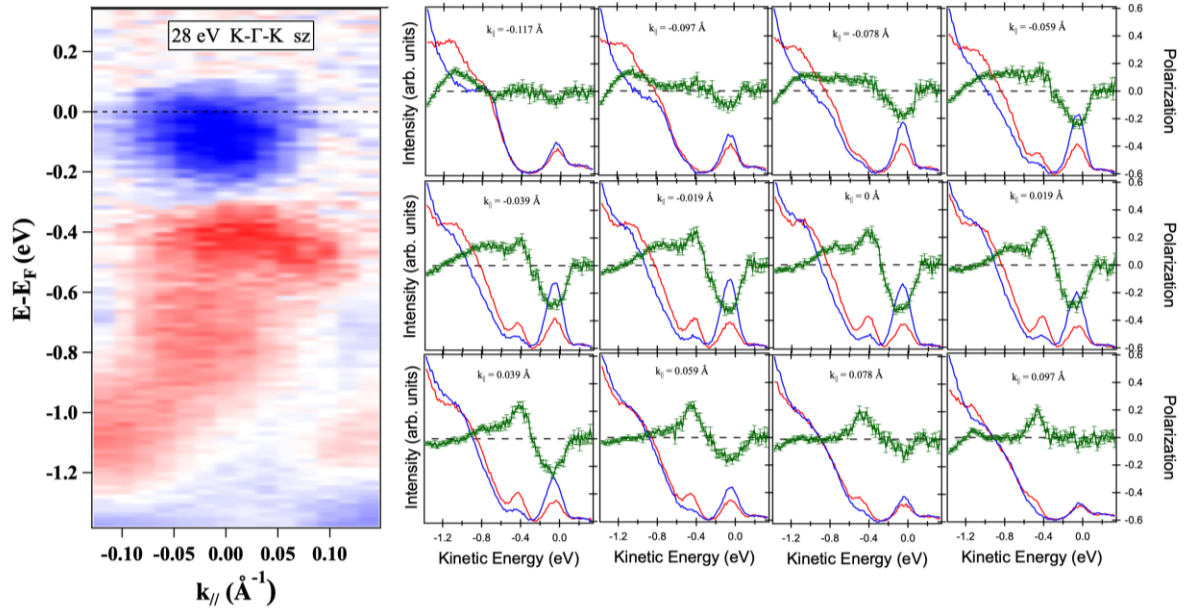


FIGURE 2. The out-of-plane spin-resolved ARPES results of MnBi_2Te_4 . (a) The out-of-plane spin-resolved ARPES dispersion maps measured at 28 eV. Positive and negative spin polarizations are indicated by red and blue colors. (b) Energy distribution curves of spin up (red line) and down (blue line) obtained from different momentum positions. Green lines show spin polarization as a function of kinetic energy.

REFERENCES

1. M. M. Otrokov *et al.*, *Nature* **576**, 416 (2019)
2. Z. S. Aliev *et al.*, *J. Alloys Compd.* **789**, 443 (2019).
3. M. M. Otrokov *et al.*, *Phys. Rev. Lett.* **122**, 107202 (2019)
4. R. Yu *et al.*, *Science* **329**, 61 (2010)
5. C.-Z. Chang *et al.*, *Science* **340**, 167 (2013)
6. Xiao *et al.*, *Phys. Rev. Lett.* **120**, 056801 (2018).

Synchrotron radiation spin-resolved ARPES study for thin film of half-metal Heusler compounds $\text{Co}_2\text{Fe}(\text{Ga}_{0.5}\text{Ge}_{0.5})$

K Goto^{a, b}, Y Sakuraba^b, M. Kakoki^c, T. Kono^c, T. Okuda^d and K Hono^{a, b}

^aGraduate school of Pure and Applied Science, University of Tsukuba, 1-1-1 Tennodai Tsukuba 305-0047, Japan

^bNational Institute for Materials Science, 1-2-1 Sengen, Tsukuba 305-0047, Japan

^cDepartment of Physical Science, Graduate School of Science, Hiroshima University, 1-3-1 Kagamiyama, Higashi-hiroshima 739-8526, Japan

^dHiroshima Synchrotron Radiation Center, Hiroshima University, 2-313 Kagamiyama, Higashi-hiroshima 739-0046, Japan

Keywords: Half-metal Heusler compounds, Spin-resolved ARPES, Temperature dependence of spin polarization

Co-based Heusler compounds such as Co_2MnSi and $\text{Co}_2\text{FeGa}_{0.5}\text{Ge}_{0.5}$ (CFGG) are predicted to have high spin-polarization of the conduction electron at the Fermi level. These materials have been attracting much attention for spintronics devices of tunneling magnetoresistance (TMR) and current perpendicular to plane giant magnetoresistive (CPP-GMR) devices [1-4]. However, observed large reduction of MR ratio with temperature [1, 4] limits a potential of applications using half-metallic Heusler compounds. To understand a cause of this problem, the spin-polarized electronic structure should be observed by spin and angle-resolved photoemission spectroscopy (SARPES) which is the most powerful method for direct measurement of the electronic structure (energy, moment and spin) in the solids.

The CFGG thin film sample which has $L2_1$ structure was prepared by the magnetron sputtering method equipped at National Institute for Materials Science (NIMS) and it was delivered to beam line 9B of Hiroshima Synchrotron Radiation Center (HiSOR) with keeping high vacuum ($\sim 3.0 \times 10^{-10}$ mbar) level by the suitcase chamber. SARPES experiment was performed at the Efficient SPin REsolved SpectroScOpy (ESPRESSO) end station with the very-low-energy-electron-diffraction (VLEED)-type spin polarimeter [5]. Photon energy was set at 66 eV to observe Γ -X line in fcc Brillouin zone. Before SARPES measurement, CFGG thin film was annealed at 500°C for 30 min to obtain a clean surface. The measurement temperature was room temperature and 20 K.

Figure 1(a) and (b) show ARPES image of CFGG along the Γ -X line and spin-resolved energy distribution curves (EDC) for each emission angles θ of 0° (Γ point), 8°, 11°, 13°, 16° (X point), 18° and 20°, respectively. Red markers and blue markers on the figure 1(a) mean the spin character for band structures of CFGG. It was clarified that there is clear the minority hole band around Γ point and the majority electron band around X point. Furthermore, in comparison with theoretical band calculation performed by GGA without electron correlation effect, the experimental band energy is shifted about 0.4 eV to deeper binding energy side from the calculation. This result indicates the necessity of electron correlation effect for band calculation of CFGG.

In conclusion, clear spin-polarized band structure of CFGG was experimentally observed by SARPES

measurement for the first time and the necessity of electron correlation effect in band calculation for CFGG was indicated. Further studies and analysis to evaluate the value of electron correlation effect for CFGG is in progress.

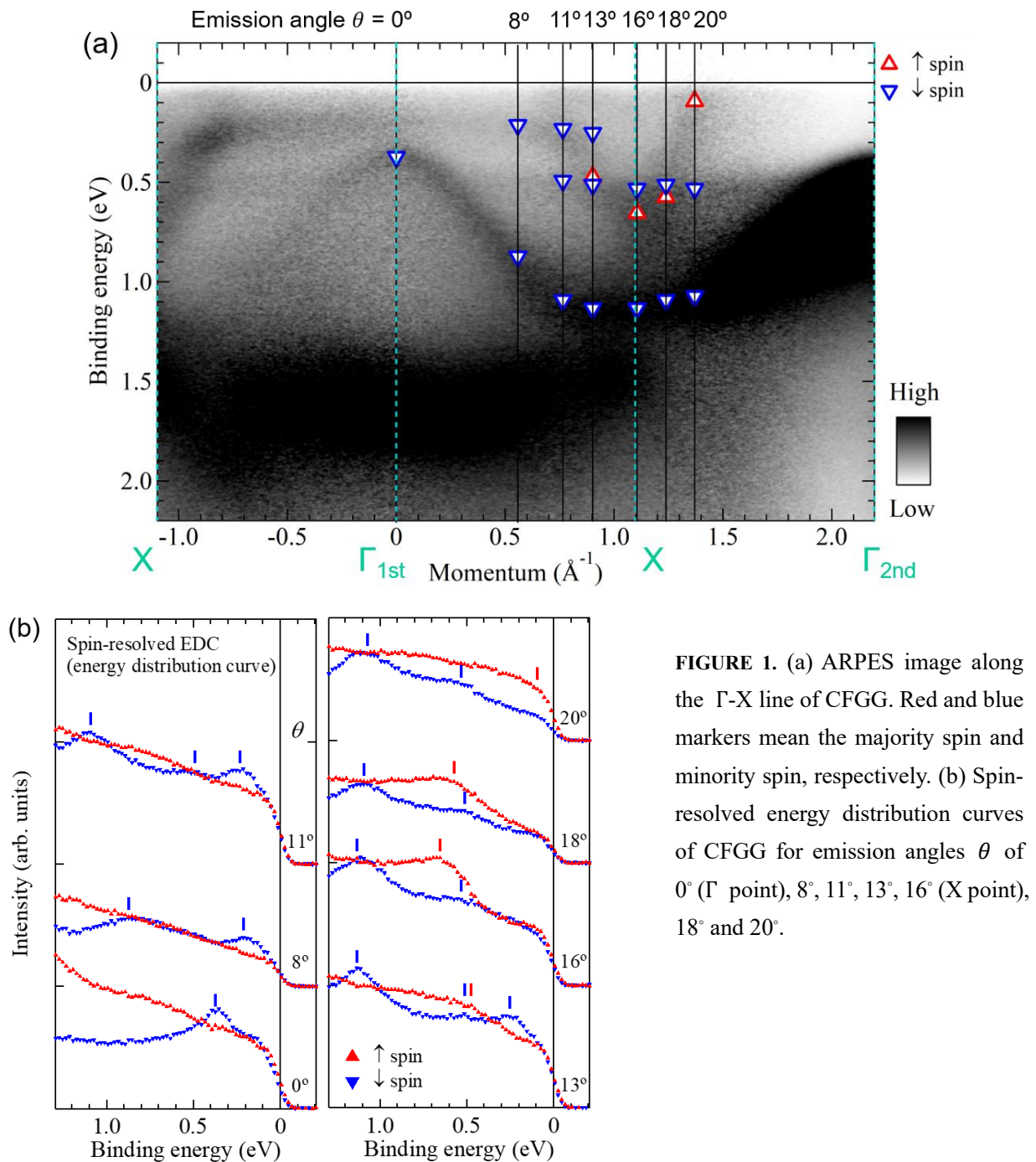


FIGURE 1. (a) ARPES image along the Γ -X line of CFGG. Red and blue markers mean the majority spin and minority spin, respectively. (b) Spin-resolved energy distribution curves of CFGG for emission angles θ of 0° (Γ point), 8° , 11° , 13° , 16° (X point), 18° and 20° .

REFERENCES

1. Y. Sakuraba *et al.*, Appl.Phys. Lett. **88**, 192508 (2006)
2. T. Ishikawa *et al.*, J. Appl. Phys. **103**, 07A919 (2008)
3. S. Li *et al.*, Appl. Phys. Lett. **103**, 042405 (2013)
4. J. W. Jung *et al.*, Appl. Phys. Lett. **108**, 102408 (2016)
5. T. Okuda *et al.*, Rev. Sci. Instrum. **82**, 103302 (2011)

Spin-resolved ARPES study on charge density wave material NbTe₂

M. Sakano^a, N. Mitsuishi^a, K. Miyamoto^b, T. Okuda^b,
H. Takahashi^c, S. Ishiwata^c, K. Ishizaka^a

^a*Quantum-Phase Electronics Center (QPEC) and Department of Applied Physics,
The University of Tokyo, Hongo 113-8656, Japan.*

^b*Hiroshima Synchrotron Radiation Center (HSRC), Hiroshima University,
2-313 Kagamiyama, Higashi-Hiroshima 739-0046, Japan.*

^c*Division of Materials Physics, Graduate School of Engineering Science,
Osaka University, Toyonaka, Osaka 560-8531, Japan.*

Keywords: NbTe₂, topological surface states, charge density wave, spin-resolved ARPES

Topologically nontrivial materials host protected edge states associated with the bulk band inversion through the bulk-edge correspondence [1, 2]. Manipulating such edge states is highly desired for developing new functions and devices practically using their dissipation-less nature and spin-momentum locking. Recently we have revealed that in a transition metal dichalcogenide VTe₂ the charge density wave (CDW) formation induces the huge anisotropic modification of the bulk electronic structure, accompanying the selective disappearance of Dirac-type spin-polarized topological surface states that exist in the normal state [3]. Such CDW-coupled topological materials provide a new way to the topological manipulation of matters by utilizing CDWs' flexible characters to external stimuli. From this viewpoint, here we investigate the spin texture of electronic states in the isostructural NbTe₂ [4] using spin- and angle-resolved photoemission spectroscopy (ARPES) at BL-9B in HiSOR. Single crystalline NbTe₂ were grown by chemical vapor transport method using I₂ as a transport agent. Samples were cleaved at 20 K in-situ to obtain clean cleavage planes. For spin-resolved measurements, we used a *s*-polarized 21.2 eV light and set the energy and angle resolutions to ~90 meV and ±1.5 deg, respectively.

Figure 1 (b) shows the spin-integrated ARPES spectra (20 K) along the Brillouin zone boundary. Note that the data includes multiple signals along different momentum cuts due to the mixing of in-plane 120-deg CDW domains, see Fig. 1 (a) for the measurement region. We find the relatively flat bands lying at around $E - E_F = -0.6$ and -0.8 eV and other dispersive bands. According to the bulk band calculations, these are located in distinct momentum space (i.e. the flat bands are at \bar{M}_2 side while the dispersive bands at \bar{M}_1), which seemingly the similar situation with the isostructural VTe₂ [3]. Figures 1 (c) and (d) are the spin-resolved ARPES spectra respectively for spin-up and -down components along k_x . While flat bands show almost same up/down photoelectron intensities, the dispersive band at around $E - E_F = -1.2$ to -1.0 eV shows the finite up/down contrasts as marked by the black arrows. This result suggests the spin-polarized states (possibly, the topological surface states) exist at around the \bar{M}_1 side, as similarly to the VTe₂ case [3]. For clarifying the topological property in NbTe₂, future theoretical and experimental investigations are desired.

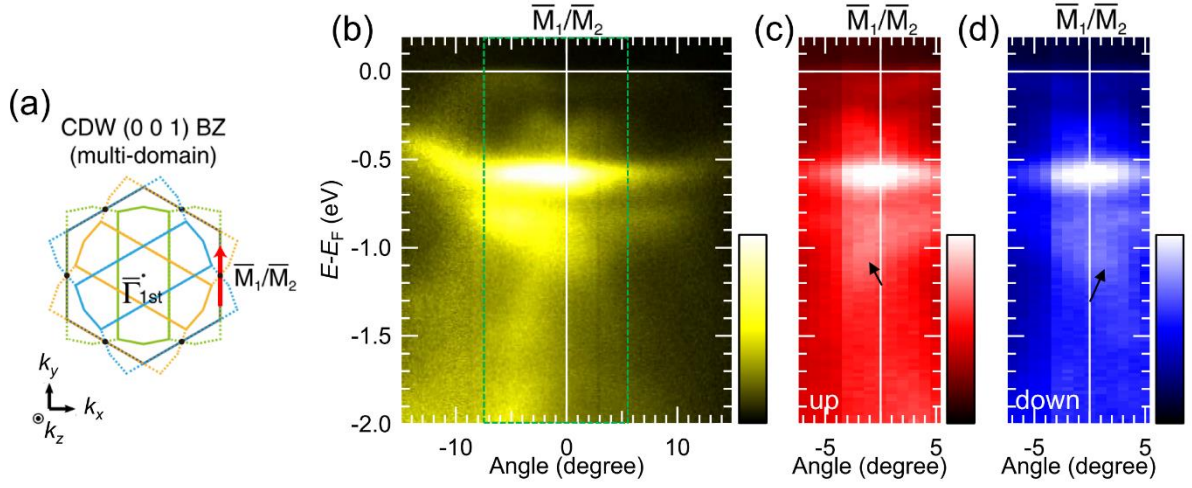


FIGURE 1. Spin-resolve ARPES results on NbTe₂ (20 K, *s*-polarized 21.2 eV light). (a) Schematic 2D Brillouin zone with mixed in-plane CDW domains. The red arrow qualitatively follows the measurement direction. (b) Spin-integrated ARPES spectra. (c, d) The corresponding spin-resolved ARPES spectra for spin-up (c) and spin-down (d) components along k_x .

REFERENCES

1. L. Fu and C. L. Kane, *Phys. Rev. B* **76**, 045302 (2007).
2. M. Z. Hasan and C. L. Kane, *Rev. Mod. Phys.* **82**, 3045-3067 (2010).
3. N. Mitsuishi *et al.*, *Nat. Commun.* **11**, 2466 (2020).
4. B. E. Brown, *Acta Crystallorg.* **20**, 264-267 (1966).

ARPES Study of In-doped (111) $\text{Pb}_x\text{Sn}_{1-x}\text{Te}$ Close to Band Inversion Compositions

Vladimir Golyashov^a, Taichi Okuda^b, Akio Kimura^c, Oleg Tereshchenko^a

^a*Rzhanov Institute of Semiconductor Physics SB RAS, pr. Akademika Lavrentieva 13, Novosibirsk, 630090, Russian Federation*

^b*Hiroshima Synchrotron Radiation Center, Hiroshima University, 2-313 Kagamiyama, Higashi-Hiroshima 739-8526, Japan*

^c*Graduate School of Science, Hiroshima University, 1-3-1 Kagamiyama, Higashi-Hiroshima 739-8526, Japan*

Keywords: topological crystalline insulator, lead tin telluride, electronic structure, angle-resolved photoemission spectroscopy.

One of the most recently proposed topological class of matter is topological crystalline insulator (TCI) [1]. Topological surface states (TSS) of TCI are protected by crystalline symmetry instead of time reversal symmetry in the topological insulators. After the theoretical prediction [2], TCI phase existence was experimentally confirmed for $\text{Pb}_{1-x}\text{Sn}_x\text{Te}$ compound [3]. PbTe-SnTe solid solutions have a rocksalt crystal structure and they are narrow-gap semiconductors. PbTe has a 0.32 eV band gap with normal band ordering, while SnTe has an inverted band structure with $E_g = 0.18$ eV. Therefore, the $\text{Pb}_{1-x}\text{Sn}_x\text{Te}$ compound is expected to undergo a band inversion and topological phase transition at $x \sim 0.35$. But only (001), (111), and (110) crystal surfaces keep the mirror symmetry with respect to the (110) planes of rocksalt structure and are gapless.

The main question associated with topological insulators is controlling bulk conductivity to distinguish surface transport properties. Due to the low energy of native defect formation undoped $\text{Pb}_{1-x}\text{Sn}_x\text{Te}$ films have carrier densities of 10^{18} - 10^{19} cm^{-3} and extrinsic doping is required. The most interesting dopant for this system is indium. For $\text{Pb}_{1-x}\text{Sn}_x\text{Te}$ with $x \sim 0.2$ - 0.35 indium doping provides Fermi level pinning in band gap with insulating bulk properties (resistivity more than 10^3 $\Omega \cdot \text{cm}$) at temperatures below 30K [4]. So, samples with certain x , doped with 1-2 % of indium, can be fully compensated and therefore are absolutely nonconductive at liquid helium temperatures despite very small bulk band gap. All these $\text{Pb}_{1-x}\text{Sn}_x\text{Te}$ compositions are considered to be outside TCI phase, but they are perfect candidates to be used as substrates for thin strained TCI-composition $\text{Pb}_{1-x}\text{Sn}_x\text{Te}$ films in various transport experiments. Furthermore, despite the fact these compositions are trivial insulators, the surface of the films can be enriched by Sn and In during its preparation by annealing in vacuum due to diffusion and sublimation of PbTe . The formation of Sn-enriched strained (due to lattice mismatch) surface layer can induce emergence of the TSS. Possibility of creation of such heterostructures with truly insulating bulk and thin topological insulator surface layer is of great interest, because it allows direct TSS transport properties measurements.

In this work we performed study of the electronic structure of (111) surface of 1-3 % In-doped $\text{Pb}_{1-x}\text{Sn}_x\text{Te}$ films with $x \sim 0.3$ - 0.35 in the close proximity to topological crystalline insulator phase transition boundary. The 1-2 micrometers thick $\text{Pb}_{1-x}\text{Sn}_x\text{Te}$ films were grown by molecular beam epitaxy on (111) oriented BaF_2 substrates. To obtain atomically clean well-ordered surface for angle resolved photoemission spectroscopy (ARPES) measurements, samples were chemically treated in HCl-IPA solution [5] to remove the oxides and then annealed in UHV conditions at 300-370 °C for 10-15 minutes.

It was found that annealing of the HCl-IPA treated In doped $\text{Pb}_{1-x}\text{Sn}_x\text{Te}$ samples leads to significant increase in indium content at their surface (up to 5-10%). A photoemission spectrum of $\text{Pb}_{0.66}\text{Sn}_{0.33}\text{In}_{0.01}\text{Te}$ film surface after chemical treatment in HCl-IPA and annealing at ~ 360 °C temperature is shown in fig. 1 (a). It is seen that besides $\text{Pb}5d$ and $\text{Sn}4d$ photoemission lines quite intensive $\text{In}4d$ line emerges in spectrum, despite the fact that In was not detected just after chemical treatment. This result allows us to

suggest that sample annealing leads to indium diffusion from bulk of the sample to its surface and formation of the high In-content $\text{Pb}_{1-x-y}\text{Sn}_x\text{In}_y\text{Te}$ surface layer. Low energy electron diffraction (LEED) showed formation of (1×1) surface structure at $\sim 330\text{-}350^\circ\text{C}$ sample annealing temperatures, and unusual (9×9) superstructure (fig. 1 (b)) formation after increase in annealing temperature to $360\text{-}370^\circ\text{C}$. Though no surface reconstruction impact on surface electronic structure was found.

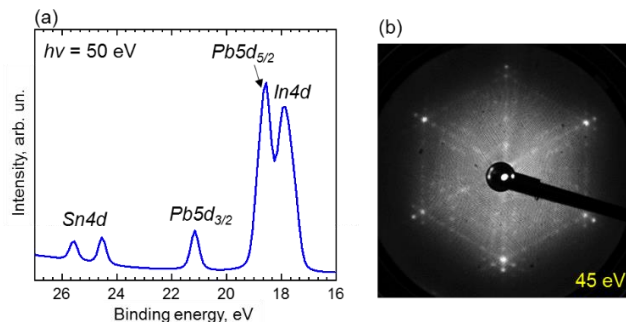


FIGURE 1. (a) Photoemission spectrum of (111) $\text{Pb}_{0.66}\text{Sn}_{0.33}\text{In}_{0.01}\text{Te}$ surface after chemical treatment in HCl-IPA and annealing at $\sim 360^\circ\text{C}$ temperature in UHV, (b) LEED image of the surface with (9×9) reconstruction.

Figure 2 (a-e) shows ARPES spectra of (9×9) reconstructed (111) $\text{Pb}_{0.66}\text{Sn}_{0.33}\text{In}_{0.01}\text{Te}$ surface measured at different photon energies at BL-9B. The valence band states at binding energies > 0.3 eV are heavily dispersing with k_z and can be attributed to “bulk” states of the $\text{Pb}_{1-x-y}\text{Sn}_x\text{In}_y\text{Te}$ surface layer formed. Therefore, the band gap of this composition can be estimated to be more than 0.3 eV. The additional low-density states are clearly visible within the band gap (binding energies 0.1-0.3eV), and can be attributed to topological crystalline insulator surface states. Figure 2 (f) shows cone-like dispersion of this states measured using Laser-ARPES setup at HiSOR. Their intensity reaches maximum at energies $h\nu \sim 17\text{-}19$ eV, corresponding to indium line resonant excitation, and indicating indium states to contribute to surface states formed. However low spin polarization of this states ($\sim 10\%$) was found in this experiment.

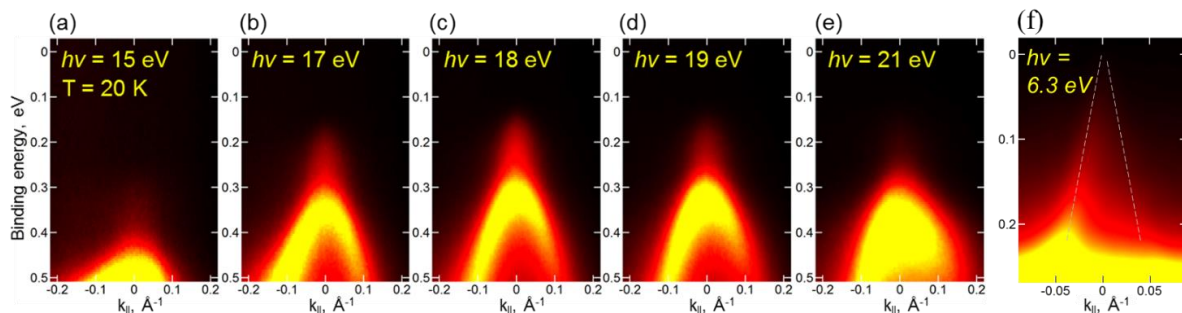


FIGURE 2. (a-e) ARPES spectra of (9×9) - (111) $\text{Pb}_{0.66}\text{Sn}_{0.33}\text{In}_{0.01}\text{Te}$ surface measured at different photon energies, (f) Laser-ARPES spectra of (1×1) - (111) $\text{Pb}_{0.32}\text{Sn}_{0.68}\text{Te}$ surface (Γ -M direction, $T = 20$ K).

REFERENCES

1. L. Fu, et.al. *Phys. Rev. Letters* **106**, 106802 (2011).
2. T.H. Hsieh, et al. *Nature Communications* **3**:982 (2012).
3. S.-Y. Xu, et al. *Nature Communications* **3**:1192 (2012).
4. R. Zhong, et.al. *Crystals* **7**, 55 (2017).
5. V.L. Alperovich, et.al. *Applied Surface Science* **235**, 249–259 (2004).

Study of temperature-induced topological phase transition in TlBiS_2 and TlBiSe_2

Takehito Imai^a, Kazuki Kato^a, Teruo Matsuda^a, Jiahua Chen^a, Koji Miyamoto^b,
Akio Kimura^a and Taichi Okuda^b

^aGraduate school of Science, Hiroshima University, 1-3-1 Kagamiyama, Higashi-Hiroshima 739-8526, Japan

^bHiroshima Synchrotron Radiation Center, Hiroshima University, 2-313 Kagamiyama, Higashi-Hiroshima 739-0046, Japan

Keywords: Topological Insulator, Phase Transition

Topological insulators, which are possessing the spin-polarized surface states with linear dispersion like graphene, have been studied extensively in recent years since the special features of the surface states are considered to be useful for the future spintronics applications. Recently, some theoretical studies predicted that the spin-polarized electronic states caused by spin-orbit interaction in topological insulators or Rashba spin-split states can be modified by external perturbation such as impurity doping, temperature, pressure, electric field, magnetic field and so on [1, 2]. Furthermore, even the topological phase transition from nontrivial to trivial and vice versa is expected in some materials by the theories [1, 3]. $\text{TlBi}(\text{S}_x\text{Se}_{1-x})_2$ is one of the candidates showing such a topological phase transition by the external perturbation. In the system, the topological phase transition has been already reported by changing the ratio of S and Se [1, 4, 5]. That is, the transition from the topologically nontrivial states of TlBiSe_2 into topologically trivial states of TlBiS_2 has been observed at about $x=0.5$ [6]. Furthermore, according to the recent theory, the topologically nontrivial (trivial) state of TlBiSe_2 (TlBiS_2) can be changed into a trivial (nontrivial) state by temperature [1]. In this report, we have observed the temperature dependence of electronic states of the TlBiS_2 and TlBiSe_2 by spin-resolved angle-resolved photoelectron spectroscopy (ARPES and SARPES).

All the experiments have been done at the beamline 9B of Hiroshima Synchrotron Radiation Center (HiSOR). The clean surface of the TlBiS_2 and TlBiSe_2 single-crystal fabricated by the Bridgman method was obtained by cleaving the sample in the ultra-high vacuum. In the ARPES measurement, the p -polarized light at the photon energy of 18 eV impinged into the sample surface at the incident angle of 50 degrees. The band structure of TlBiS_2 has been observed with changing the sample temperature from 50 K to 470 K. While the band structure of TlBiSe_2 has been observed with changing the sample temperature from 50 K to 475 K which is controlled by a temperature controller using the

electric heater in the manipulator with He cryostat.

As a result, in TlBiS_2 , the appearance of the temperature-induced topological surface state is not observed in the measured temperature range. Therefore, no direct evidence of the topological phase transition is obtained. However, the increase of the bandgap between the bulk valence band and the conduction band is observed with increasing temperature. The result is opposite to the trend predicted by theoretical calculation [2]. Therefore, it is expected that the topological phase transition will not occur in TlBiS_2 . One of the possible reasons for this discrepancy between the theory and the experiment is due to the neglect of the effect of thermal lattice expansion in the theoretical calculation [2]. Taking this effect into account, it is expected that the bandgap will increase with increasing temperature by the reduction of bandwidths in bulk conduction and valence bands and the experimental results can be qualitatively understandable.

On the other hand, we have also investigated the temperature dependence of the electronic states of topologically non-trivial TlBiSe_2 , which has been predicted to show different response with temperature in the theory. As a result, it is observed that the topological surface state is maintained even at the maximum temperature of 475 K in the measurement. Therefore, it is found that the topological phase transition does not occur in this temperature range. However, the tendency of reduction of the band gap with increasing temperature is suggested from the observation of the energy difference between the Dirac point and the bulk valence band. The result is consistent with the predictions by the theory [2] as well as the abovementioned expected band gap closing by the lattice expansion. Therefore, it is considered that a topological phase transition may occur at a temperature higher than 475 K. However, since the estimated band gap of 0.1 eV at the low temperature by the theory is underestimated compared with the one reported by previous ARPES measurement (~ 0.3 eV) [7], it is expected that the topological phase transition would occur at quite high temperature ~ 600 K if one assumes the constant band gap closing (~ 0.5 meV/K) which is observed in our measurement. These results suggest that the inclusion of the effect of lattice expansion is important in the understanding of the temperature-induced topological phase transition.

REFERENCES

- [1] G. Antonius and Steven G. Louie, *Phys. Rev. Lett.* 117, 246401(2016)
- [2] P. Dziawa, *Nature Materials* 11, 1023 (2012).
- [3] B. Monserrat and D. Vanderbilt, *Phys. Rev. Lett.* 117, 226801 (2016).
- [4] K. Saha and I. Garate, *Physical Review B* 89, 205103 (2014).
- [5] T.Sato et al., *Nature Physics* 7, 840 (2011)
- [6] Xu, S-Y. *Science* 332, 560–564 (2011)
- [7] K. Kuroda, M. Ye, et al. *Phys. Rev. Lett.* 105, 146801 (2010)

Performance evaluation of Graphene coated Co (0001) / W (110) as a target of spin-detector for out-of-plane spin component and the observation of its electronic structure

Y. Baba^a, T. Okuda^b and K. Miyamoto^b

^a Graduate School of Science, Hiroshima University, 1-3-1 Kagamiyama, Higashi-Hiroshima 739-8526, Japan

^b Hiroshima Synchrotron Radiation Center, Hiroshima University, 2-313 Kagamiyama, Higashi-Hiroshima 739-0046, Japan

Keywords: electron-spin detector, out-of-plane spin, graphene-coated Co

Various types of electron-spin detectors have been developed so far, and among them, a very low-electron diffraction (VLEED) spin detector based on the exchange scattering of electrons at a magnetized target (ferromagnetic target) shows the highest efficiency [1]. However, since the commonly used target can detect only in-plane spin components, one spin detector cannot resolve all spin components without complex system such as spin-rotator system. Therefore, a development of a target which can resolve out-of-plane spin component is demanded. It is well known that Co(0001) bulk single crystal possesses perpendicular magnetization[2], but the strong stray magnetic field can change the motion of electrons by Lorentz force and it is not useful for the spin detector. To suppress the stray magnetic field, Co film might be useful for a target of perpendicular spin detection. However, it is also required to keep the target performance for a long time for the reliable use of the target. Since the Co film can be easily contaminated by residual gas, some protection of the Co film is also necessary.

In this study, to overcome the problem, we have employed the graphene-coated Co (0001) film on W (110) [3] and examined the performance of the film as a target of spin detector for out-of-plane spin component by angle-resolved and spin-resolved photoemission spectroscopy.

Figure 1 shows the band dispersions of Graphene/40nm Co(0001)/W(110) near the $\bar{\Gamma}$, just after introduction from the atmosphere and after a short annealing (5-10 min.) at 600°C. It is found that the clean surface can be recovered by the annealing. We have also confirmed that the surface is not contaminated the sample surface by exposing it in the low vacuum chamber (about 3.6×10^5 [L]). On the other hand, according to the results from spin-resolved photoemission, it was found that this sample was not perpendicularly magnetized due to the influence of graphene or not thick enough. In this study, it was clarified that the surface of Co film is protected by graphene and that the surface is revived only by a short annealing.

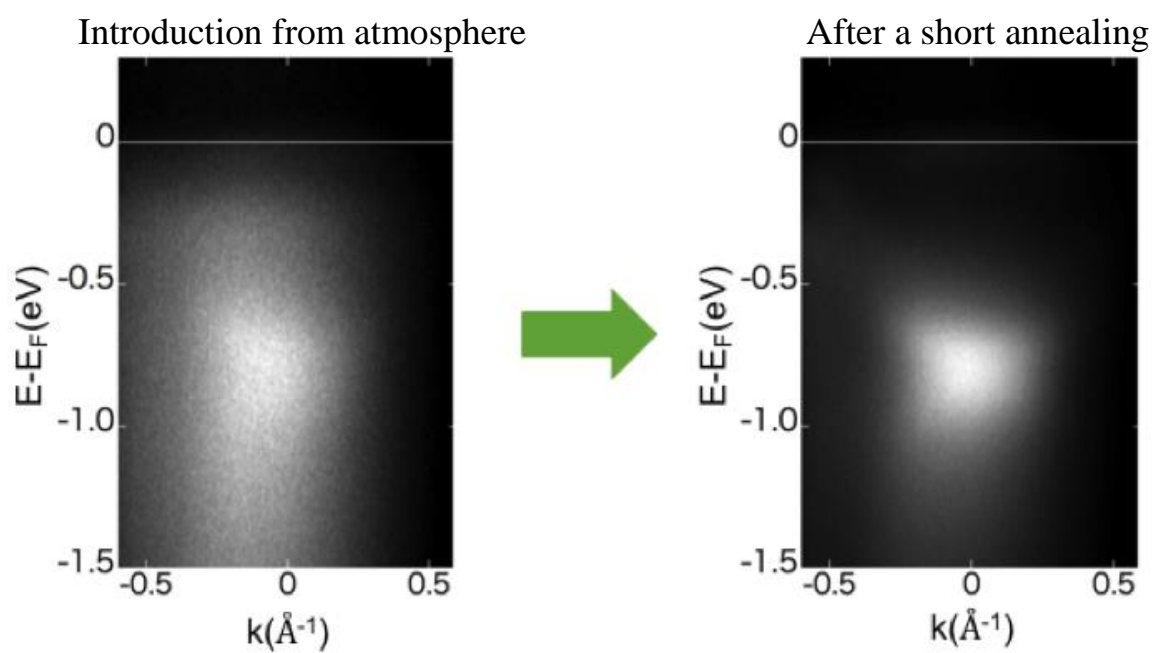


Fig.

1 Band dispersions of Grapnene-coating Co near $\bar{\Gamma}$ point after exposure of atmosphere and after

REFERENCES

1. T. Okuda, K. Miyamoto, A. Kimura, H. Namatame, M. Taniguchi, J. Electron Spectrosc. Relat. Phenom. 201, 23 (2015).
2. K. Honda and S. Kaya, Sci. Rep. Tohoku Univ. Bd.17, S. 1157 (1928).
3. D. Usachov and A. Fedorov, et al, Nano Lett. 15, 2396–2401 (2015).

Adsorption mechanism of hydrogen sulfide gas on granulated coal ash

Satoshi ASAOKA^a, Hiroyuki SAITO^b, Tsuyoshi ICHINARI^b,
Takahito OIKAWA^c and Shinjiro HAYAKAWA^d

^a Research Center for Inland Seas, Kobe University (5-1-1 Fukaeminami Higashinada Kobe 658-0022 Japan)

^b FujiClean Co., LTD. (33 Yamahana, Yamayashiki, Chiryu 472-0022 Japan)

^c The Chugoku Electric Power Co., INC. (3-9-1 Kagamiyama, Higashi-Hiroshima 739-0046 Japan)

^d Graduate School of Engineering, Hiroshima University (1-4-1 Kagamiyama, Higashi-Hiroshima 739-8527 Japan)

Keywords: domestic wastewater, hydrogen sulfide, wastewater treatment, XAFS

1. Introduction

Hydrogen sulfide is highly toxic to organisms and may cause foul odor. Granulated coal ash (GCA) is prepared by mixing fly ash from coal electric power plants with cement. We previously reported that GCA could adsorb and oxidize hydrogen sulfide in water. However, the adsorption of hydrogen sulfide in waste gases to GCA is not revealed yet. Removal of hydrogen sulfide from waste gases comprise physical and chemical processes. The purposes of this study is to reveal adsorption mechanisms of hydrogen sulfide gas to GCA.

2. Materials and Methods

Dried GCA which particle size is 3-5 mm in diameter was packed in a mini column (50 mm h, 30 mm in diameter). Thereafter, hydrogen sulfide gas (800-1600 ppmv) was introduced to the mini column at rate of 0.3 L min⁻¹. The concentration of hydrogen sulfide gas before and after the mini column was monitored by detection tubes. In addition to dried GCA, wet GCA was also prepared by immersing the GCA in water for 1 d. The adsorption test for hydrogen sulfide using the wet GCA was conducted with the same procedure. After adsorption of hydrogen sulfide to GCAs, the GCAs were stored in vacuum packs to prevent oxidation before XAFS analyses.

Sulfur K edge XAFS spectra (ranges 2460–2490 eV) of the sediments were measured using the BL11 in the Hiroshima Synchrotron Research Center, HiSOR. The synchrotron radiation from a bending magnet was monochromatized with a Si(111) double-crystal monochromator. The sample chamber was filled with He gas, and XAFS spectra were measured by the X-ray fluorescence yield (XFY) mode using a SDD detector (XR-100SDD; AMPTEK). The K edge main peak of sulfate derived from CuSO₄·5H₂O was set to 2481.6 eV. The GCA samples were mounted on a double stick tape (NW-K15; Nichiban) placed in the central hole (15 mm in diameter) of a copper plate.

3. Results and Discussion

Removal percentages of hydrogen sulfide by the dried GCA and the wet GCA were 99.5% and 25%, respectively. The maximum adsorption capacities for hydrogen sulfide were 320 g L⁻¹ for the dried GCA and 31 g L⁻¹ for the wet GCA. The adsorption of hydrogen sulfide to the wet GCA was much lower than that of the dried GCA.

The sulfur species on the surface of the GCAs identified by XAFS are shown in **Fig. 1**. The composition of sulfur species on the surface of the dried GCA was sulfate (93%) and elemental sulfur (7%). In contrast, sulfate accounted for 100% on the surface of wet GCA. Hence, hydrogen sulfide was oxidized to sulfate or sulfur on the surface of the GCAs.

REFERENCES

Patent Application 2020-010845 (27 January 2020): Deodorant

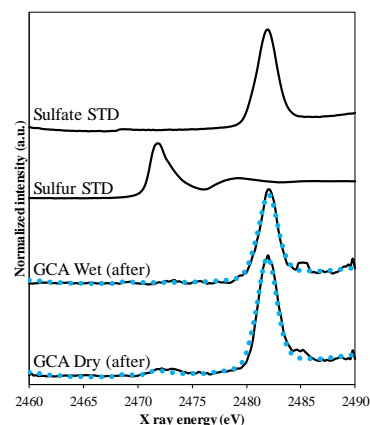


Fig. 1 Sulfur X edge spectra of hydrogen sulfide adsorbed GCAs. Dotted lines stand for the results of linear combination fit by using sulfur and sulfate standards.

Chemical composition of calcium species in fertilization pellets produced from anaerobic digestate

Satoshi ASAOKA^a, Gen YOSHIDA^b,

Ikko IHARA^b and Shinjiro HAYAKAWA^c

^a Research Center for Inland Seas, Kobe University (5-1-1 Fukaeminami Higashinada Kobe 658-0022 Japan)

^b Graduated school of Agricultural Science, Kobe University (1-1 Rokkodai, Nada, Kobe 657-8501, Japan)

^c Graduate School of Engineering, Hiroshima University (1-4-1 Kagamiyama, Higashi-Hiroshima 739-8527 Japan)

Keywords: calcium silicate, methane fermentation, nutrients, oligotrophication

1. Introduction

In the 1960-1970s, the Seto Inland Sea, Japan, experienced eutrophication due to increased discharge of nutrients accompanying drastic economic growth. Currently, nutrient concentration in the sea has decreased under laws concerning oceanic environmental conservation. As a result, fish catches have fallen sharply. Another environmental issue is the utilization of anaerobic digestate, which is a byproduct of methane fermentation. We must find an effective use for anaerobic digestate to promote biomass power generation. Given these problems, we have developed ocean fertilization pellets to promote primary production in oligotrophic seas by mixing the anaerobic digestate with high nutrients (nitrogen and phosphate) and blast furnace cement. The dissolution behavior of phosphate in the fertilization pellets might depend on calcium species in the fertilization pellets because the phosphate in the fertilization pellets is considered to form calcium phosphate. The purpose of this study is to identify calcium species in the fertilization pellets.

2. Materials and Methods

The fertilization pellets were prepared by mixing the anaerobic digestate and blast furnace cement at mixture weight ratios of 1:1 (pellet A); 2:1 (pellet B); and 4:1 (pellet C). Batch experiments were conducted to investigate the dissolution behavior of nutrients to artificial seawater.

Calcium K edge XAFS spectra (ranges 4045–4095 eV) of the sediments were measured using the BL11 in the Hiroshima Synchrotron Research Center, HiSOR [1]. The synchrotron radiation from a bending magnet was monochromatized with a Si(111) double-crystal monochromator. The sample chamber was filled with He gas, and XAFS spectra were measured by the X-ray fluorescence yield (XFY) mode using a SDD detector (XR-100SDD; AMPTEK). The X-ray energy around K edges of sulfur was calibrated with the spectra of CuSO₄ obtained with the CEY mode. The pellet samples were mounted on a double stick tape (NW-K15; Nichiban) placed in the central hole (15 mm in diameter) of a copper plate. The surface of the sample was attached to that of the copper plate. The angle between the incident X-ray and the sample surface was adjusted at 20°, and the X-ray fluorescence was detected from the direction normal to the incident beam in the plane of electron orbit of the storage ring.

3. Results and Discussion

Cumulative amounts of dissolved inorganic phosphorus (DIP) dissolved from the pellets were <0.005 mg g⁻¹ (pellet A), 0.074 mg g⁻¹ (Pellet B) and 0.48 mg g⁻¹ (pellet C) after 42 days. Calcium K edge XAFS spectra of the pellets and standards are shown in **Fig. 1**. Calcium phosphate was not identified in the pellets because calcium phosphate might not be major species and its concentration was less than

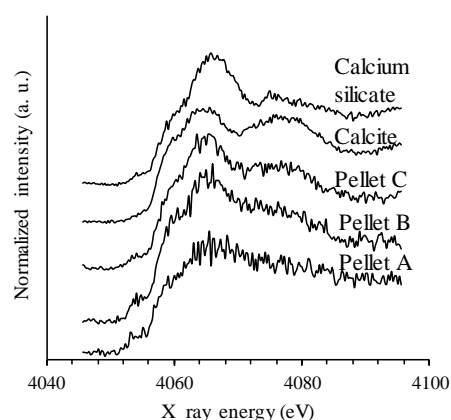


Fig. 1 Calcium K edge XAFS spectra of the fertilization pellets

0.04%. Calcium silicate like peak was observed with increasing mixing ratio of the anaerobic digestate. Because the digestate use in this study was originated from livestock waste, silicate from the livestock waste reacted with calcium from the cement and formed calcium silicate.

Acknowledgements

This study was partially supported by Hyogo Eco-town Promotion Conference.

REFERENCES

1. Asaoka, S., Umehara, A., Otani, S., Fujii, N., Okuda, T., Nakai, S., Nishijima, W., Takeuchi, K., Shibata, K. Jadoon, W.A., Hayakawa, S. *Mar. Pollut. Bull.* **133**, 891-899 (2018).

Sulfur K-edge XAFS structural analysis of the acid decomposition reaction of diethyldithiocarbamate

Atsuya Doi, Jens R. STELLHORN, Kenji Komaguchi, Shinjiro Hayakawa

Department of Applied Chemistry, Graduate school of Engineering, Hiroshima University, Higashi-Hiroshima, Hiroshima, 739-8527, Japan

[Introduction]

Sodium diethyldithiocarbamate (Na-DDTC) is one of famous chelating agents. Since its complex with a transition metal ion is hardly soluble in water, it is widely used for solvent extraction method. Considering that Na-DDTC is obtained from diethylamine and CS₂ in the presence of NaOH, DDTC can be decomposed in the reverse reaction under acidic conditions. We have investigated Sulfur K-edge XAFS spectra of DDTC under the acidic condition, and have found that the protonated DDTC has longer life than expected before the decomposition. Kinetics and structural information of DDTC will be discussed.

[Experimental]

Aqueous solutions of Na-DDTC were prepared with the buffer solutions to maintain pH of the solution constant, and spectral changes of a 196 μM aqueous Na-DDTC solution were measured with a spectrophotometer, Sulfur K-edge XAFS measurements were performed on a 50 mM aqueous Na-DDTC solution prepared with the same buffer solutions. The experiments were performed on BL11 of HiSOR. A sealed liquid cell was used for the measurement. With this cell, a liquid film of approximately 200 μm in thickness can be formed. XAFS spectra were obtained with the X-ray fluorescence yield (XFY) method in a He filled chamber.

[Results and discussion]

Figure 1 shows the temporal changes of UV spectra of 196 μM Na-DDTC solution at pH 7.33 (Tris-HCl buffer). Three characteristic absorption bands were observed in the UV spectra. Two peaks at 257 nm and 282 nm decayed while the other peak at 207 nm increased, and the isosbestic point appeared. The former two peaks are assigned to carbamate ion [1] and the latter peak is similar to that of CS₂. Considering that the solubility of CS₂ is extremely small in aqueous solution, the latter peak may be assigned to protonated DDTC, and the sum of DDTC and DDTC-H was conserved during the measurements at pH 7.33. Similar experiments were performed using an acetate buffer (pH 4.92) and a phosphate buffer (pH 6.86, 7.52, 7.57). From the changes in absorbance at wavelengths of 207 nm and 282 nm, rate constants of protonation and decomposition were determined.

Figure 2 shows the temporal changes in sulfur K-edge XAFS spectra of Na-DDTC solution at pH 7.33 (Tris-HCl buffer). The spectra were normalized for comparison, but the sulfur XFY was conserved during the measurements. For comparison, the spectra of DDTC at pH 13.52 (A) and CS₂ (B) are included in the figure. The spectrum A represents DDTC without protonation. The peaks at 2.4700 keV and 2.4715 keV are assigned to transitions from 1s to π* and σ*, respectively. It is clear that the XAFS spectra became similar to that of CS₂, and the spectrum obtained at 110 min was well expressed with the mixture of spectrum A (67%) and spectrum B (33%). Rate of the protonation reaction calculated from the UV measurements was about 7.5 % under the experimental condition, and the reason of the discrepancy between the calculated and

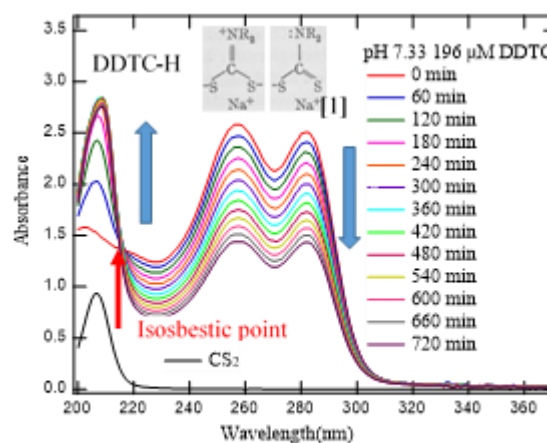


FIGURE 1. Temporal changes in UV spectra of 196 μM Na-DDTC at pH 7.33

experimental results was unclear.

Though the shape of the XAFS spectrum obtained at 110 min was well explained with the waveform synthesis, there was clear difference of the π^* peak position, and the peak position was 0.3 eV in lower than that of CS_2 . It may be caused by the structural difference between CS_2 and DDTC-H especially around the SCS bond angle.

Molecular orbital calculations for DDTC, DDTC-H, and CS_2 were performed using Gaussian 03W with 6-31G(d) basis set. The optimized structure of DDTC-H showed changes of N-C bond length from 1.328 Å to 1.514 Å, and the change of SCS angle from 120.4 deg to 127.9 deg. Calculated energies of both π^* and σ^* molecular orbitals of DDTC and DDTC-H increased slightly after the protonation. In the observed XAFS spectra π^* peak showed higher energy shift while the σ^* peak remained in the same position. The higher energy shift of the π^* peak may be caused by the structure change of DDTC-H.

It was clear that the observed spectra changes were much greater than that expected with the protonation, and the other possibility of formation of CS_2 should be considered.

Figure 3 shows the sulfur K-edge XAFS spectra of CS_2 and 4.70 vol% CS_2 in ethanol, and aqueous DDTC solution of pH 4.70. The spectra of CS_2 and CS_2 in ethanol were almost identical except for the sharper peak width of σ^* peak. The spectrum of the pH 4.70 DDTC was similar to that of the CS_2 -ethanol, and structures in higher energy region were different from other two spectra. The possibilities of aggregation of formed CS_2 and diethyl amine might be considered in the solution.

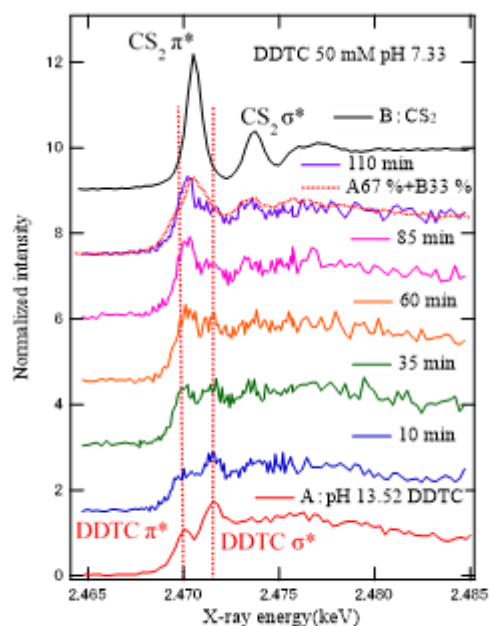


FIGURE 2. Temporal changes in sulfur K-edge XAFS spectra of 50 mM DDTC at pH 7.33

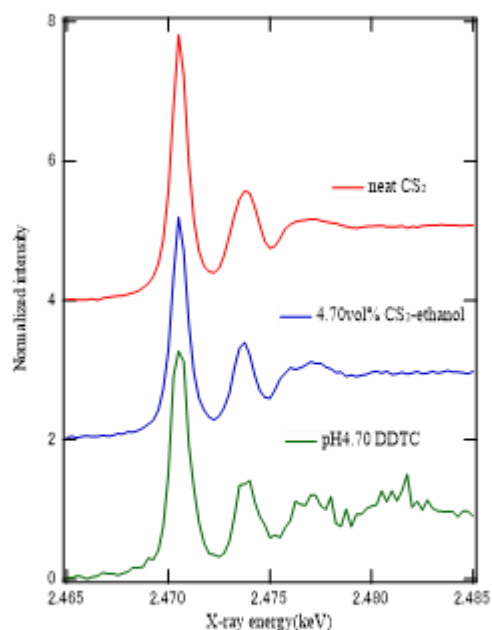


FIGURE 3. Sulfur K-edge XAFS spectra of CS_2 , CS_2 -ethanol and DDTC

REFERENCES

1. G.D.Thorn, R.A.Ludwig, The Dithiocarbamates and Related Compounds 1962

Identification of sulfur species in marine sediments collected from the western part of Seto Inland Sea, Japan

Satoshi ASAOKA^a, Shinjiro HAYAKAWA^b and Kazuhiko TAKEDA^c

^a *Research Center for Inland Seas, Kobe University (5-1-1 Fukaeminami Higashinada Kobe 658-0022 Japan)*

^b *Graduate School of Engineering, Hiroshima University (1-4-1 Kagamiyama, Higashi-Hiroshima 739-8527 Japan)*

^c *Graduate School of Integrated Sciences for Life, Hiroshima University (1-7-1 Kagamiyama, Higashi-Hiroshima 739-8521)*

Keywords: hydrogen sulfide, pyrite, sulfate, thiosulfate, XAFS

1. Introduction

Hydrogen sulfide in eutrophic marine sediments is highly toxic to benthic organisms and may cause foul odor and blue tide. The hydrogen sulfide distribution in marine sediments is controlled by biogenic and abiogenic reactions such as sulfide oxidation, sulfate reduction, metal sulfide precipitation and dissolution, nucleophilic additions to organic matter, and acid base equilibria. We previously reported that sulfur species in marine sediments collected from the central and eastern parts of Seto Inland Sea, Japan mainly fitted with the combination of sulfate, thiosulfate, elemental sulfur and pyrite. However, the sulfur species in marine sediments in the western part of the Sea is not revealed yet. The purposes of this study were to (1) determine directly the hydrogen sulfide concentration in marine sediment pore water using a detection tube and (2) identify sulfur species in marine sediment collected from the western part of Seto Inland Sea, Japan.

2. Materials and Methods

Sediment samples were collected from the western part of Seto Inland Sea, Japan (**Fig. 1**) using an undisturbed core sampler (ø11 cm, 50 cm long: HR type; Rigo) or a Smith-McIntyre Grab (33 cm x 33 cm; Rigo) deployed from a training and research vessel, TOYOSHIO-Maru, Faculty of Biological Science, Hiroshima University on July 8-11th in 2019. The collected sediment cores were cut at every 5 cm on board. The surface sediments collected by the Ekman-Birge bottom sampler were taken from the top layer (5 cm). The sediment pore water was collected by installing a soil moisture sampler (DIK-305A; Daiki Rika Kogyo) to the sediments and the concentration of hydrogen sulfide in the pore water was measured by the detection tube (200SA or 200SB; Komyo Rikagaku Kogyo). Oxidation and reduction potential (Eh) and pH were measured by inserting each electrode to the sediments (RM-30P; DKK-TOA, C-62; AS ONE). The collected sediments were vacuum-dried at 45°C and ground using an agate made mortar. The homogenized sediment samples were stored in vacuum packs to prevent oxidation before XAFS analyses.

Sulfur K edge XAFS spectra (ranges 2460–2490 eV) of the sediments were measured using the BL11 in the Hiroshima Synchrotron Research Center, HiSOR [1]. The synchrotron radiation from a bending magnet was monochromatized with a Si(111) double-crystal monochromator. The sample chamber was filled with He gas, and XAFS spectra were measured by the X-ray fluorescence yield (XFY) mode using a SDD detector (XR-100SDD; AMPTEK). The X-ray energy around K edges of sulfur was calibrated with the spectra of CuSO₄ obtained with the CEY mode. The K edge main peak of sulfate was set to 2481.6 eV. The sediment samples were mounted on a double stick tape (NW-K15; Nichiban) placed in the central hole (15 mm in diameter) of a copper plate. The surface of the sample was attached to that of the copper plate. The angle between the incident X-ray and the sample surface was adjusted at 20°, and the X-ray fluorescence was detected from the direction normal to the incident beam in the plane of electron orbit of the storage ring. Concentrations of each sulfur species were calculated from total sulfur concentration proportionally divided by each sulfur species composition.

3. Results and Discussion

Hydrogen sulfide in sediment pore water were only detected in the range from 0.3 to 0.4 mg-S L⁻¹ at 5-15 cm layer of St SN-2. At other sampling stations, hydrogen sulfide were below the detection limit (<0.1 mg-S L⁻¹).

The sulfur species in surface sediments (0-5 cm layer) collected from the western part of Seto Inland Sea are shown in **Fig. 1**. Pyrite was significantly identified at Beppu Bay (ST-BB1) and the western part of Suonada (ST-SN1). Beppu Bay are adjacent to big industrial complex and affected by terrigenous organic load from Beppu city. In the case of the western part of Suonada, the terrigenous loads from the Yamakuni River form halocline. The enhancing primary production due to terrigenous loads from the Yamakuni River increase organic sedimentation flux. Therefore, sediments from the two sampling stations are sometimes affected by hypoxia. Under such anoxic conditions, sulfate-reducing bacteria (SRB) utilize sulfate as a terminal electron acceptor for the degradation of organic matter and generates hydrogen sulfide. Hence, pyrite in these stations was considered to be derived from hydrogen sulfide and iron contained in the sediments.

In other sampling stations (ST-SN2, ST-SN3, ST-0), sulfate, thiosulfate and sulfur were dominant sulfur species in the sediments. In contrast, the percent composition of sulfur species could not be quantified at Iyo-nada (ST-IN2, IN3 and IN4) and Bungo channel (ST-BS1 and BS3) because excellent sulfur XANES spectra could not be obtained in these sampling stations due to low sulfur concentration. However, weak sulfate peak was observed. These sampling station are affected by the intrusion of open-ocean water derived from Kuroshio. Therefore, the sulfur species such as hydrogen sulfide and iron sulfide hardly form in the sediments because dissolved oxygen can be supplied with the intrusion of open-ocean water.

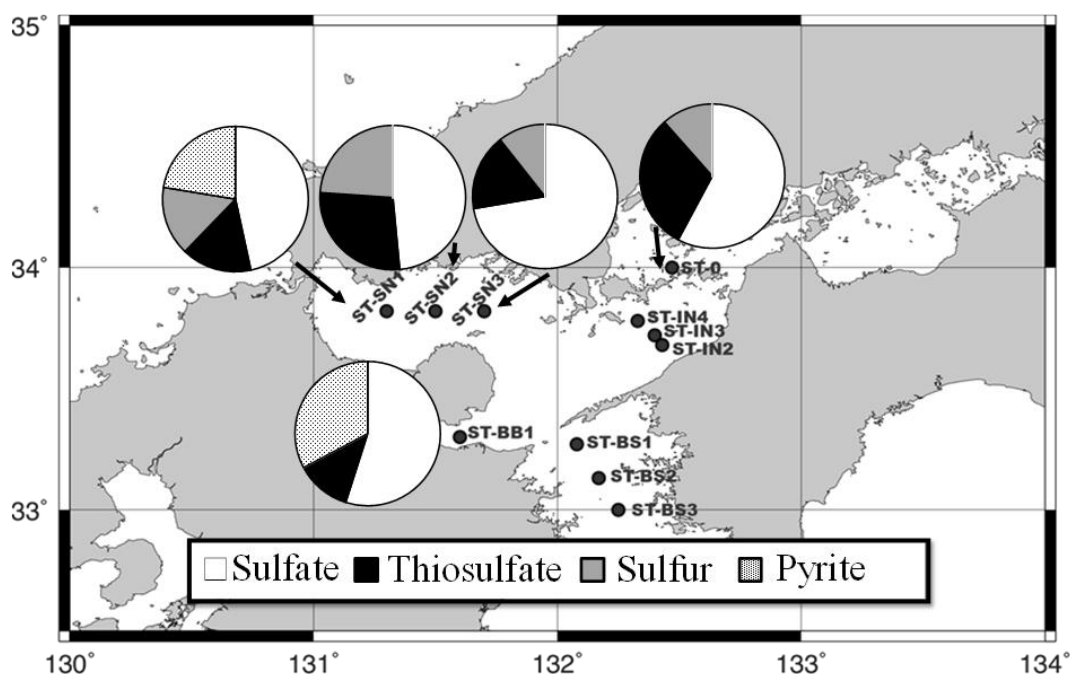


Fig. 1 Sulfur species composition in marine sediments collected from the western part of Seto Inland Sea, Japan

Acknowledgements

The authors show appreciation to Mr. Kazumitsu NAKAGUCHI, for piloting the research vessel.

REFERENCES

1. Asaoka, S., Umehara, A., Otani, S., Fujii, N., Okuda, T., Nakai, S., Nishijima, W., Takeuchi, K., Shibata, K. Jadoon, W.A., Hayakawa, S. *Mar. Pollut. Bull.* **133**, 891-899 (2018).

Transmission Curve Measurement of the Vacuum Window Installed in the X-ray Astronomy Satellite

T. Midooka^{a, b}, M. Tsujimoto^b, S. Kitamoto^c and S. Hayakawa^d

^aDepartment of Astronomy, The University of Tokyo, Tokyo, Japan

^bInstitute of Space and Astronautical Science (ISAS)/ Japan Aerospace Exploration Agency (JAXA), Kanagawa, Japan

^cDepartment of Physics, Rikkyo University, Tokyo, Japan

^dDepartment of Applied Chemistry, Hiroshima University, Hiroshima, Japan

Keywords: beryllium, X-ray transmission, astronomy satellite

The X-ray astronomy satellite XRISM is planned to be launched in 2022. It is expected to revolutionize the high-energy astrophysics with its high-resolution, high-throughput, and non-dispersive X-ray spectroscopic capability based on X-ray microcalorimetry. The instrument called "Resolve" is built on the heritage of Hitomi SXS, which demonstrated its capability in the orbit but was discontinued a month after the launch due to malfunction of the spacecraft attitude control system in 2016.

Resolve is a cryogenic instrument with the microcalorimeter detector in a cryostat. The gate valve with Be window of about 270 μm thickness is installed on top of the cryostat to keep the inside vacuum on the ground and to protect the cryostat interior from initial outgas contamination in the orbit. Until it will be opened a few months after the launch, all observations will be made through the gate valve. Therefore, knowledge of its X-ray transmission is crucial for the initial observational results.

We measured the X-ray transmission of the gate valve at KEK Photon Factory [1]. The X-ray transmission curve was obtained in the 2.0-12.0 keV range with a 2 eV pitch using a Si (111) double crystal monochromator (DCM). Fig 2 shows the transmission curve and its ratio to a model assuming photoelectric absorption by Be of a 250 μm thickness. In the lower panel of Fig 2, we found a transmission increase below 2.4 keV. This feature is likely caused by the effect of higher-order X-ray reflection in the DCM. We decided to make additional measurements to confirm this at HiSOR using BL11 for its capability in 2.0-3.0 keV and its availability in 2019 to be in time for the XRISM master schedule.



FIGURE 1. The Be window with an aluminium holder for safety

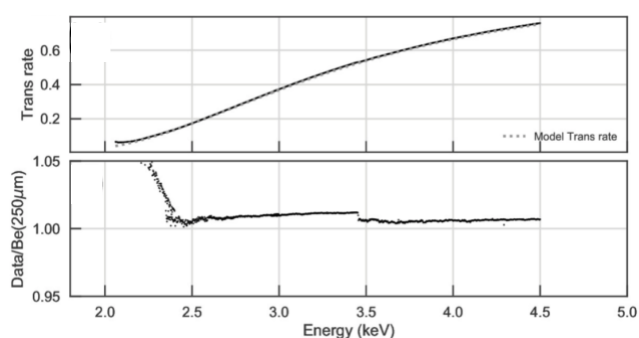


FIGURE 2. Upper: The measured transmission curve at KEK and a model curve assuming the Be thickness is 250 μm . Lower: The ratio of the measurement curve to the model curve.

First, We tilted the second crystal of the Si (111) DCM at HiSOR BL11 so that the incident light intensity decreases to about 80% of the intensity in the full-tuned (two crystal completely parallel) configuration. By measuring the X-ray transmission of the Be window in the detuned configuration, we can ignore the effects of higher-order X-rays because they have much narrower peak in the rocking curve. After the measurements in 2.1-4.0 keV, we returned the DCM to the full-tuned configuration and measured the transmission in 2.1-2.3 keV.

Fig 3 shows the results comparing between the full-tuning and detuning configuration. Below 2.3 keV, we found the measured transmission was lower than the model for both full-tuning and detuning. We made additional measurements at a fixed energy of 2140 eV for 2500 seconds and at 2400 eV for 890 seconds. The result is shown in Fig 4. We found that the derived X-ray transmission at 2400 eV (in orange) was stable within 1%, while that at 2140 eV (in blue) fluctuated by 30% for 40 minutes. We concluded that the X-ray transmission at the lower energy has a large uncertainty due to this time-varying factor.

One of the causes of this feature is the effect of residual air in the chamber, in which He gas is filled. We calculated the atmosphere transmission with a composition of 78.0% Nitrogen, 21.0% Oxygen, and 0.9% Argon, and found that the steep energy dependence in Fig 3 cannot be explained by the residual air alone. There should be other factors in the setup that made the observed decrease of the X-ray transmission below 2.3 keV, which remains unknown.

Assuming that the unknown factor is the same, we compare the transmission curves for the detuned and full-tuned configurations in 2.15–2.3 keV. In the lower energy band (2.10–2.15 keV), the transmission curve in the detuned configuration decreases exponentially as the energy decreases. On the other hand, the transmission curves in the full-tuned configuration decrease less sharply than that (Fig 3). We speculate that the higher-order X-rays contaminate the transmission measurements in the full-tuned configuration, as we anticipated.

In conclusion, the present result at HiSOR infers that the anomalous transmission increase measured at KEK (Fig 2) was also contaminated by high-order X-ray reflection at the DCM. However, the unknown time-varying factor found in the 2.1-2.3 keV band needs to be identified to establish this interpretation.

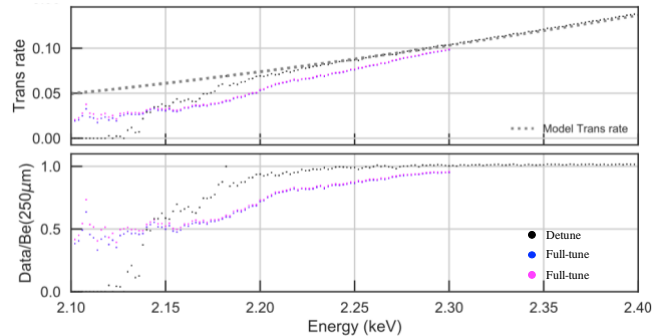


FIGURE 3. Upper: The measured transmission curves at HiSOR BL11 with detuning and full-tuning, and a model curve assuming the Be thickness is 250 μm . Lower: The ratio of the measurement curves to the model curve.

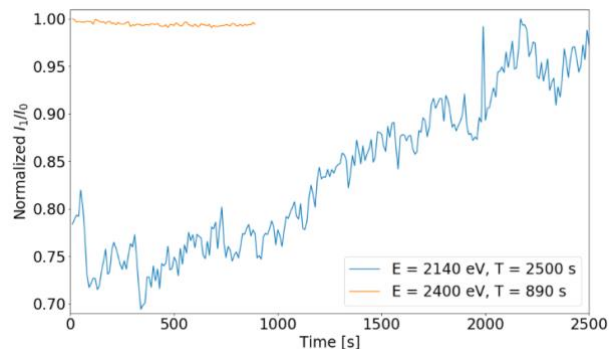


FIGURE 4. Fixed-energy measurement results using X-rays at 2140 eV and 2400 eV. The horizontal axis shows time, and the vertical axis shows the normalized X-ray intensity ratio between transmitted X-rays and incident X-rays.

REFERENCES

1. Midooka, T., 2020, “Ground calibration of XRISM for the initial observations -- X-ray transmission of the gate valve of the cryostat for the low-temperature detector.” Master thesis, The university of Tokyo

Structure of a Novel Amorphous Organic-Inorganic Hybrid Tin Cluster Exhibiting Nonlinear Optical Effects by Low-Energy XAFS Measurements

Jens R. Stellhorn^a, Shinjiro Hayakawa^a, Benedict Paulus^b, Benjamin D. Klee^b

^a Department of Applied Chemistry, Graduate School of Engineering, Hiroshima University, Higashi-Hiroshima, Hiroshima 739-8527, Japan

^b Department of Chemistry, Philipps University of Marburg, Marburg 35032, Germany

Keywords: Amorphous structure, low-energy XAFS, non-linear optical effect

Tailored light sources have greatly advanced technological and scientific progress by optimizing colour and brilliance, improving energy efficiencies or the quantum properties of light. So called supercontinuum generators are premier examples for media with nonlinear optical (NLO) effects – far superior in some respects to other sources such as phosphorescent white light-emitting diodes (LEDs). However, unlike LEDs, most of these advanced light sources are only used for scientific purposes, as they require extreme electric field strengths which are commonly realized by high-power pulsed lasers. In contrast, the materials of interest for this research project represent a new generation of supercontinuum emitters that are readily obtained from ubiquitous resources in a simple synthesis.

These compounds are of the general composition $\text{Sn}_4\text{S}_6\text{R}_4$ (R=Methyl, Phenyl, Naphtyl, Cyclopentadienyl) and exhibit strong NLO effects, making it possible to use them as cheap and efficient warm-white supercontinuum emitters when driven by a commercially available low-power continuous-wave infrared laser diode [1]. Quantum chemical calculations suggest that these compounds consist of Sn_4S_6 clusters. On the other hand, it was also confirmed that the NLO effect is linked to the amorphous nature of the materials, but the structural properties of the amorphous phase, and thereby the apparent origin of this effect, is difficult to determine [2].

To support the structural analysis, we performed low-energy x-ray absorption fine structure measurements at the sulfur *K* absorption edge (Fig. 1). This information will help to elucidate the local environment of S in the cluster. Furthermore, we will be able to determine if there are different S species, as can be expected when fragments of the cluster form a significant part of the sample structure. Already we established a shift of the absorption edge for R= Cyclopentadienyl (Cp), which exhibits the lowest NLO effects of the four different samples.

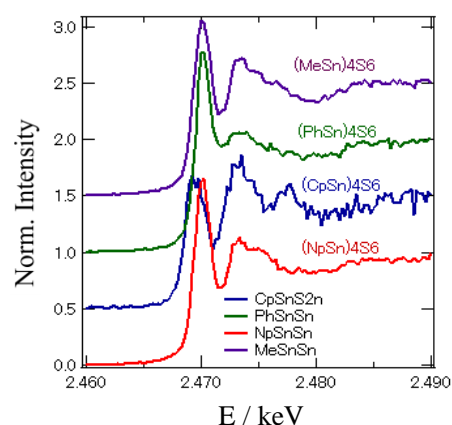


FIGURE 1. S *K*-edge XAFS spectra for four different $\text{Sn}_4\text{S}_6\text{R}_4$ compounds.

REFERENCES

- [1] N.W. Rosemann et al., Science 6291, 1301 (2016).
- [2] B. D. Klee, E. Dornsiepen, J. R. Stellhorn, Phys. Stat. Solidi B 255, 1800083 (2018).

Interaction Mechanism between α_1 -Acid Glycoprotein and Bio-Membrane Characterized by Vacuum-Ultraviolet Circular-Dichroism Spectroscopy

Koichi Matsuo^a, Munehiro Kumashiro^b, and Kunihiko Gekko^a

^aHiroshima Synchrotron Radiation Center, Hiroshima University,
2-313 Kagamiyama, Higashi-Hiroshima 739-0046, Japan

^bDepartment of Physical Science, Graduate School of Science, Hiroshima University,
1-3-1 Kagamiyama, Higashi-Hiroshima, Hiroshima 739-8526, Japan

Keywords: α_1 -acid glycoprotein; electrostatic and hydrophobic interactions; membrane-bound conformation; secondary structure of protein; synchrotron radiation circular dichroism.

How water-soluble globular proteins interact with bio-membranes is of great interest since such interactions occur in various biological events.¹ It is known that α_1 -acid glycoprotein (AGP) exhibits some characteristic binding abilities to numerous basic, acidic, and neutral drugs, and the binding capacity for neutral drugs decreases upon interacting with bio-membranes, dramatically changing its conformation.² Knowledge of the conformations of AGP on the membrane is indispensable for understanding its interaction mechanisms and membrane-mediated biological functions. This study characterized the mechanism of interaction between AGP and lipid membranes by measuring the vacuum-ultraviolet circular-dichroism (VUVCD) spectra of AGP down to 170 nm using synchrotron radiation in the presence of five types of liposomes whose constituent phospholipid molecules have different molecular characteristics in the head groups (e.g., different net charges).

AGP exhibited the characteristic VUVCD spectra when bound to membrane depending on the types of liposome (Fig.1). The secondary-structure analyses using SELCON3 program and VUVCD-NN method³ showed that the contents and segment numbers of helical structure of AGP largely increase upon interacting with the negatively-charged liposomes and that both neutral and positively-charged helix regions also take part in the AGP-membrane interaction. The neutral helix region was amphiphilic and its interaction was retained even in NaCl solution but the positively-charged helix region around W160 largely collapsed in NaCl solution. This collapse was also confirmed from the change of fluorescence spectra. These results indicate that the neutral helix of AGP would strongly interact with membrane by the hydrophobic interaction and the positively-charged helix would weakly interact with membrane by the electrostatic interaction, suggesting a delicate balance between electrostatic and hydrophobic interactions in AGP-membrane interaction. This demonstrates that the liposome-dependent conformations of AGP analyzed using VUVCD spectroscopy provide useful information for characterizing the mechanism of interaction between AGP and lipid membranes.

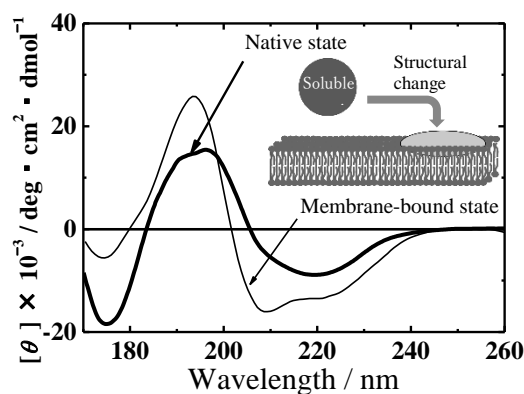


Fig 1. VUVCD spectra of AGP at native and membrane-bound states

1. Matsuo, K.; Namatame, H.; Taniguchi, M.; Gekko, K. *Proteins* **2016**, *84*, 349.
2. Matsuo, K.; Gekko, K. *Glycobiophysics* **2018**, *1104*, 101.
3. Matsuo, K.; Gekko, K. *Methods Mol. Biol.* **2013**, *974*, 151.

Electrostatic Interaction between An N-terminal Fragment of Myelin Basic Protein and A Phosphatidylinositol Membrane Characterized by Synchrotron Radiation Circular Dichroism Spectroscopy

Munehiro Kumashiro^a, Yudai Izumi^b, and Koichi Matsuo^b

^aDepartment of Physical Science, Graduated School of Science, Hiroshima University, 1-3-1 Kagamiyama, Higashi-Hiroshima, Hiroshima 739-8526, Japan

^bHiroshima Synchrotron Radiation Center, Hiroshima University, 2-313 Kagamiyama, Higashi-Hiroshima, Hiroshima 730-0046, Japan

Keywords: synchrotron radiation circular dichroism; peptide-membrane interaction; myelin basic protein.

The 18.5 kDa isoform of myelin basic protein (MBP) is an essential component for the formation of compact multilamellar myelin sheath in the central nervous system [1]. It is known that the MBP has three membrane-binding helical segments, which are located at T33–D46, V83–T92, and Y142–L154 residues and these three interactions could contribute to the stabilization of the myelin structure [1, 2]. However, the whole interaction mechanism between MBPs and membranes remains unclear because the conformation of membrane-bound MBP is unresolved. Here, we demonstrate that an N-terminal region of MBP (³QKRPSQESKYLASASTMDHARHGFL²⁷) interacts with the phosphatidylinositol (PI) membrane, and forms helical structure by using synchrotron radiation circular dichroism (SRCD) spectroscopy and molecular dynamics (MD) simulation.

The N-terminal fragment of MBP was synthesized using a solid-phase synthesis by Genscript biotech Corp. (NJ, USA). PI was purchased from Avanti Polar Lipids, Inc. (AL, USA). We used the Avanti Mini-Extruder (Avanti Polar Lipids, Inc., AL, USA) and prepared PI-liposomes by an extrusion technique. The peptide fragments were dissolved in 20 mM sodium acetate buffer (pH 4.5) and mixed with the liposome suspension at final concentrations of 30 μ M peptides and 0–4 mM liposomes. The SRCD spectra of the peptide fragments in the presence or absence of PI-liposomes were measured from 190 to 260 nm using the VUVCD spectrophotometer constructed at BL-12 of HiSOR [3]. The path length of the sample-cell was 1 mm. The MD simulations of the peptide fragment and the PI-membrane were carried out using GROMACS (Groningen Machine for Chemical Simulation) package and the CHARMM36m force field [4, 5]. The

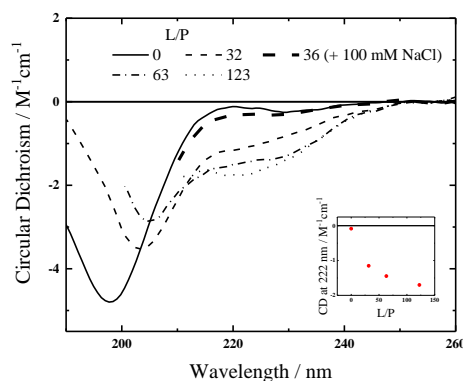


FIGURE 1. SRCD spectra of the N-terminal fragments of MBP (³QKRPSQESKYLASASTMDHARHGFL²⁷) in the presence or absence of the PI-liposomes at lipid to peptide molar ratio (L/P ratio) of 0, 32, 63, and 123 (solid, dashed, dash-dotted, and dotted lines, respectively). The inset shows the plots of CD intensities at 222 nm of the fragments against the L/P ratio. The SRCD spectrum of the fragments in the presence of PI-liposomes (L/P = 36) and 100 mM NaCl (thick dashed line) is also shown.

structural stability of the peptide fragment and the interaction between the peptide and the PI-membrane were evaluated with two different types of simulations: (1) the peptide fragment with random coil conformation was set at least 20 Å above the PI-membrane surface; (2) the peptide fragment with helical structure was set on the PI-membrane surface. These systems were used as the initial structures and simulated for 200 ns.

Figure 1 shows the SRCD spectra of the N-terminal fragments of MBP in the absence (native state) and the presence of the PI-liposomes. The inset of the figure 1 shows the plots of the CD intensities at 222 nm against the lipid-to-peptide molar ratio (L/P ratio). The peptide fragments in the native state exhibited a large negative CD peak around 200 nm, which is a characteristic peak of unordered structures. On the other hand, the spectra of the peptide fragments with the PI-liposomes showed a peak shift toward longer wavelength region and an increment of the CD intensities at 222 nm as L/P ratio increased. Since the helix structures of peptides and proteins exhibit the negative CD peaks around 222 nm [6], the increment of the CD intensity as shown in the inset of Figure 1 indicates that the helical structures of the peptide fragments increased via the interactions with liposomes. Further, the peptide fragments in the presence of deoxyphosphatidylcholine (L/P=490) or 47 % trifluoroethanol showed two negative peaks around 208 and 222 nm and a positive peak around 190 nm, suggesting that the peptide fragments formed helical structures in membrane-mimetic conditions (data not shown). The MD simulations of the peptide fragment and PI-membrane showed that the peptide fragment bound to the PI-membrane surface within 50 ns and that the helical conformation of the peptide fragment was formed within 200 ns. Furthermore, the MD simulations also showed that the peptide-membrane interaction was primarily electrostatic. As shown in Figure 1, it was also experimentally confirmed by the SRCD measurement, which showed that the interaction of the peptide fragment with PI-liposomes was canceled by 100 mM NaCl. It is known that MBP can bind to the membrane surface through the electrostatic interaction and that PIs are involved in MBP-membrane interactions [7]. Therefore, these results suggested that the N-terminal region of MBP is one of the candidate sites to electrostatically interact with PI-membrane. This electrostatic interaction and the PI-induced conformational change shown in the present work would contribute to reveal the whole interaction mechanism between MBPs and membranes.

REFERENCES

1. K. A. Vassall, V. V. Bamm, and G. Harauz, *Biochem. J.* **472**, 17-32 (2015).
2. G. Harauz, V. Ladizhansky, and J. M. Boggs, *Biochem.* **48**, 8094-8104 (2009).
3. N. Ojima, K. Sakai, K. Matsuo, T. Matsui, T. Fukazawa, H. Namatame, M. Taniguchi, and K. Gekko, *Chem. Lett.* **30**, 223-236 (2004).
4. M. J. Abraham, T. Murtola, R. Schulz, S. Pall, J. C. Smith, B. Hess, and E. Lindahl, *SoftwareX* **1-2**, 19-25 (2015).
5. J. Huang, S. Rauscher, G. Nawrocki, T. Ran, M. Fei, B. L. de Groot, H. Grubmuller, and A. D. MacKerell Jr, *Nature Methods* **14**, 71-73 (2017).
6. N. Greenfield and G. D. Fasman, *Biochem.* **8**, 4108-4116 (1969).
7. A. Raasakka, N. C. Jones, S. V. Hoffmann, and P. Kursula, *Biochem. Biophys. Res. Comm.* **511**, 7-12 (2019).

Optical Activity Measurement of Amino Acid Films by Circular Dichroism Spectroscopy

Jun-ichi Takahashi^a, Toshiki Sakamoto^a, Yudai Izumi^b, Koichi Matsuo^b
Masaki Fujimoto^c, Masahiro Katoh^{b, c}, Yoko Kebukawa^a, Kensei Kobayashi^a

^a*Faculty of Engineering, Yokohama National University, 79-5 Tokiwadai, Hodogaya-ku, Yokohama 240-8501, Japan*

^b*Hiroshima Synchrotron Radiation Center, Hiroshima University, 2-313 Kagamiyama, Higashi-Hiroshima 739-0046, Japan*

^c*UVSOR Facility, Institute for Molecular Science, 38 Nishigo-Naka, Myodaiji, Okazaki 444-8585, Japan*

Keywords: Homochirality, Amino Acid, Optical Activity, Circularly Polarized Light, Circular Dichroism

The origin of homochirality in terrestrial biomolecules (L-amino acid and D-sugar dominant) remains one of the most mysterious problems in the research for the origins of life. Rational explanations for the chiral asymmetry introduction into biomolecules are required through interdisciplinary collaborations. One of the most attractive hypotheses in the context of astrobiology is “Cosmic Scenario” as below [1,2];

(1) Asymmetric reactions of prebiotic molecules on interstellar dust surfaces in molecular cloud circumstances were introduced by asymmetric radiation sources in space, that is “chiral radiations”.

(2) The chiral products were transformed into the complex organic materials including amino-acid precursors as “chiral seeds”.

(3) The complex organic materials as “chiral seeds” were transported with meteorites or asteroids to primitive Earth resulting in terrestrial biomolecular homochirality.

Several ground experiments to validate the scenario have been investigated asymmetric photochemical reactions in simple biochemical molecules using circularly polarized light (CPL) from high-energy particle accelerators. We have already reported optical activity emergence in solid-phase films of racemic amino acids by left- or right-handed CPL (L- or R-CPL) irradiation of 215 nm in wavelength from free electron laser (FEL) of UVSOR-II [3]. By analysis using conventional circular dichroism (CD) spectrometer, preferential structural changes between the two enantiomers in racemic mixtures of amino acids have been introduced by L- or R-CPL irradiation from FEL.

CD spectroscopy can detect optical activity emergence with a high accuracy because CD spectra sensitively reflects the steric structures of chiral molecules. The theoretical calculation of CD spectrum of L-alanine molecule has revealed that the chromophores such as carboxyl and amino groups are derived from characteristic electronic transitions ($n-\pi^*$, $\pi-\pi^*$, and $n-\sigma^*$) corresponding to different wavelengths below 230 nm [4,5]. It is strongly suggested that optical activity emergence by asymmetric photochemical reactions depends on the photon energy.

In present, we are carrying out irradiation experiments by using CPL with different wavelengths to investigate the photon energy dependence of photochemical chiral reactions. As for the sample, we formed thin solid films of racemic mixture of alanine on quartz substrates from crystal powders of DL-alanine (L/D = 50/50) as a sublimation source by using a thermal-crucible vacuum-evaporation system in HiSOR. Sublimation temperature was controlled in the range of 150~200°C and pressure of the vacuum chamber was approximately 5×10^{-2} Pa throughout the evaporation process. The CD spectra of thin solid films just after the deposition were measured from 260 to 160 nm in wavelength using a vacuum-ultraviolet (VUV) CD instrument at beam line BL-12 of HiSOR and confirmed to be mostly zero CD before the irradiation, showing that the spurious CD due to the contamination of film surface were negligible.

The thin solid films of racemic mixture of alanine were irradiated of L- or R-CPL in different wavelengths using the undulator beam line BL1U of UVSOR-III [6]. In case of CPL irradiation in shorter wavelengths than 200 nm, the samples were set in a vacuum sample chamber preventing attenuation by air absorption. On the beam

entrance side of the vacuum sample chamber, a gate valve with an MgF₂ vacuum sealing window was mounted. The irradiated CPL wavelengths were 180 and 155 nm corresponding to photon absorption bands of alanine molecule. The irradiated photon energy dose was measured with photoelectron current of a silicon photodiode (International Radiation Detectors, Inc.) settled at the sample position [7,8].

CD spectra of the CPL irradiated films were measured at beam line BL-12 of HiSOR to clarify the optical activity emergence by CPL irradiation. In order to delete the effects of linear dichroism (LD) and/or linear birefringence (LB) components, dependence on sample rotation angle (0, 45, 90, and 135 degrees) of the CD spectra was measured. The observed spectral profile strongly depends on the irradiated CPL wavelength and the polarization (L- or R-CPL) [9,10]. In Figure 1, CD spectra of DL-alanine films irradiated by L- or R-CPL at 180 and 155 nm in wavelength are shown. We are now planning the irradiation experiment using CPL at 120 nm in wavelength, which is corresponding to hydrogen Lyman alpha line.

Detailed analysis of CD spectra is in progress to clarify full mechanism of the optical activity emergence, which potentially has relevance to the origin of terrestrial bioorganic homochirality stimulated by “chiral radiation”.

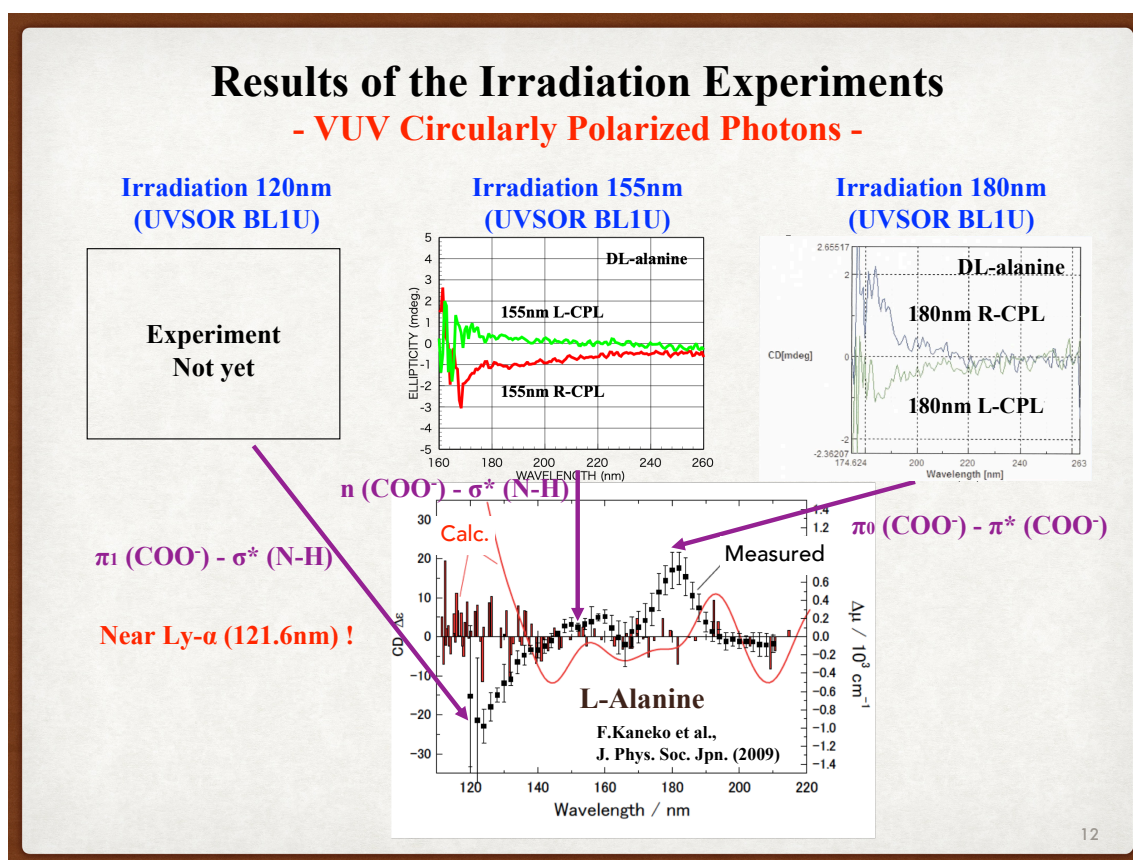


FIGURE 1. CD spectra of the L- or R-CPL irradiated DL-alanine film measured at BL-12 of HiSOR. The CPL irradiation wavelengths were 180 nm and 155 nm at BL1U of UVSOR-III.

REFERENCES

1. W. A. Bonner, *Orig. Life Evol. Biosph.* **21**, 407 (1991).
2. J. Takahashi et al., *Symmetry.* **11**, 919 (2019).
3. J. Takahashi et al., *Int. J. Mol. Sci.* **10**, 3044 (2009).
4. T. Fukuyama et al., *J Phys. Chem.* **A109**, 6928 (2005).
5. F. Kaneko et al., *J. Phys. Soc. Jpn.* **78** 013001 (2009).
6. K. Matsuo et al., *UVSOR Activity Report 2016* **44**, 157 (2017).
7. J. Takahashi et al., *HiSOR Activity Report 2017* 126 (2018).
8. J. Takahashi et al., *UVSOR Activity Report 2017* **45**, 145 (2018).
9. J. Takahashi et al., *UVSOR Activity Report 2018* **46**, 156 (2019).
10. J. Takahashi et al., *Proceedings of The 23rd Hiroshima International Symposium on Synchrotron Radiation* p.55 (2019).

Structure analysis of dimer and multimer of DNA repair protein, XRCC4, using VUV-CD

Kai Nishikubo^{a,b}, Maho Hasegawa^{a,b}, Yudai Izumi^c, Kentaro Fujii^b,
Koichi Matsuo^c, Yoshihisa Matsumoto^d, Akinari Yokoya^{b,a}

^a*Graduate School of Science and Engineering, Ibaraki University, Japan*

^b*Quantum Beam Science Research Directorate, National Institutes for Quantum and Radiological Science and Technology (QST), Japan*

^c*Hiroshima Synchrotron Radiation Center, Hiroshima University, Japan*

^d*Tokyo Institute of Technology*

Keywords: VUV-CD, XRCC4, DNA repair, phosphorylation

XRCC4 is a key protein to repair severe DNA damage of double strand breaks (1). It has been reported that a dimer of XRCC4 forms a substructure with another repair protein, XRCC4-like factor (XLF). Enzymatically induced phosphorylation at several amino acid residues in XRCC4, such as serine (2), might cause a local change of statically electric charge, resulting conformational alteration to activate the protein. However, the correlation between the structural change and activation has not been understood yet. Full-length XRCC4 was not able to be crystallize because of its intrinsically disordered C-terminal region including several phosphorylation sites. Thus, we have applied circular dichroism (CD) spectral analysis for the full length of wild type XRCC4 (denoted as WT) in an aqueous solution and reported its characteristic secondary structure (3).

To investigate further the structural change by phosphorylation, in this study, we prepared a mutated XRCC4 in which a serine residue was substituted to an aspartic acid (denoted as S327D) to mimic phosphorylation in terms of statically electric charge. The protein solution obtained from *E. coli* cell extracts was a mixture of dimers and multimers, thus those fractions were separated by a gel filtration method before CD measurements. The obtained CD spectra were compared with that of WT. Although spectra for both dimer proteins of WT and S327D were similar, the latter showed slightly different spectrum from that of WT when they formed a multimer (**FIGURE 1**). The composition ratios of the secondary structures for both WT and S327D were calculated using a software, SELCON3. The content of β -strand of S327D was significantly higher than that of WT, and conversely, the content of both α -helix and random of S327D was lower than that of WT (**TABLE 1**). The results indicate that

β -strand content would be greatly increased by phosphorylation when the proteins form a multimer. It is inferred that the C-terminal phosphorylation facilitates polymerization of the proteins surrounding DNA terminus at the double strand break site, presumably through forming a fiber-like architecture composed of each dimer and/or XLF connected at the newly formed β -structures in its not only original α -helix region but also intrinsically disordered region.

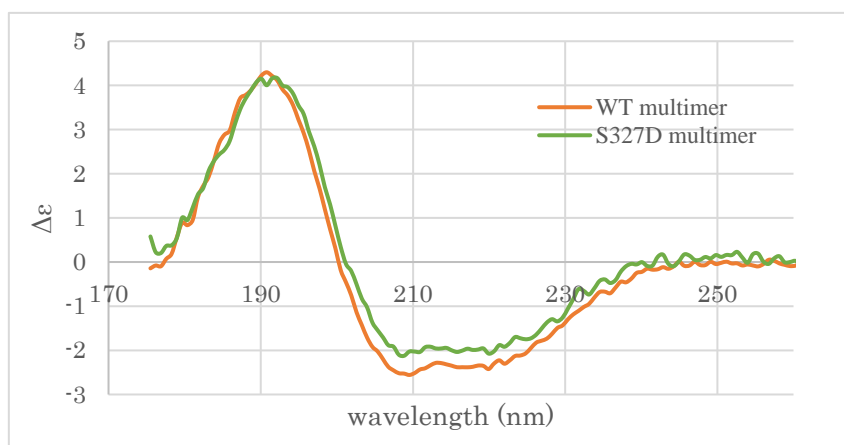


FIGURE 1. VUV-CD spectra of full-length of XRCC4 multimers. The orange and green lines indicate WT and S327D, respectively.

TABLE1. Contents of secondary structures of dimer of WT and multimers of WT and S327D of XRCC4.

| Secondary structure | WT dimer | WT multimer | S327D multimer |
|---------------------|----------|-------------|----------------|
| α -helix (%) | 46.1 | 30.8 | 24.1 |
| β -strand (%) | 9.0 | 17.9 | 31.5 |
| turn (%) | 22.6 | 22.2 | 24.4 |
| random (%) | 23.0 | 25.6 | 19.5 |

REFERENCES

1. R. P. Kamdar and Y. Matsumoto, Radiation-induced XRCC4 Association with Chromatin DNA Analyzed by Biochemical Fractionation. *J. Radiat. Res.* **51**, 303-313 (2010).
2. M. Hammel, M. Rey, Y. Yu, R. C. Mani, S. Classen, M. Liu, M. E. Pique, S. Fang, B. L. Mahaney, M. Weinfeld, D. C. Schriemer, S. P. Lees-Miller and J. A. Tainer, XRCC4 protein interactions with XRCC4-like factor (XLF) create an extended grooved scaffold for DNA ligation and double strand break repair. *J. Biol. Chem.* **286**, 32638-32650 (2011).
3. K. Nishikubo, Y. Izumi, Y. Matsumoto, K. Fujii, K. Matsuo and A. Yokoya, Structural analysis of DNA repair protein XRCC4 applying circular dichroism in an aqueous solution. *Radiat. Prot. Dosim.* **183**, 36-39 (2019).

Determination of the Degree of Linear Polarization in BL-13 by Using a Planarly-Oriented Material

Masataka Tabuse^a, Kamon Yamamoto^a, and Shin-ichi Wada^{a,b}

^a*Department of Physical Science, Hiroshima University*

^b*Hiroshima Synchrotron Radiation Center, Hiroshima University*

Keywords: Linear Polarization, HOPG (highly oriented pyrolytic graphite), XAS (X-ray absorption spectroscopy), NEXAFS (near edge X-ray absorption fine structure).

X-ray absorption spectroscopy (XAS) is one of powerful tools to investigate local structural and dynamical information because of its element selectivity. Especially, one can easily get orientation structure around X-ray absorption center by using linearly polarized X-ray beam. Most simple method to determine the degree of linear polarization is by using a multilayer optical component, but such an optical component for X-ray regime is expensive and is not easy to use routinely. Another technique is polarization dependent XAS measurement of structurally well-known anisotropic materials. So far, measurements of near-edge X-ray absorption fine structure (NEXAFS) for CO monolayer on a Ni(100) surface [1] and Langmuir-Blodgett monolayers of Ca- and Cd-arachidate molecules [2] have been reported, which have still disadvantage of difficulty in sample preparation in vacuum and perfect ordering of molecules. Recently, Watts and co-workers have proposed the alternative approach by using planarly-oriented carbon material, highly ordered pyrolytic graphite (HOPG), without additional experimental apparatus [3]. In this study, this technique was applied to HiSOR BL-13 and the degree of linear polarization was determined.

BL-13 is a soft X-ray beamline in HiSOR with a Dragon-type spherical grating monochromator [4]. The beamline has been developed to investigate soft X-ray surface photochemistry and has kept a potential to measure X-ray absorption and photoelectron spectra especially for organic materials. XAS as well as X-ray photoelectron spectroscopy (XPS) is a great tool to investigate element-specific electronic states of samples. So far, XAS measurements at the end station of BL-13 has been provided with the total electron yield (TEY) and total ion yield (TIY) modes. Quite recently, a newly built partial yield detector was installed in order to measure XAS with partial electron yield (PEY) and total fluorescence yield (TFY) modes.

Measurements of C K-edge NEXAFS spectra were performed for HOPG mounted on a sample manipulator with a tilt angle. Fig. 1(a) shows a schematic drawing of the HOPG sample with a fixed tilt angle θ_c to a sample manipulator installed at the BL-13 end station. Normally, polarization-dependent NEXAFS measurements are performed by changing a polar angle, α . But in this experiment, X-ray was irradiated to the sample only at the normal incidence angle ($\alpha=0$). Alternatively, the azimuthal angle, ϕ , of the mounted sample was changed to measure the degree of linear polarization. Fig. 1(b) shows a snapshot of actual HOPG sample mounted with a home-made tilted stage on the manipulator at BL-13. During measurements, the experimental chamber had a base pressure of about 5×10^{-9} Torr. NEXAFS spectra around the C K-edge were recorded in TEY mode by measuring a sample drain current.

Fig. 2 describes NEXAFS spectra of HOPG in C K-edge region measured at several azimuthal angle ϕ from 0° , shown

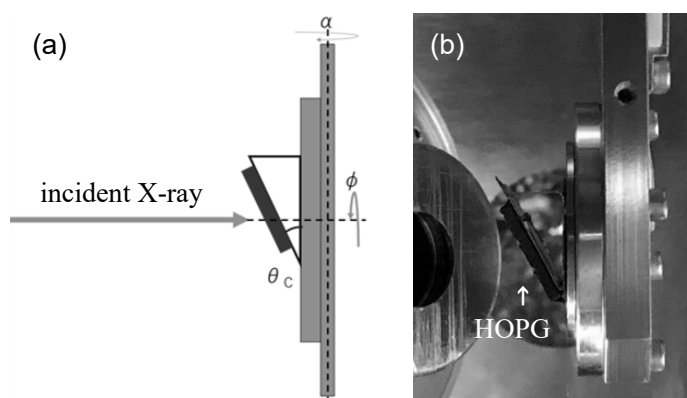


FIGURE 1. (a) Schematic drawing of a sample in this experiment with incident X-ray axis and three rotation axes: α , θ , and ϕ . (b) Actual mounted HOPG sample on a sample manipulator with the fixed tilt angle θ_c at the BL-13 end station.

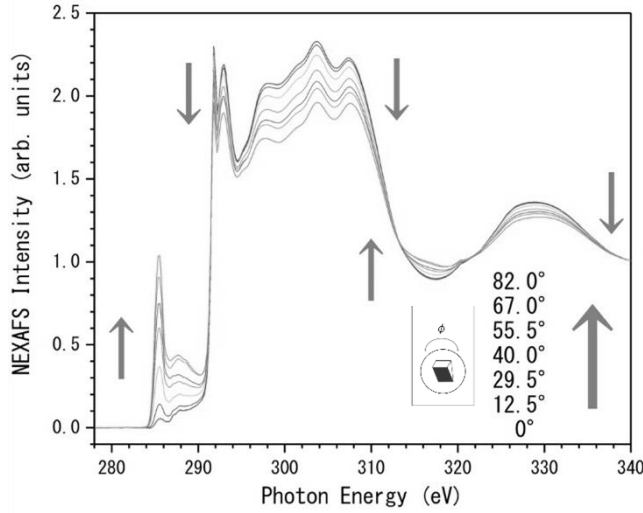


FIGURE 2. Normalized C K-edge NEXAFS spectra measured for tilted HOPG by changing the azimuthal angle ϕ . The other angles are fixed at $\alpha=0^\circ$ and $\theta=30^\circ$.

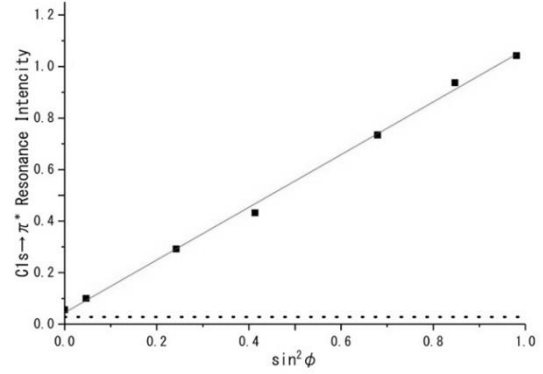


FIGURE 3. Plot of the first π^* intensity depending on $\sin^2\phi$ ($\alpha=0^\circ$ and $\theta=30^\circ$). The solid line is fitted result by Eq. (1). The dotted line indicates the intensity I_\perp at $\alpha=\theta=0^\circ$.

in inset orientation, to 82° . The spectra which were normalized at pre-edge and 340 eV indicate clear angle-dependent intensity alternation with isosbestic points. HOPG is multilayers of two-dimensional sp^2 hybridized carbon atoms (i.e. graphene) and has well-defined electronic orbitals like σ and σ^* orbitals within the planes and π and π^* ones perpendicular to the plane. So, the first peak at 285 eV which becomes higher intensity at the higher ϕ , comes from π^* resonance, while the second σ^* resonances around 292 eV shows opposite angle dependence.

Here, the degree of linear polarization, P , is normally defined by $P = |E_x|^2 / (|E_x|^2 + |E_z|^2)$. $|E_x|^2$ and $|E_z|^2$ are relative strength of linearly polarized X-ray component (parallel to the synchrotron ring) and its perpendicular component, respectively. So, the observable NEXAFS intensity, I , is described using X and Z components of transition intensities coming from σ^* and π^* transitions by $I = PI_X + (1 - P)I_Z$. In the situation of different azimuthal angle ϕ , the intensity I_ϕ can be written by: [3]

$$I_\phi = m \cdot \sin^2 \phi + b \quad (1)$$

And therefore, the degree of linear polarization can be defined by:

$$P = \frac{[m/(b - I_\perp)] + 1}{[m/(b - I_\perp)] + 2} \quad (2)$$

where I_\perp is resonance intensity at completely normal incidence ($\alpha=\theta=0^\circ$).

Fig. 3 shows the intensity plot obtained at the 285 eV π^* resonance against $\sin^2\phi$ according to Eq. (1), indicating the good linear relation. So, we can simply get the gradient of the line, m , and the intercept of the line, b , from the linear fitting. I_\perp was separately obtained by measuring the same resonance intensity at $\alpha=\theta=0^\circ$ (ϕ is free) condition (experimentally $\theta_c=30^\circ$, $\phi=90^\circ$, and $\alpha=-30^\circ$). By using Eq. (2), P at the 285 eV π^* resonance was derived to be 0.989 ± 0.010 , which has reproducibility for several measurements. By considering other resonances like the 292 eV and 298 eV σ^* resonances, the averaged degree of linear polarization at BL-13 was determined to be 0.96. This higher value derived by this simple evaluation method is due to narrow opening of four-jaw slits in the perpendicular direction equipped at the most upstream position of BL-13.

REFERENCES

1. J. Stöhr and R. Jaeger, *Phys. Rev. B* **26**, 4111 (1982).
2. G. Hähner, R. Hofer, and I. Klingenfuss, *Langmuir* **17**, 7047 (2001).
3. B. Watts, L. Thomsen and P.C. Dastoor, *J. Electron Spectrosc. Relat. Phenom.* **151**, 208 (2006).
4. Homepage of Hiroshima Synchrotron Radiation Center, http://www.hsrc.hiroshima-u.ac.jp/english/storagering_beamlines/beamlines.html.

XANES and XPS measurements of Br-incorporated DNA related molecules

Misaki Hirato^{a,b}, Kentaro Fujii^b, Shin-ichi Wada^c, Yuji Baba^d, Akinari Yokoya^{b,a}

^aGraduate School of Science and Engineering, Ibaraki University, Japan

^bNational Institutes for Quantum and Radiological Science and Technology (QST), Japan

^cGraduate School of Science, Hiroshima University, Japan

^dFukushima research and development department, JAEA, Japan

Keywords: BrdUMP, TMP, DNA damage, XPS, XANES

Cells with DNA incorporating 5-bromouracil (BrU) as a thymine analogue have been known to be highly sensitive to ionizing irradiation. Thus, BrU has been expected to be a sensitizing agent in radiation therapy. Previously, a radiation-track simulation study proposed a mechanism that hydrated electrons produced by water radiolysis could react with the Br-DNA to form damage (1). The aim of the present study is to clarify the electronic states of DNA related molecules incorporating a bromine atom. In order to understand the physicochemical nature of Br-DNA, we investigated the binding energies of inner shell electrons of particular atoms in the DNA molecule using X-ray photoelectron spectroscopy (XPS) and X-ray Absorption Near Edge Structure (XANES) around the energies of C, N, O and P K-absorption edges. In addition, resonant Auger spectra were measured near the K-edges of C and N. Thin film samples of 5-bromo-2'-deoxyuridine-5'-monophosphate (BrdUMP) and thymidine-5'-monophosphate (TMP) on an indium substrate were used for the spectroscopies. Obtained results indicate that the photoelectron binding energies, as well as XANES spectra, were similar for those sample molecules regardless of binding of a bromine atom. Contrary to the initial expectation, it is concluded that a bromine atom does not significantly contribute to the inner shell or unoccupied states in these molecules. S / N of the resonant Auger electron spectra were needed to be improved for further quantitative analyses. Experiments on the effect of bromine atoms on the valence electronic state are currently being addressed.

REFERENCES

1. Watanabe and Nikjoo *Int. J. Radiat. Biol.* **78**, 953-66 (2002).

X-ray Absorption Spectroscopy and Photoelectron Spectroscopy for a Deliquescent Ionic Liquid

Yasumasa Hikosaka^a and Shin-ichi Wada^b

^aUniversity of Toyama, 2630 Sugitani, Toyama, 930-0194, Japan

^bHiroshima University, 1-3-2 Kagamiyama, Higashi-Hiroshima, 739-8511 Japan

Keywords: Ionic liquid; X-ray absorption spectroscopy; X-ray photoelectron spectroscopy.

Ionic liquid is a category of salts that exist in liquid phase over a wide temperature range. It rarely evaporates even under vacuum, owing to its extremely-low vapor pressure. 1-Butyl-3-methylimidazolium chloride (BMI-Cl), one typical ionic liquid, has a melting point of 70°C and the pure sample is in solid phase at room temperature. However, due to its deliquescent property, it often exists as a liquid under the atmosphere even at room temperature. The deliquescence may affect the interaction between the cation and anion species in the ionic liquid, which is of great interest. We have a future plan to study the deliquescence dynamics by electron-electron coincidence spectroscopy [1]. In this study, we have investigated if the deliquescent BMI-Cl sample can be properly introduced inside the measurement chamber stationed at beamline BL-13 and if the prepared sample is suitable for advanced studies by electron-electron coincidence spectroscopy.

A small droplet of deliquescent BMI-Cl liquid was put onto a gold surface under the atmosphere and was transferred into our measurement chamber. Any sizable increase in the base pressure ($\sim 5 \times 10^{-9}$ Torr) of the chamber was not detected and the droplet was retained on the surface during a day of the experiment, indicating the extremely-low vapor pressure of the deliquescent liquid. To investigate the liquid sample condition put under vacuum, X-ray absorption spectroscopy (XAS) and X-ray photoelectron spectroscopy (XPS) were performed for its Cl2p, C1s, and N1s regions. Figure 1 shows the XAS spectrum in the N1s region. The spectral features are in good agreement with those reported previously [2]. The sharp peak around a photon energy of 402 eV is assigned to the N1s $\rightarrow \pi^*$ transitions of the imidazolium ring, while the broad structures above 405 eV are allocated to 1s $\rightarrow \sigma^*$ transitions [2]. This observation indicates that a proper sample is available by the droplet simply prepared in the atmosphere and then introducing into vacuum.

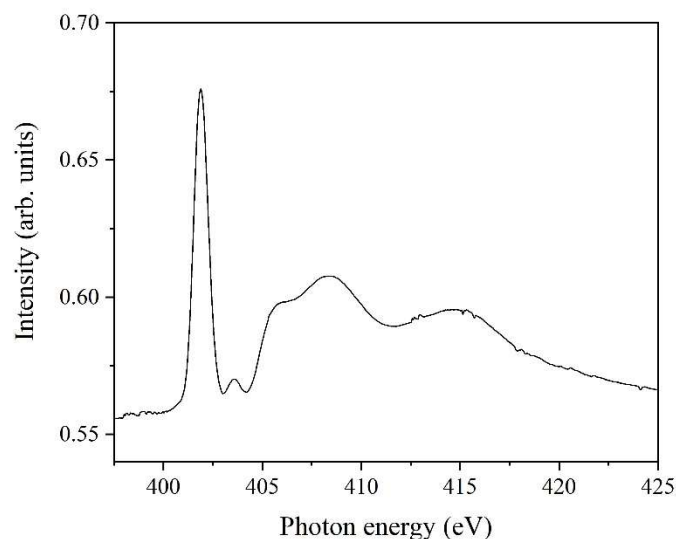


FIGURE 1. XAS spectrum of a deliquescent 1-butyl-3-methylimidazolium chloride sample in the N1s region.

The cation species in the liquid has two nitrogen atoms in the imidazolium ring, and the one bonding to the methyl group is often drawn as having the positive charge. If the chemical shift between the N1s photoelectrons would be large enough to be resolved in the present energy resolution, two peaks of comparable intensities should appear on a photoelectron spectrum. The N1s photoelectron spectrum shown in Fig. 2, measured at a photon energy of 507 eV, however exhibits a feature different from the expectation: a peak structure around a kinetic energy of 96 eV and a small shoulder on the higher kinetic energy side. The observed peak structure might reflect the solvation of the cation by water molecules. We plan further studies to give insight into the information of the solvation.

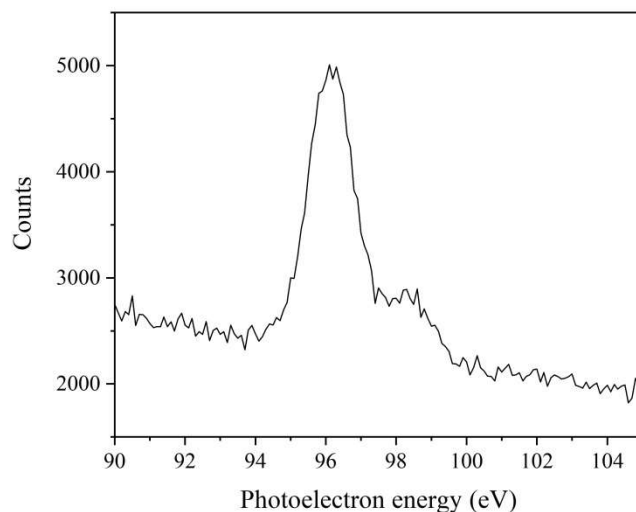


FIGURE 2. N1s XPS spectrum of a deliquescent 1-butyl-3-methylimidazolium chloride sample.

REFERENCES

1. Y. Hikosaka et al., *J. Electron Spectrosc. Rel. Phenom.* **213**, 17–21 (2016).
2. F. Rodrigues, G. M. do Nascimento and P. S. Santos, *J. Electron Spectrosc. Rel. Phenom.* **155**, 148–154 (2007).

Valence Trends in $\text{Sm}(\text{Co}_{1-x}\text{Cu}_x)_5$ and $\text{Ce}(\text{Cu}_{1-x}\text{Co}_x)_5$

Tetsuro Ueno^a, Hiroaki Shishido^{b,c}, Kotaro Saito^d, Masahiro Sawada^e, and
Munehisa Matsumoto^{d,f}

^a*Quantum Beam Science Research Directorate, National Institutes for Quantum and
Radiological Science and Technology, 1-1-1 Koto, Sayo, Hyogo 679-5148, Japan*

^b*Department of Physics and Electronics, Osaka Prefecture University, 1-1 Gakuen-cho, Naka-ku,
Sakai, Osaka 599-8531, Japan*

^c*NanoSquare Research Institute, Osaka Prefecture University, 1-1 Gakuen-cho, Naka-ku,
Sakai, Osaka 599-8531, Japan*

^d*Institute of Materials Structure Science, High Energy Accelerator Research Organization, Oho 1-1,
Tsukuba, Ibaraki 305-0801, Japan*

^e*Hiroshima Synchrotron Radiation Center, Hiroshima University, 2-313 Kagamiyama,
Higashihiroshima, Hiroshima 739-0046, Japan*

^f*Institute for Solid State Physics, University of Tokyo, Kashiwanoha 5-1-5, Kashiwa, Chiba 277-8581,
Japan*

Keywords: rare earth permanent magnets, grain boundary phase, magnetic quantum critical point

In order to possibly design a useful material on demand, it is a crucial problem to understand how the macroscopic functionalities of the target material emerge out of the microscopic properties derived from electronic structure. We are working on such a problem posed by rare-earth permanent magnets, which provide an ideal playground where a non-trivial electronic structure made of $4f$ electrons and $3d$ electrons combined with an optimal combination of the main-phase ferromagnets and paramagnets lead to the extremely slow decay of the spontaneously magnetized state.

Representative examples are Nd-Fe-B magnets [1] and Sm-Co magnets [2]. It has been empirically known [3,4] that certain optimal conditions exist for the chemical composition of the grain boundary phase in Nd-Fe-B magnets and the cell-boundary phase in Sm-Co magnets and for the particular structure on the mesoscopic scale, so-called the microstructure. Recently, practical demands and fundamental interests pose a question concerning a prospective fabrication of a working permanent magnet made of a ferromagnet with the ThMn_{12} structure [5,6] as the main phase, and a quest for the better main phases and the proper microstructure with “good” grain boundary phases are in progress [7,8]. At this point, lack of the proper understanding of the grain-boundary phases in the permanent magnets from first principles is a part of the bottleneck. Most notably, it is not entirely clear what exactly characterizes the “good” grain boundary phase or the cell boundary phases for a permanent magnet utility. Thus, it is essential to understand and possibly control the characterization of the grain boundary phases or the cell boundary phases in those bulk rare-earth permanent magnets.

Here we look into the case of the Sm-Co magnet, where Cu-enriched $\text{Sm}(\text{Co,Cu})_5$ in the cell-boundary phase [2], seems to help in realizing good coercivity, a measure of the robustness of the magnetized state against externally imposed magnetic fields. For the case of Nd-Fe-B magnet, we refer to a separate study [9]. It is hoped that these studies would be a help in the fabrication of a prospective new permanent magnet and also for bulk material design, in general, starting from the microscopic viewpoint.

Polycrystals of $\text{Sm}(\text{Co}_{1-x}\text{Cu}_x)_5$ ($0 \leq x \leq 1$) were grown by arc-melting, in addition to $\text{Ce}(\text{Co}_{1-x}\text{Cu}_x)_5$ ($0 \leq x \leq 0.8$) which we studied in the previous work and are taken as a reference case for the present study. X-ray Absorption Spectroscopy (XAS) experiment was performed at HiSOR BL-14, Hiroshima University, Japan. Clean surface of the sample was prepared by filing in ultra-high vacuum. X-ray absorption spectra were collected by a total-electron-yield method measuring the sample drain current. Photon energy was tuned to Ce $M_{4,5}$ absorption edges ($3d-4f$ transition) for $\text{Ce}(\text{Co,Cu})_5$ and Sm $M_{4,5}$ for $\text{Sm}(\text{Co,Cu})_5$.

X-ray absorption spectra with respect to temperature (T) and Cu concentration (x) are shown for the Sm compound in Fig. 1(a) and for the Ce compounds in Fig. 1 (b). In Ce compounds, the tendency toward a clear trivalent state is seen in the composition range $x > 0.6$. In a separate bulk measurement of magnetization

curves, it is remarkable that strong high-temperature coercivity is observed for $x = 0.3$ and $x = 0.4$ which is interpreted as an outcome of coupling between a valence transition or crossover and magnetic anisotropy in those “optimal” chemical composition in $\text{Ce}(\text{Co},\text{Cu})_5$ systems [10]. An analogous mechanism for an intrinsic coercivity can be expected for the Sm analogues.

Sm valence state looks rather stable for the chemical composition, in contrast to the Ce counterpart, which is reasonable considering the mirroring relation between Ce and Sm, where one electron/hole is localized in $\text{Ce}^{3+}/\text{Sm}^{3+}$, respectively, in the lowest $J=5/2$ multiplet. Effects of valence fluctuations in Sm is expected in the chemical composition space where the valence state of Ce is robust [11].

Precise temperature control system implemented at HiSOR BL-14 has helped us to thoroughly investigate the valence state of Ce and Sm in $\text{R}(\text{Co},\text{Cu})_5$ ($\text{R}=\text{Ce}$ and Sm) all over the relevant temperature range.

We acknowledge helpful comments given by Y. Kuramoto and discussions with J. B. Staunton, C. E. Patrick, H. Sepehri-Amin, T. Ohkubo in related projects. The present research was partly supported by JSPS KAKENHI grant number 15K13525. Numerical calculations in the theory part were executed in ISSP supercomputer center, University of Tokyo.

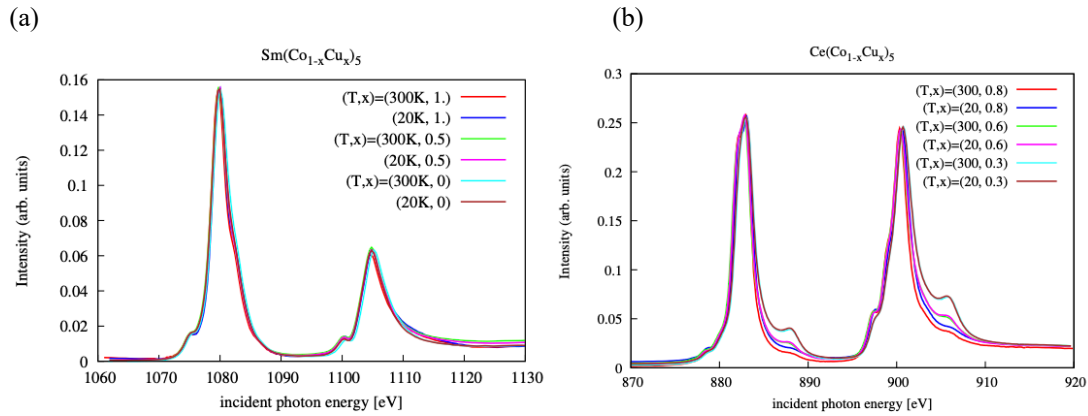


FIGURE 1. X-ray absorption spectra (a) at Sm $M_{4,5}$ edges for $\text{Sm}(\text{Co}_{1-x}\text{Cu}_x)_5$ ($0 \leq x \leq 1$) and (b) at Ce $M_{4,5}$ edges for $\text{Ce}(\text{Co}_{1-x}\text{Cu}_x)_5$ ($0.3 \leq x \leq 0.8$) at 20 K and 300 K. Temperature dependence was carefully monitored in between which is not shown here for the clarity of presentation. In plotting the data, peak heights coming from the $(4f)^1$ state for Ce and $(4f)^5$ state for Sm have been adjusted to match onto each other so that the trends in the satellite peak coming from $(4f)^0$ for Ce and $(4f)^6$ for Sm can be elucidated. The overall trend is that $4f$ -electrons tend to populate the rare-earth site more as Cu is enriched and the temperature is reduced.

REFERENCES

1. For a review, see e.g. J. F. Herbst, *Rev. Mod. Phys.* **63**, 819 (1991).
2. For a review, see e.g. K. Ohashi, *J. Japan Inst. Metals* **76**, 96 (2012) (in Japanese except for abstract and figure captions)
3. For a review, see e.g. K. Hono and H. Sepehri-Amin, *Scr. Mater.* **67**, 530 (2012).
4. For a recent review, see e.g. K. Hono and H. Sepehri-Amin, *Scr. Mater.* **151**, 6 (2018).
5. One of the earliest attempts dates back to the pioneering work: K. Ohashi *et al.*, *IEEE Trans. Magn.* **23**, 3101 (1987).
6. A recent line of attack is seen in T. Miyake, K. Terakura, Y. Harashima, H. Kino, S. Ishibashi., *J. Phys. Soc. Jpn.* **83**, 043702 (2014).
7. P. Tozman *et al.*, *Acta Materialia* **153**, 354 (2018).
8. H. Sepehri-Amin *et al.*, *Acta Materialia* **194**, 337 (2020).
9. M. Morishita, M. Matsumoto *et al.*, in preparation. See also a recent development in U. Kamber *et al.*, *Science* **368** eaay6757 (2020).
10. H. Shishido, T. Ueno, K. Saito, M. Matsumoto, in preparation.
11. M. Matsumoto, *Phys. Rev. Materials* **4**, 054401 (2020).

Magnetic property of nickel hydroxide nanosheet

Y. Naruo^a, S. Uechi^a, M. Sawada^b, A. Funatsu^c, F. Shimojo^c, S. Ida^c, M. Hara^c

^aGraduate School of Science and Technology, Kumamoto University,
2-39-1 Kurokami, Kumamoto 860-8555, Japan

^bHiroshima Synchrotron Radiation Center, Hiroshima University,
2-313 Kagamiyama, Higashi-Hiroshima 739-0046, Japan

^cFaculty of Advanced Science and Technology, Kumamoto University,
2-39-1 Kurokami, Kumamoto 860-8555, Japan

Keywords: nickel hydroxide nanosheet, XAS, XMCD

Nickel hydroxide Ni(OH)₂ has been developed as an electrode component for battery applications in a few decades. Recently, the importance has increased not only in the battery technologies but also in chemical catalysis, supercapacitors, devices and sensors [1]. The nickel hydroxide has a typical hexagonal layered structure in which nickel cations and hydroxyl anions are two-dimensionally arranged as shown in Fig.1(a). The layered crystal can be exfoliated into monolayers [2], which are applicable for building blocks in van der Waals heterostructures consisting of various two-dimensional (2D) materials [3]. In this study, we have investigated effects of thermal annealing on magnetic properties of the monolayer nickel hydroxide nanosheets by X-ray magnetic circular dichroism (XMCD) measurement.

Nickel hydroxide nanosheets were deposited on a highly doped Si substrate by the Langmuir-Blodgett method. Figure 1(b) shows an atomic force microscopy image of the nanosheets. In order to investigate electronic states in the nickel hydroxide nanosheets, X-ray absorption near edge structure (XANES) were measured at the BL-14 beam line of HiSOR. The measured X-ray absorption corresponds to excitations from 2p core levels to 3d unoccupied levels. The spectra Ni L₂ and L₃ edges of Ni were taken in total electron yield mode by measuring the current due to X-ray absorption thorough the conductive Si substrate. The directions of the incident X-ray beam and the external magnetic field of 1.1 T supplied by a permanent magnet array were perpendicular to the substrate. The degree of X-ray circular polarization was estimated to be about 70 %. Thermal annealing for 30 minutes at different temperatures and subsequent XANES measurements at room temperature were carried out in the UHV chamber of the beam line.

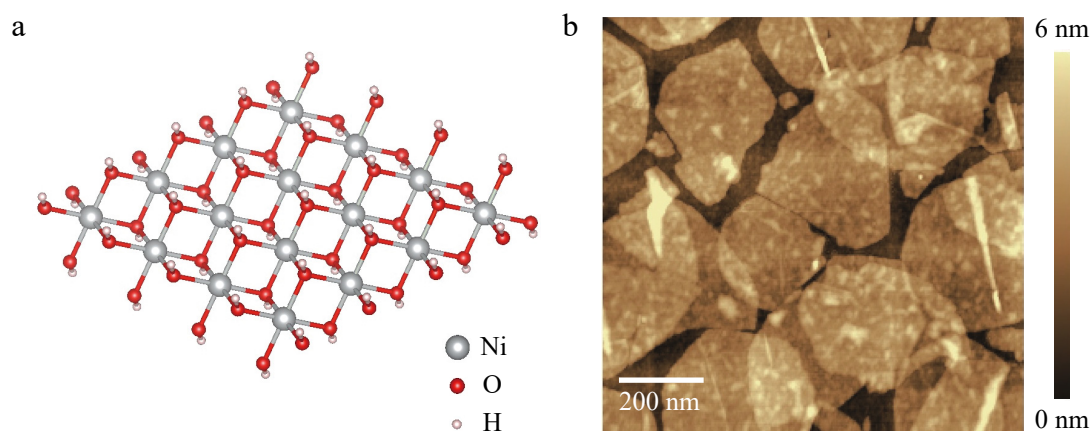


FIGURE 1. (a) Structural model of nickel hydroxide nanosheet. (b) Atomic microscopy image of nickel hydroxide nanosheets deposited on a Si substrate.

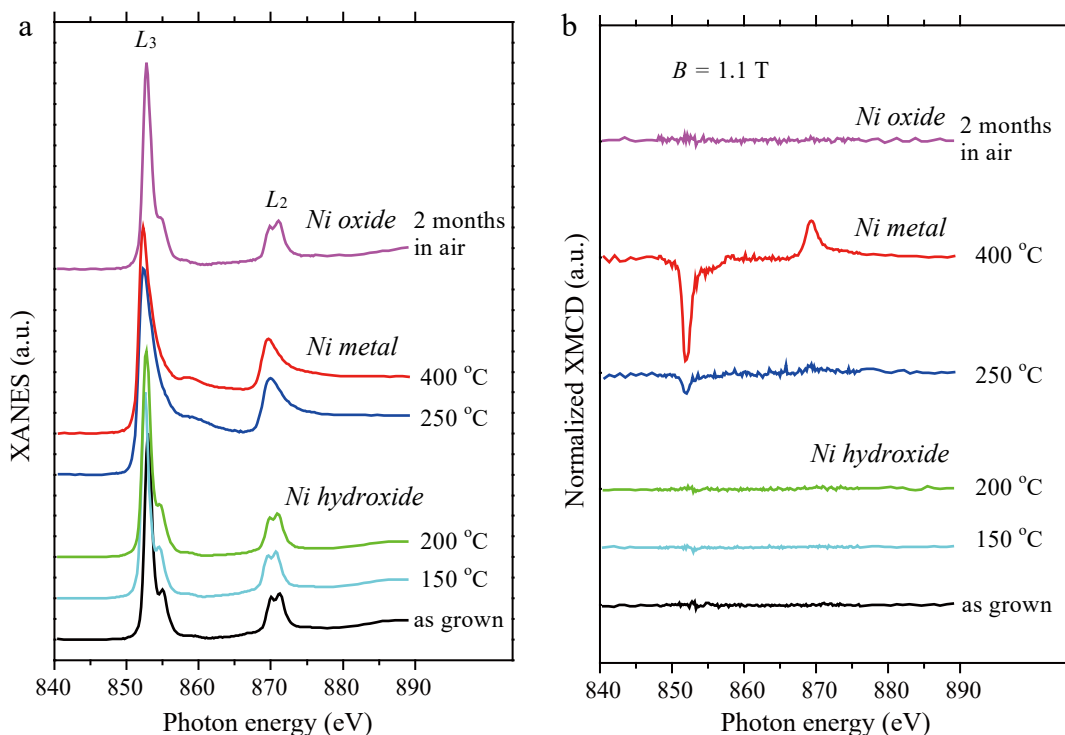


FIGURE 2. (a) X-ray absorption near edge structure (XANES) for different annealing temperatures. (b) Normalized X-ray magnetic circular dichroism (XMCD) spectra for different annealing temperatures.

Figure 2 (a) shows the X-ray absorption spectra for different settings of the annealing temperature. The as grown sample exhibited multiple structures corresponding to the transition $2p^63d^8 \rightarrow 2p^53d^9$, which indicates that the nickel hydroxide has valence state of Ni^{2+} . Above 250 °C, the multiple structure drastically changed into two broad metallic peaks similar to spectra observed in deposited nickel metal films [4,5]. The result indicates that the nickel hydroxide nanosheets are converted to nickel metal structures by thermal annealing under vacuum. The converted metallic sample annealed at 400 °C was easily oxidized due to air exposure, so that the XANES signal changed into the multiple structure again.

Figure 2(b) shows XMCD spectra normalized by the amplitude of L_3 peak in each X-ray absorption spectra. A weak XMCD signal appeared in the sample annealed at 250 °C and was enhanced in the sample annealed at 400 °C, which means a ferromagnetic order induced by the metallization. In the XMCD measurements, the direction of the external magnetic field of 1.1 T was perpendicular to the sample, so that the magnetic moments were not fully aligned along the magnetic field especially in 250 °C sample. Another possibility is a reduction of the Curie temperature, which is strongly dependent on the metal structure.

REFERENCES

1. D. S. Hall, D. J. Lockwood, C. Bock, and B. R. MacDougall, *Proc. R. Soc. A* **471**, 20140792 (2015).
2. S. Ida, D. Shiga, M. Koinuma, and Y. Matsumoto, *J. Am. Chem. Soc.* **130**, 14038-14039 (2008).
3. A. K. Geim and I. V. Grigorieva, *Nature* **499**, 419-425 (2013).
4. C. T. Chen, F. Sette, Y. Ma, and S. Modesti, *Phys. Rev. B* **42**, 7262-7265 (1990).
5. J. Vogel, G. Panaccione, and M. Sacchi, *Phys. Rev. B* **50**, 7157-7160 (1994).

Magnetic Study of Co/h-BN/Fe/Ni Interface by Soft X-ray Magnetic Circular Dichroism

Tatsuya Mayumi^a, Yuka Ohashi^a, Masahiro Sawada^b

^a*Department of Physical Science, Graduate School of Science, Hiroshima University*

^b*Hiroshima Synchrotron Radiation Center, Hiroshima University*

Keywords: boron nitride, cobalt, iron; X-ray magnetic circular dichroism

Tunnel magnetoresistance (TMR) effect is one of key phenomena for developing of spintronic devices. Monolayer hexagonal boron nitride is an insulating layered material with stable honeycomb structure. It is expected to provide an ideal barrier layer in magnetic tunnel junction (MTJ), where a pinhole-less ultrathin barrier layer ensures large MR ratio and low impedance insulation to promote quick-response in device applications. Spin-dependent transport studies with the MTJ including a monoatomic h-BN barrier layer have shown the MR ratio up to 150% at room temperature [1]. So far, magnetic state at the interface between a magnetic layer and a monolayer h-BN has not been sufficiently clarified, although it takes an essential role in a mechanism of TMR. To clarify magnetic state at the interface between a magnetic layer and monolayer h-BN, we have investigated magnetic properties of Co and Fe layers that sandwich a monolayer h-BN which are grown on Ni(111), by means of soft X-ray magnetic circular dichroism (XMCD) spectroscopy.

We fabricated Co wedge films on h-BN/Fe/Ni(111) films, whose Fe layer was intercalated under h-BN layer with a post annealing after 2.5 ML deposition of Fe. High-quality h-BN monolayer was prepared on a Ni(111) surface by cracking of vaporized borazine ($B_3N_3H_6$). The samples of Co/h-BN/Fe/Ni(111) are obtained by MBE evaporation of Co at room temperature. The XMCD experiments were in-situ performed at HiSOR-BL14, where spectra are measured at both $L_{2,3}$ edges of Fe and Co. Figure 1 shows XMCD spectra for h-BN/Fe/Ni(111) and Co/h-BN/Fe/Ni(111) with different thickness of Co. The opposite sign in XMCD signals are confirmed at each edge of L_2 and L_3 , between Fe spectra in h-BN/Fe/Ni(111) and Co spectra in 1.6ML-Co/h-BN/Fe/Ni(111). This qualitative result supports antiferromagnetic alignment of Fe and Co spins, whose behavior is similar to a case in Co/h-BN/Ni(111) without Fe intercalation layer. The MCD signal of Co disappears for a thicker Co layer, because no magnetization is induced by external magnetic field along surface normal direction, due to strong in-plane magnetic anisotropy.

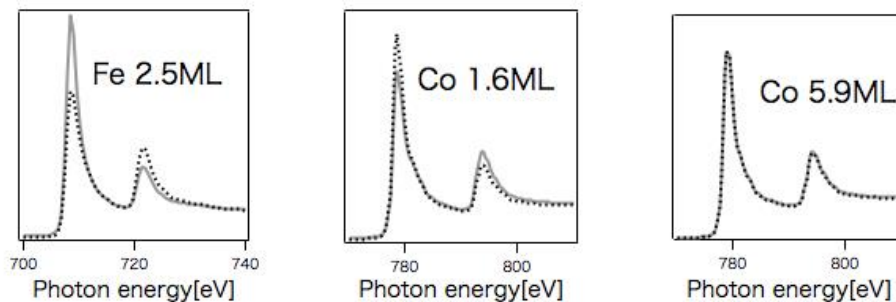


FIGURE 1. XMCD for h-BN/2.5ML-Fe/Ni(111) and Co/h-BN/2.5ML-Fe/Ni(111) with Co thickness of 1.6 and 5.9 ML. For each case, XAS spectra are shown for measurement with sample magnetization direction parallel (μ_+ shown in dotted curves) and antiparallel (μ_- shown in thick curves) to photon helicity vector.

REFERENCES

1. A. Dankert, M. V. Kamalakar, A. Wajid, R. S. Patel, and S. P. Dash, *Nano. Res.* **8**, 1357 (2015).

Hydrogen effects on the magnetic property of Laves phase GdCo₂ probed by XMCD

S. Kanamori¹, K. Ishimoto², N. Ishimatsu¹, N. Kawamura³, K. Sakaki⁴,
M. Sawada⁵, Y. Nakamura⁴, S. Nakano⁶

¹Grad. Sch. Sci., Hiroshima University, ²Sch. Sci., Hiroshima University, ³JASRI/SPring-8, ⁴AIST, ⁵HiSOR, ⁶NIMS

Keywords: Enter keywords.

Laves phase compound (RT_2) composed of $4f$ heavy rare earth (R) and $3d$ transition metal (T) is characterized by ferrimagnetism in which the magnetic moments of R and T atoms align antiparallel. Because of the high storage capacity of hydrogen, Laves phase GdFe₂ is hydrogenated to GdFe₂H _{x} ($x > 5$) in pressurized hydrogen atmosphere above 10 GPa. The hydrogenation is known to change the ferrimagnetic coupling in GdFe₂ to ferromagnetic one; both Gd and Fe magnetic moments align parallel [1-3]. The same hydrogen-induced change is predicted for the magnetic coupling in GdCo₂H _{x} ($x > 5$).

It is well known that RT_2 H _{x} with a moderate hydrogen content ($x \sim 3$) is stable under ambient pressure, and even the small amount of hydrogen content modifies the magnetic property of the Laves phase compound [4]. In this study, we synthesized GdCo₂H₃, and hydrogen effects on the coupling between Co and Gd magnetic moments were investigated element-selectively by using X-ray magnetic circular dichroism (XMCD). We performed experiments on SPring-8 BL39XU and HiSOR BL-14 for the XMCD measurements at Gd $L_{2,3}$ edges and Co $L_{2,3}$ edges, respectively.

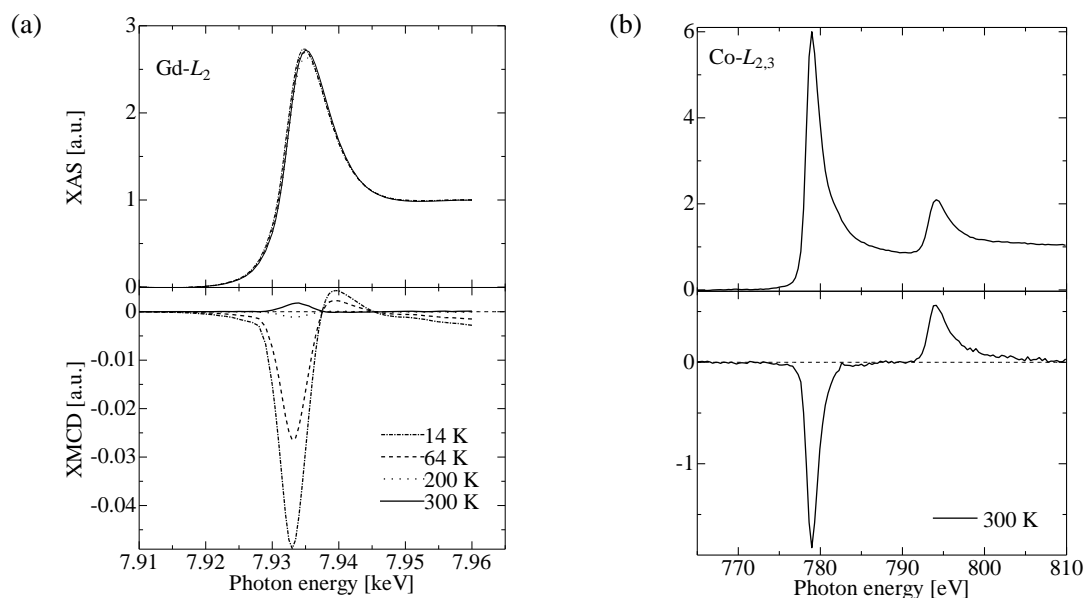


FIGURE 1. Temperature dependence of XMCD and XAS of GdCo₂H₃ ((a): Gd- L_2 , (b) : Co- $L_{2,3}$).

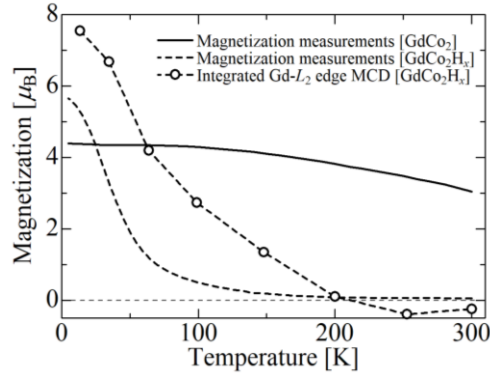


FIGURE 2. Temperature dependence of the magnetism of GdCo_2H_3 and the integrated intensity of Gd- L_2 edge XMCD

As shown in Fig. 1(a), XMCD spectra of GdCo_2H_3 show negative peaks at the Gd L_2 edge under low temperatures, which is as same as the sign before hydrogenation. The peak of XMCD spectra decreases gradually with increasing temperature and inverts its sign to positive above ~ 200 K. Therefore, the direction of Gd moments changes from parallel to antiparallel to the magnetic field above ~ 200 K, which is consistent with the signs of XMCD at the Co $L_{2,3}$ edges (Fig. 1(b)); Co magnetic moments align parallel to the applied magnetic field at 300 K. These results demonstrate that the flipping of the moments occurs at ~ 200 K, however, the magnetic coupling between Gd and Co moments remains ferrimagnetic in the temperature range up to 300 K. As shown in Fig. 2, the hydrogenation enhances the net magnetization at $T=4$ K but reduces the Curie temperature significantly from 400 K [5] to ~ 60 K. Hydrogenation up to $x\sim 3$ modifies the magnetic properties of Laves phase GdCo_2 , however, larger amount of hydrogen content is probably required to introduce the change in the magnetic coupling.

REFERENCES

- [1] T. Mitsui *et al.*, J. Phys. Soc. Jpn., **85**, 123707 (2016).
- [2] T. Mitsui *et al.*, J. Alloys. Compd., **580**, S264 (2013).
- [3] N. Ishimatsu *et al.*, SPring-8/SACLA Res. Rep. **4**, 1 (2016).
- [4] X. Li *et al.*, Intermetallics, **7**, 207-211, (1999).
- [5] M. A. Laguna-Marco, Doctor thesis, Prensas Universitarias de Zaragoza (2007).

Development of a Measurement Software for Soft X-ray Reflectometry with High Usability and Flexibility in axes control

Kazuha Machida^a, Tatsuya Mayumi^b, Masahiro Sawada^c

^aDepartment of Physical Sciences, Faculty of Science, Hiroshima University

^bDepartment of Physical Science, Graduate School of Science, Hiroshima University

^cHiroshima Synchrotron Radiation Center, Hiroshima University

Keywords: software development, soft X-ray, reflectometry

Soft X-ray reflectometry is one of useful methods for investigation of a valence electron structure, which is probed through a resonant scattering process in the vicinity of an absorption edge. Since a magneto-optical effect appears in a reflectance profile for polarized SR light, the reflectometry method can also be utilized to analysis of a magnetic state and a magnetic structure for many kind of magnetic materials including insulators. Insensitivity to sample surface of the photon-in-photon-out technique is an advantage to investigate practical materials like an electronic/spintronic device, whose region of interest are deep inside of the layered structures. Measurements under low vacuum or atmospheric pressure in helium-pass expands the capability of soft X-ray reflectometry into ambient/operando spectroscopy, whose vacuum environment can be easily established by vacuum separation technique from UHV beamline with X-ray transmission membrane.

Recently, we have developed a soft X-ray reflectometer at HiSOR-BL14, whose motorized mechanism is established in low vacuum chamber. Essential mechanism in the reflectometer are, an incidence angle control with sample rotation, and a detection angle control which determines reflection angle with the photon detector scanning around rotation center in the sample surface. An additional axis is installed in the sample holder to adjust the sample surface level into the rotation center where the SR light is focused. For the reflectometry measurement, these three motorized axes and energy (wave length) of photon provided from the SR beamline should be systematically controlled through motion commands from PC. For automatic data acquisition of the reflectometry, we have established an user-friendly software with high flexibility in the axes control.

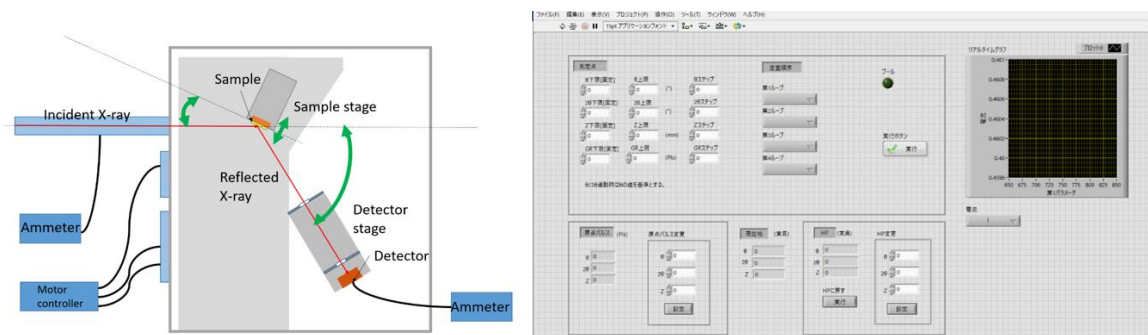


FIGURE 1. Schematic diagram of the soft X-ray reflectometer for BL-14 (left), and the user interface panel of developed software for the reflectometry experiments (right).

High Quality Cr₂O₃ Layers Growth on Graphene-Covered Ni(111) Substrate

Xueyao Hou^a, Masahiro Sawada^b

^aDepartment of Physical Science, Graduate School of Science, Hiroshima University

^bHiroshima Synchrotron Radiation Center, Hiroshima University

Keywords: Cr₂O₃, thin film, X-ray absorption spectra (XAS)

Antiferromagnet (AFM) exhibits a spontaneous ferromagnetic termination which is strongly linked to its AFM order parameter. The boundary magnetism of the locally uncompensated AFM lattice determines the topology of antiferromagnetic domain walls. The feature highlights a precise control method to the tiny uncompensated magnetic moment in AFM-based spintronic devices [1]. Chromium oxide (Cr₂O₃) is a potential ME-AFM material because of its electrically switchable magnetic states at room temperature and perpendicular magnetic anisotropy with neighboring ferromagnets. In this work, high-quality Cr₂O₃ layers are obtained by controlling the post-annealing procedure.

Monolayer graphene were fabricated via propylene cracking on Ni(111) substrate, and used as buffer layer to avoid Ni(111) oxidation of during the Cr₂O₃ deposition. Cr₂O₃ layers were deposited on graphene covered Ni(111) substrate by MBE with pressure $p_{O_2} = 2 \times 10^{-4}$ Pa. Comparing with graphene/Ni(111) (Figure 1(a)), the Cr₂O₃/graphene/Ni(111) (Figure 1(b)) keeps clear spots with 6-fold symmetry. As shown in Figure 1 (c), Cr L_{2,3} edge shows significant Cr³⁺ characteristic. The other possible oxidation states, +2 +4 and +6, can be ruled out because the corresponding XAS spectra are different from Cr³⁺ oxidation state. The same indication has been found comparing the environment of O K edge (Figure 1(d)). The in-plane lattice constant mismatch between Cr₂O₃ and graphene is about 9.23%. Thus, Cr₂O₃ layers are highly in-plane strained, which might induce novel phenomenon.

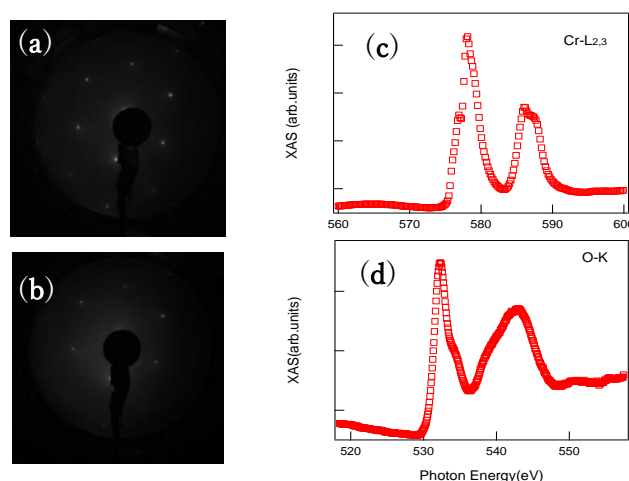


FIGURE 1. LEED patterns (Energy = 200 eV) of (a) graphene/Ni(111) substrate; (b) Cr₂O₃/graphene/Ni(111). XAS of Cr₂O₃/Graphene/Ni(111) at (c) Cr L-edge; (d) O K-edge.

REFERENCES

1. N. Wu, X. He, A. L. Wysocki, U. Lanke, T. Komesu, K. D. Belashchenko, C. Binek and P. A. Dowben, Phys Rev Lett **106** (8), 087202 (2011).